Comparison of electrical response of beta PVDF and PVDF-TrFE sheets

By

Jehanzad Zafar

DEPARTMENT OF PHYSICS

QUAID-I-AZAM UNIVERSITY

ISLAMABAD, PAKISTAN

2023

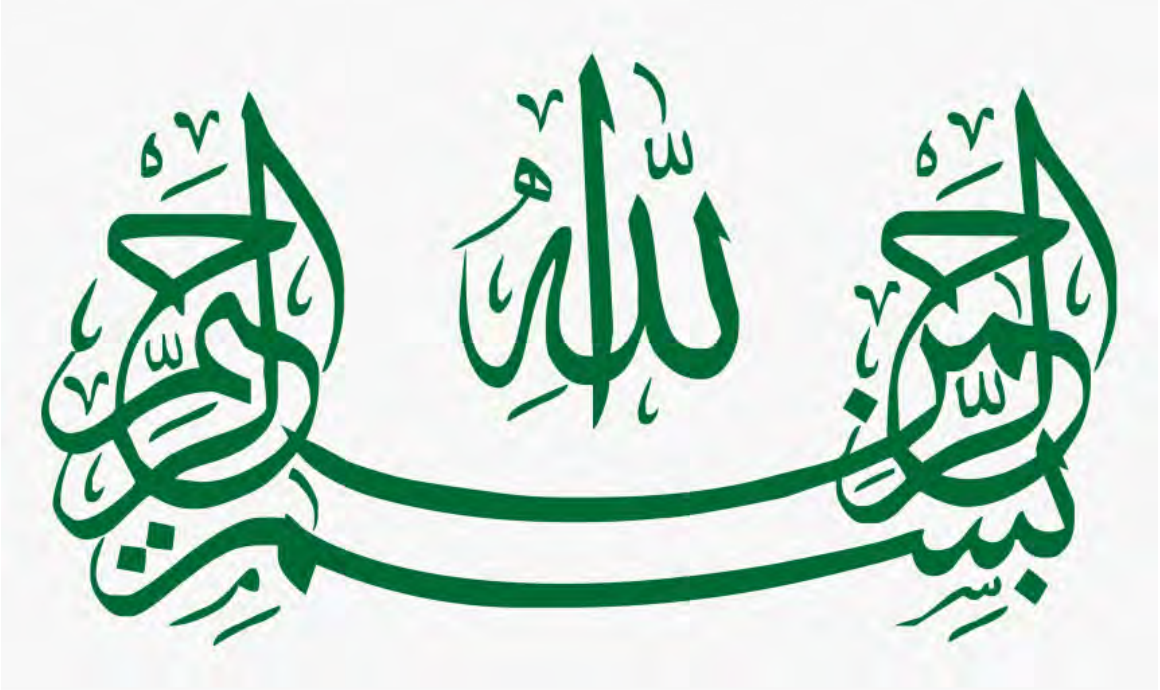

In the name of Allah, the Most Gracious, the Most Merciful

This work is submitted as a dissertation

In partial fulfillment of the requirement for the degree of

MASTER OF PHILOSOPHY

IN

PHYSICS

To The

Department of Physics

Quaid-i-Azam University

Islamabad, Pakistan

2022

CERTIFICATE

This is to certify that the experimental work in this dissertation has been carried out by ***Jehanzad Zafar*** under my supervision in the Superconductivity and Magnetism Lab, Department of Physics, Quaid-i-Azam University, Islamabad, Pakistan.

Supervisor:

Prof. Dr. Ghulam Hassnain Jaffari

Department of Physics

Quaid-i-Azam University

Islamabad, Pakistan.

Submitted Through:

Prof. Dr. Kashif Sabeeh

Chairman

Department of Physics

Quaid-i-Azam University

Islamabad, Pakistan.

To

My Family

ACKNOWLEDGMENT

*First and foremost, I would like to praise and thank **Allah the Almighty,** the Cherisher and Sustainer of the words, the Most Gracious and the Most Merciful, who gave me strength to achieve what I wanted to and blessed me all the way. Moreover, thousands of blessings be upon the Seal of the **Prophet Peace Be Upon Him,** the Most Perfect and Splendid, due to whom we are known as the Superb Ummah in the universe.*

*Then, I would like to express my sincere gratitude for my supervisor, my mentor, and my guider **Prof. Dr. Ghulam Hassnain Jaffari** for giving me the opportunity to do research and providing his continuous support, immense knowledge, valuable suggestions, guidance, and persistent supervision during my whole research work.*

*I am very grateful to my seniors **Musfira Aqeel, Dr.Fiza Mumtaz and Shahid Khan Niazi** for their guidance, support, and helpful advice. Their valuable discussions have always encouraged me throughout my research. I would like to extend my special appreciation and thanks to my lab fellows **Fahad Atta, Muhammad Waqas, Umme Habiba, Asra Babar** who helped and supported me.*

*Finally, and most importantly, I would like to pay my heartfelt thanks to my beloved parents **Mrs. Naz Gul Sanawar** and late **Mr. Zafar Khan** for their unconditional love, prayers and sacrifices for educating and preparing me for my future. My words would never be enough for all that they have done for me in life and raising me to be a person I am. Hearing their encouraging voices from a distance has been the brightest light in my darkest days. I cannot find the words to show my extremely deepest gratitude and love to my siblings **Zarafshan Gul, Behzad Zafar and Shahzad Zafar** for their endless and everlasting emotional and moral support, love ,care, and for all their countless efforts to make me happy and motivate in every situation. A special thanks to my Maternal uncle **Mr. Farhad Ali Khan**, your example has taught me to approach challenges with an open mind and to embrace failure as a stepping-stone toward success. A bundle of thanks to my friends **Asif Ullah and Pirzada** for their immense support every time.*

*My accomplishments and success are just because of my loved ones who believed in me. May **ALLAH** bless them all.*

Jehanzad Zafar

Table of Contents

List of Figures

Chapter 1

Chapter 2

Chapter 3

Chapter 4

List of Tables

Abstract

In this work, PVDF, indium tin oxide (ITO) coated β-PVDF and P(VDF-TrFE) free standing sheets have been studied in detail. Their structural, dielectric, and ferroelectric properties are compared. PVDF and P(VDF-TrFE) sheets are prepared by solvent casting technique. β-PVDF sheets were extracted from the etching of ITO by using Hydrochloric acid (HCl) as an etchant agent. The structural analysis of all the prepared samples is done using X-ray Diffraction (XRD) and Fourier transform infrared spectroscopy (FTIR). XRD and FTIR results show that P(VDF-TrFE) exhibits excellent crystallinity, followed by ITO etched PVDF and solvent casted PVDF. The higher crystallinity in P(VDF-TrFE) corresponds to steric hindrance between CHF and CH_2. In dielectric spectrum of solvent cast PVDF and ITO etched PVDF, only glass transition process related with relaxation of polymer chains is observed and their dielectric constant are compareable. Important feature observed in dielectric spectrum of P(VDF-TrFE) is the phase transition from ferroelectric to paraelectric. The ferroelectric phase transition occurs at T_c=395 K. At T_c chain conformation changes from TTTT to TTTG. Ferroelectric measurements of this specimen further confirm this trend. Solvent casted PVDF exhibits lossy loops and indicates high leakage current. PVDF/ITO displays resistive loops bacause of lower electrical conductivity. ITO etched PVDF results in saturated loops due to coating of better electrode i.e. Ag. P(VDF-TrFE) emerges as well-saturated loops, indicating excellent ferroelectric properties. The study further shows that removing ITO from PVDF through wet etching reveals the true electrical response. Additionally, adding TrFE to PVDF further enhance its ferroelectricity. The P(VDF-TrFE) sample exhibits a high dielectric constant and well-saturated $P-E$ loops. This makes P(VDF-TrFE) an attractive candidate for energy storage devices due to its impressive dielectric properties. It can also be used as a piezoelectric device due to its substantial remanent polarization (P_r).

Chapter 1 Introduction and Background

1.1 Introduction:

The sense of touch holds great significance in medical field, especially in the context of minimally invasive medical procedures that facilitate the identification and the treatment of numerous conditions, and surgeries that can be executed through a tiny cut [1]. But so far, significant focus has been placed on the development of piezoelectric sensors that can produce voltage upon being touched, compressed, or flexed [2]. Polymer-based ferroelectric materials offer exceptional flexibility, piezoelectricity, low processing temperatures and high electrical resistivity which makes them field of interest for flexible electronic devices like memory devices and sensors [3].

Energy harvesting is also considered one of the most promising research areas for producing sustainable power sources from the ambient environment. Energy harvesting is also known as energy scavenging which refers to the process of collecting energy from waste energy sources such as heat, vibrations and mechanical deformations and then converting it into useful electrical energy. Various sources are available for energy generation such as solar, wind, thermal energy, and mechanical vibrations. Moreover, most of these applications require the device to be able to function both indoors and outdoors with minimal dependence on weather conditions. Therefore, mechanical vibrations and human body movements have emerged as attractive energy sources for low-power and small electronic devices [4].

In recent years, interest has been growing in organic materials to enable the actuation of flexible devices due to their lightweight nature, mechanical flexibility, stretchable, cost-effective manufacturing, and compatibility with biological systems. Among the various piezoelectric material explored Poly (vinylidene fluoride) (PVDF) and its copolymer with trifluoroethylene (TrFE) have emerged as particularly promising options for numerous innovative applications [5] Enabling the piezoelectric polymers to be shaped and sized according to specific requirements will expand the range of their applications [2].

PVDF is also termed as poly (1, 1-difluoroethylene). PVDF is a highly non-reactive thermoplastic that belongs to the family of fluoropolymers. Its molecular structure consists of $(CH_2\text{-}CF_2)_n$ monomers. Researcher's attention has been grabbed by PVDF and its copolymer P(VDF-TrFE) for over a decade due to its remarkable properties as. The piezoelectric properties of PVDF were initially discovered by the Curie brothers in 1880 [6, 7]. The

ferroelectric property in PVDF was discovered in the early 1970's [8]. PVDF have five crystalline phases alpha (α) phase, beta (β) phase, gamma (γ) phase, delta (δ) phase and ε-phase. α-phase and ε-phase are non-polar in nature due to antiparallel packing of dipoles. The other three phases show good ferroelectric and piezoelectric response due to their polar nature [9].

Poly (vinylidene fluoride-trifluoroethylene) P(VDF-TrFE) is the most studied copolymer of PVDF. PVDF crystallization behavior can be changed by the addition of TrFE monomers. Recent research show that P(VDF-TrFE) can undergo direct crystallization into the β polar phase, regardless fabrication methods if the TrFE content exceeds the 20 mol% [10]. β-phase of P(VDF-TrFE) is the cause of its ferroelectricity.

The following chapter provides an In-depth analysis of dielectric properties, polarization mechanisms in dielectrics and the various forms of ferroelectricity, piezoelectricity, and pyroelectricity in materials. Additionally, the chapter includes a brief introduction to the primary materials we are currently investigating named as Poly (vinylidene fluoride) (PVDF), and Poly (vinylidene fluoride-trifluoroethylene) P(VDF-TrFE).

1.2 Types of materials:

The given information describes three categories of materials categorized by their electrical characteristics and level of conductivity, which are determined by their band gap and density of states [11, 12].

- Conductor
- Semiconductor
- Insulator

1.2.1 Conductors:

These materials have high conductivity and electricity can flow through them. There is no energy difference or band gap between their valence and conduction bands which allow electrons to move freely and participate in conduction. Their conductivity decreases with increasing temperature which results in an increase of resistance. The resistivity of these materials lie in the range of 10^{-2} to 10^{-8} Ωm [11, 12].

1.2.2 Semiconductors:

Semiconductor materials lie in between the conductors and insulators in terms of their electrical properties. They have a very small energy gap between their valence and conduction bands. This small gap is known as the narrow band gap. Their conductivity increases with an increase in temperature, which is responsible for the movement of electrons across the band gap by acquiring thermal energy. Resistivity of a semiconductor lie in the range of 10^{-5} to 10^{6} Ωm. Furthermore, the conductivity of semiconductor materials can be increased by introducing appropriate dopants, which expand their range of applications [11, 12].

1.2.3 Insulators:

Insulators are materials that are not conductive and have a wide band gap, typically greater than 3 eV. The band gap is so large that the conduction band is essentially empty because electrons lack the energy to overcome the barrier [11, 12]. Insulators possess high resistivity, ranges from 10^{11} to 10^{19} Ωm. The band gap for insulators, semiconductors, and conductors is illustrated in Figure 1.1.

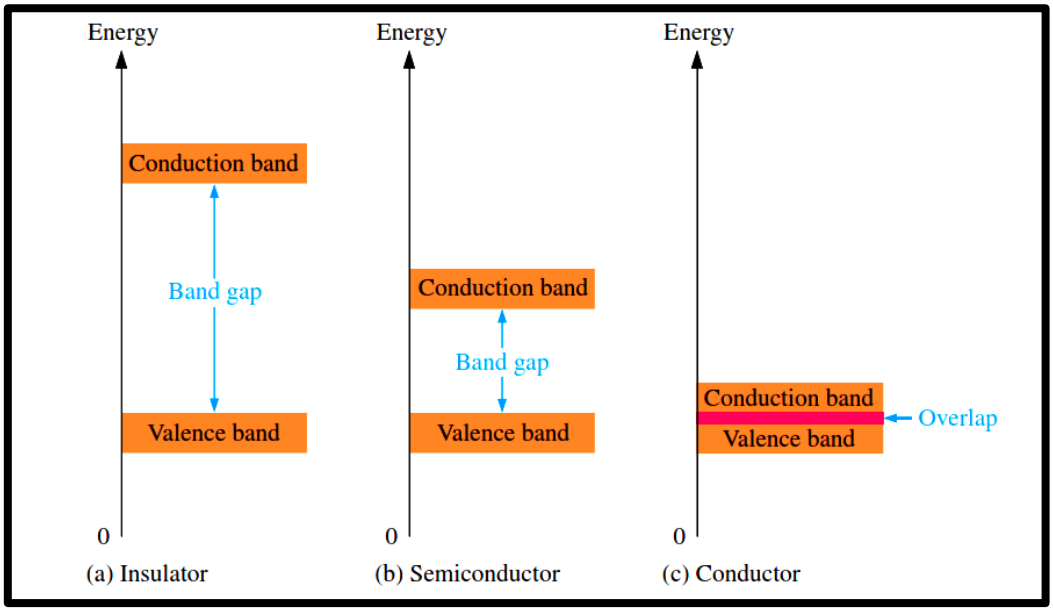

Figure 1.1 The Energy band gaps of (a) insulators, (b) semiconductors and (c) conductor [13]

1.3 Dielectric materials:

Dielectric materials act as insulators and exhibit polarization when subjected to an electric field, without the ability for charges to move freely throughout the material. Under

the influence of an electric field, positive charges are slightly displaced and move in the direction of applied field while the negative charges shift in the opposite direction, which results in polarization. As a result, an internal electric field is generated known as the depolarizing field. It opposes the applied field and which lead to a reduction in the net electric field within the dielectric [12]. Figure 1.2 illustrates the behavior of dielectric materials when subjected to electric field. The symbol E_0 represents the applied electric field while E_P represents depolarizing field.

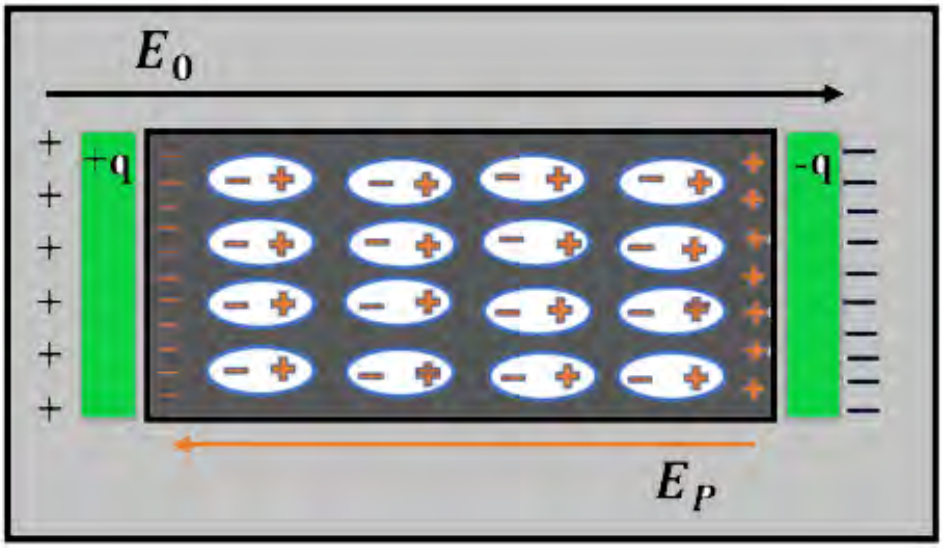

Figure 1.2 Effect of external electric field on Dielectrics

The dielectric constant or relative permittivity refers to the ratio between the permittivity of a dielectric material and the permittivity of free space (or vacuum). The dielectric constant is composed of two components and is considered a complex quantity. The dielectric constant represented as ε and consist of two parts: the real part ε', which characterizes the storage of electrical energy and the imaginary part ε'', which indicates the amount of energy absorbed or lost. The loss factor considers the impact of both conductivity and dielectric loss. Permittivity refers to the way in which a material interacts with an electric field, denoted by "ε", and is a complex quantity represented in equation 1.1 [14].

$$\varepsilon = \varepsilon' + i\varepsilon'' \qquad 1.1$$

1.4 Polarization:

When an electric field is applied to dielectric materials, they become polarized. The net polarization is defined as the induced dipole moment divided by the volume unit as given by equation 1.2.

$$\vec{P} = \frac{\Delta \vec{p}}{\Delta V} \tag{1.2}$$

Where $\vec{p}$ is dipole moment, V is net volume and $\vec{P}$ is total polarization. Another way to define electric polarization is the rearrangement of charges within a material resulting from the influence of an external electric field [11].

1.5 Types of Polarization:

Dielectric materials exhibit four primary forms of electric polarization.

1.5.1 Electronic Polarization:

When an external electric field is absent, the positively charged nucleus and negatively charged electronic cloud of an atom have the same center. However, when an external electric field is applied the electronic cloud shifts slightly from its original position which results in one end of the atom becoming positively charged, and the other end becoming negatively charged [15]. This process is induced by the external field applied and referred to as electronic polarization as shown in Figure 1.3. It typically takes about 10-15 seconds to activate as can be seen in Figure 1.7 [11]. Electronic polarization mostly occurs at high frequencies of electric field, and it can be observed in all types of atoms and molecules.

$$P_e = \alpha_e E \tag{1.3}$$

Where E is external electric field,

$$\alpha_e = 4\pi\mathcal{E}_o R^3 = 3\mathcal{E}_o V_{atm} \tag{1.4}$$

Where $V_{atm} = \frac{4}{3}\pi R^3$,

The electronic polarizability of an atom is denoted by α_e. It is the ratio of induced dipole moment in the system when external electric field is applied and is directly proportional to the volume of the electronic shell. It is independent of temperature and can be expressed in terms of the atom's radius R.

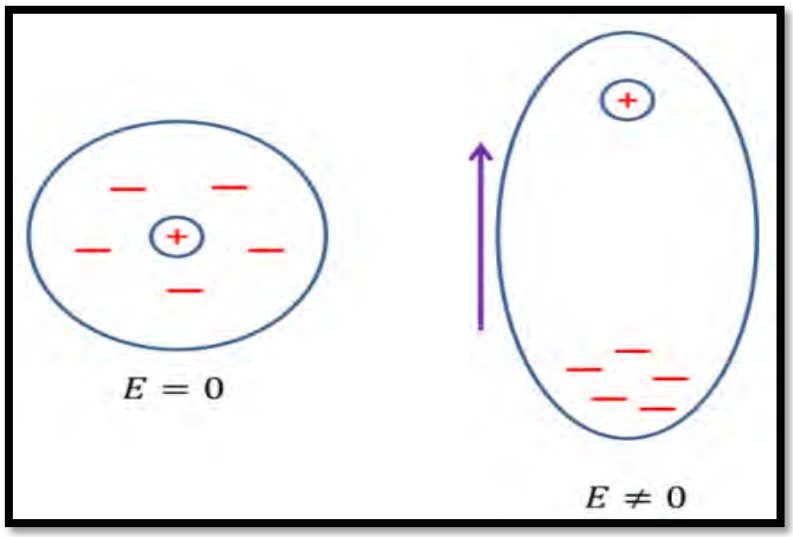

Figure 1.3 Shift of electron to center when $E \neq 0$ [15]

1.5.2 Ionic Polarization:

Ionic materials exhibit ionic polarization, which occurs because of the displacement of positively and negatively charged ions in opposite directions of an applied electric field as presented in Figure 1.4. Although ionic materials have dipoles and they do not possess net polarization in the absence of applied field because the dipoles of positive and negative ions cancel each other out. However, in the presence of applied field the cations and anions within the material slightly shift from their equilibrium positions and result in a net dipole moment [11]. Mathematically, induced dipole moment is given as.

$$P_i = \alpha_i E \qquad 1.5$$

Where E represents local electric field and α_i ionic polarizability.

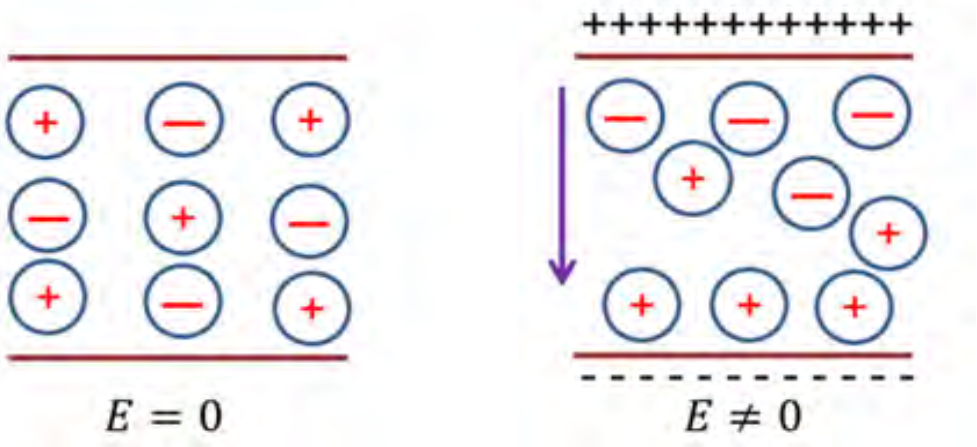

Figure 1.4 Displacement of ions when $E \neq 0$ [15]

1.5.3 Orientational Polarization:

Polar molecules such as H_2O and HCl, exhibit orientation polarization because of their permanent dipole moments. When there is no electric field, these polar molecules have zero net polarization because their permanent dipoles are randomly oriented in every direction which effectively cancelling each other out, thus resulting in zero average dipole moment [16]. In the presence of an electric field , the dipole moments within a material become oriented in the same direction as the applied field. This results in the causing of orientational polarization within the material as shown in Figure 1.5. The average dipole moment can be expressed as follows.

$$P_o = \alpha_o E \qquad 1.6$$

Where $\alpha_o = \frac{p^2}{3KBT}$,

E refers to external electric field and α_o is the orientational polarizability respectively. The above equation 1.6 shows that it is temperature dependent unlike electronic and ionic polarization.

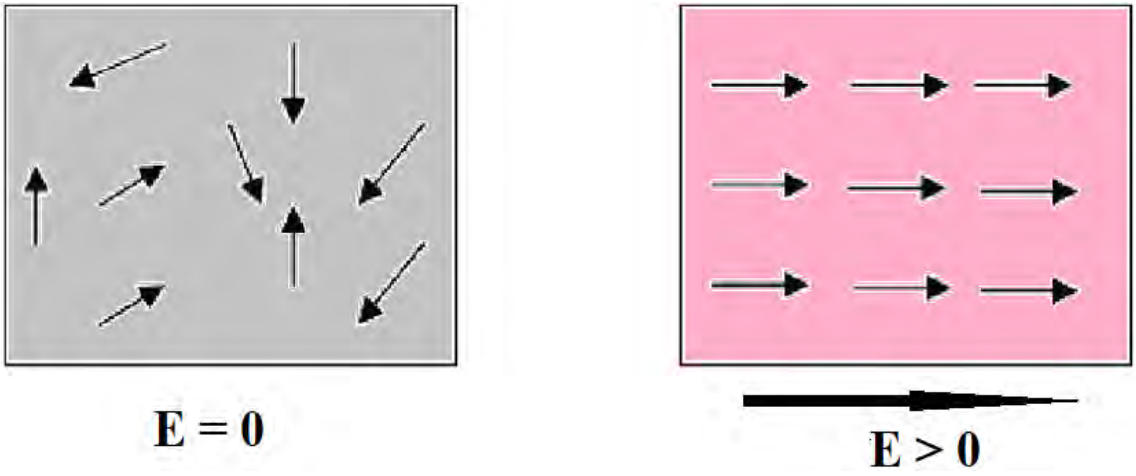

Figure 1.5 Orientational polarization [17]

1.5.4 Space charge Polarization:

A form of polarization that arises due to the accumulation of charge carriers at interfaces between different regions of a single crystal or at the boundaries between grains in polycrystalline dielectric materials. This type of polarization is also referred to as interfacial polarization. This form of polarization is commonly observed in ceramics [18]. Space charge is the distribution of electric charge over a particular region of space, rather than being

concentrated at specific point-like locations. Space charge polarization arises due to the presence of defect sites within the dielectric material, which cannot be eliminated. The presence of charges at grain boundaries contributes to the increment of dielectric constant. As the temperature increases these charges participate in conduction processes, which leads to the occurrence of a phenomenon called Maxwell-Wagner relaxation in dielectrics [16]. Figure 1.6 depicts the space charge polarization and mathematically it can be written as,

$$P_{sc} = \alpha_{sc} E \qquad 1.7$$

Where α_{sc} represent space charge polarizability.

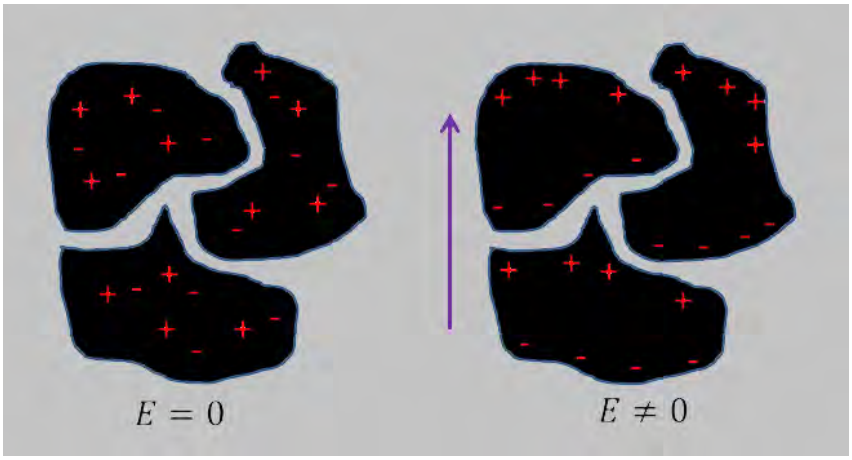

Figure 1.6 Space charge (Interfacial) Polarization [15]

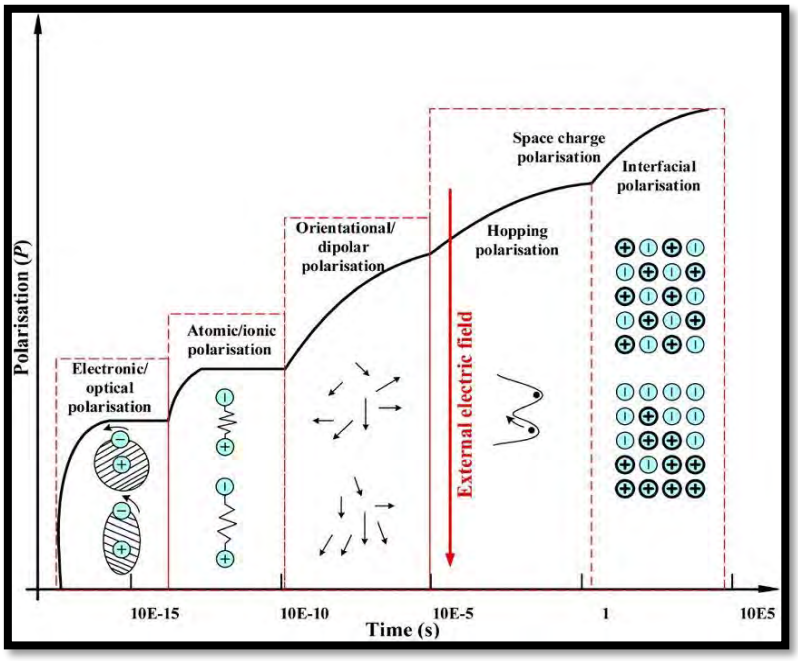

Figure 1.7 Mechanisms of polarization in dielectrics [11]

Dielectric materials exhibit total polarization because of the contributions made by all four of the known polarization mechanisms and are given in equation 1.8.

$$\vec{P}_{tot} = \vec{P}_e + \vec{P}_{ion} + \vec{P}_d + \vec{P}_{sc} \quad 1.8$$

Equation 1.9 represents the complete polarizability of a dielectric material.

$$\alpha_{tot} = \alpha_{sc} + \alpha_d + \alpha_{ion} + \alpha_e \quad 1.9$$

1.6 Dielectric Constant:

In dielectric materials, the induced polarization shows a direct proportionality to the applied electric field as given in equation 1.10.

$$\vec{P} = \varepsilon_o \chi \vec{E} \quad 1.10$$

Where χ is a dimensionless quantity known as electric susceptibility and ε_o is the permittivity of the free space [12]. Linear dielectrics are those which satisfy the above equation. Electrical displacement also known as electric flux density represented by $\vec{D}$ is defined as the displacement of charge per unit area across the dielectric in response to an applied field. Electrical displacement is given in equation as.

$$\vec{D} = \varepsilon_o \vec{E} + \vec{P} \quad 1.11$$

$$\vec{D} = \varepsilon_o \vec{E} + \varepsilon_o \chi \vec{E} \quad 1.12$$

$$\vec{D} = \varepsilon_o (1 + \chi) \vec{E} \quad 1.13$$

$$\vec{D} = \varepsilon \vec{E} \quad 1.14$$

$$\varepsilon = \varepsilon_o (1 + \chi) \quad 1.15$$

Where ε is dielectric permittivity of the medium. Dielectric constant depends on the following factors.

- Temperature
- Frequency
- Structure

1.6.1 Temperature:

Temperature affects a material intrinsic property known as the dielectric constant. Increase in temperature will result in increment of dielectric constant because of induced polarization caused by defects and space charges. The rapid rise in the dielectric constant at higher temperatures is caused by the accumulation of charges at grain boundaries (Space charge polarization). At high temperature, the polarization of material generates mobile charge carriers, increasing the dielectric constant even more [19, 20].

1.6.2 Frequency:

The resonance or relaxation frequency of different polarization mechanisms correspond to the frequencies at which they have a significant impact on the total dielectric constant. Resonance occurs when an external field's frequency corresponds with the natural frequency of electrons or ions which is normally around 10^{11} to 10^{15} Hz. The impact of alternating electric field frequency on the dielectric constant and various polarization mechanisms was shown in Figure 1.8. Electronic polarization and ionic polarization are dominant at high frequencies, while space charge polarization is dominant at low frequency [11]. Ionic polarization is active in the infrared range, electronic polarization is active in the ultraviolet-visible region, while orientational polarization is present in the microwave area as shown in Figure 1.8 [11, 21].

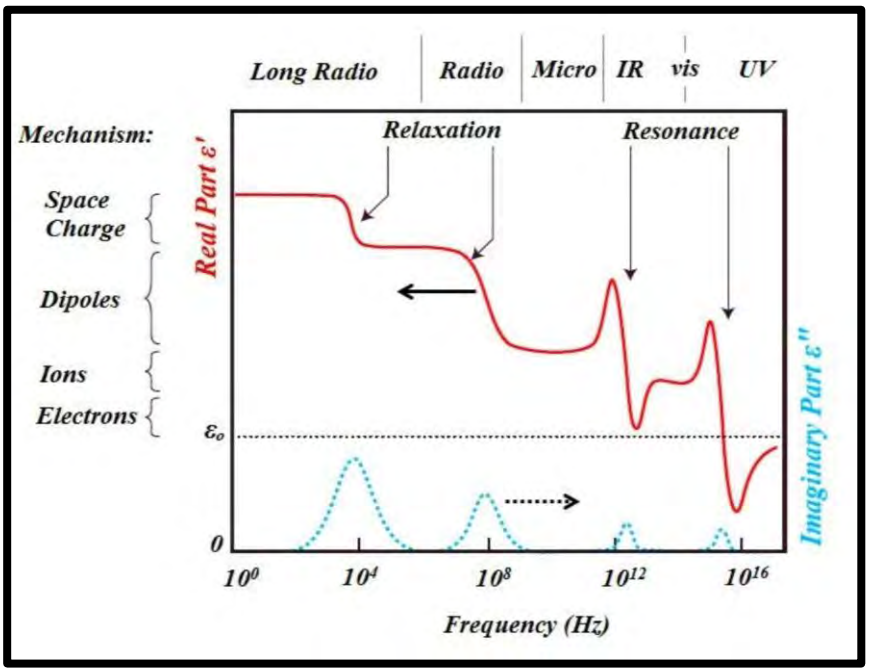

Figure 1.8 Real (ε') and imaginary component (ε") of dielectric constant [22]

1.6.3 Structure:

The dielectric constant depends on the nature of the material. Non-polar molecules have a low dielectric constant due to lacking permanent dipoles, while polar molecules exhibit a high dielectric constant because of permanent dipoles. Dipolar displacement length and dipole density are the two factors in polar molecules that affect the dielectric constant. A material having high density of permanent dipoles and large length of dipolar displacement will result in larger dielectric constant and vice versa [23, 24].

1.7 Piezoelectricity:

Materials that exhibit piezoelectricity can generate voltage under the application of mechanical stress or conversely, producing mechanical stress upon exposed to an applied electric field [25]. Piezoelectric effect is observed in those materials who possess a non-centrosymmetric crystal structure. In centrosymmetric crystal structure, dipoles cancel each other's effect which results zero net polarization [25]. Piezoelectric materials such as Barium titanate ($BaTiO_3$), Lead titanate ($PbTiO_3$) and PVDF are widely used due to their ability to generate electric charge under mechanical stress or produce mechanical stress in response to applied field [26]. These materials are highly valued for their functionality, that includes sensing, actuation, and biomedical applications etc. The piezoelectric effect observed in quartz is presented in Figure 1.9.

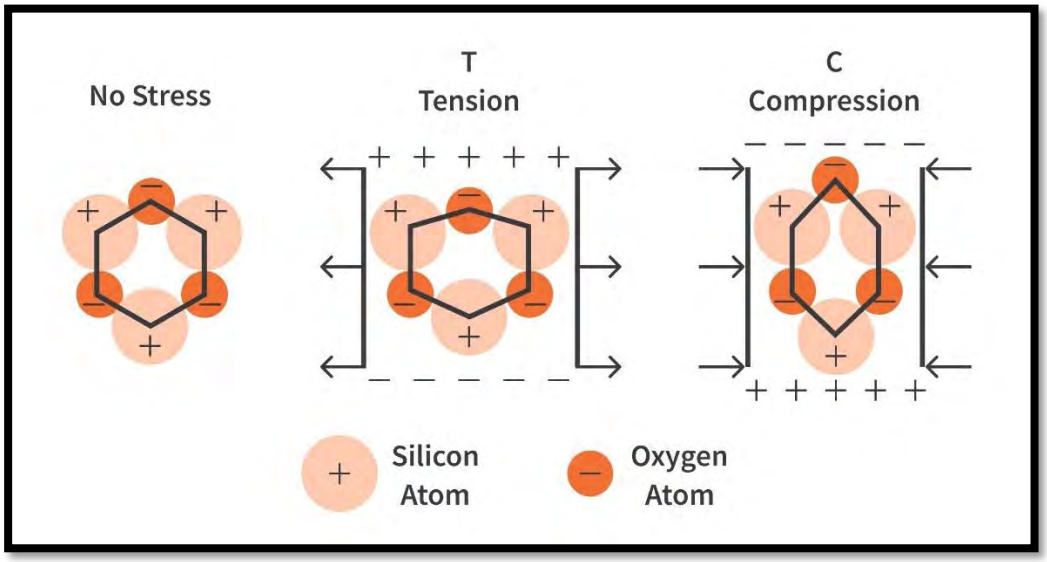

Figure 1.9 Piezoelectric effect in Quartz [27]

Two types of effects are observed in piezoelectric materials.

1. When a piezoelectric material undergoes compression or mechanical deformation, a subtle displacement occurs in the positions of its positive and negative charges, resulting in polarization. This phenomenon is termed as direct piezoelectric effect as illustrated in Figure 1.10 [11].

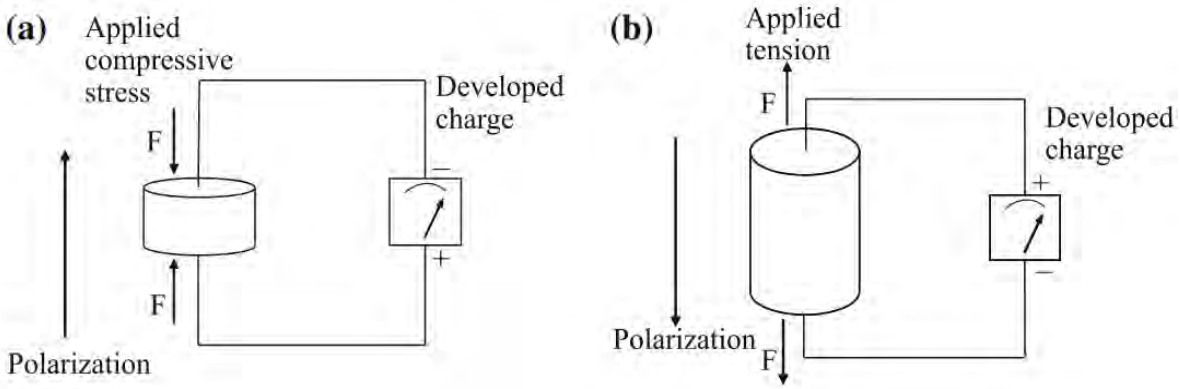

Figure 1.10 Direct piezoelectric effect (a) at applied compressive stress, (b) at applied tension [25]

2. The inverse or converse piezoelectric effect is another type of piezoelectric material. The converse piezoelectric effect is also known as the indirect piezoelectric effect and it is observed when an applied external field generate stress in the material as shown in Figure 1.11 [25].

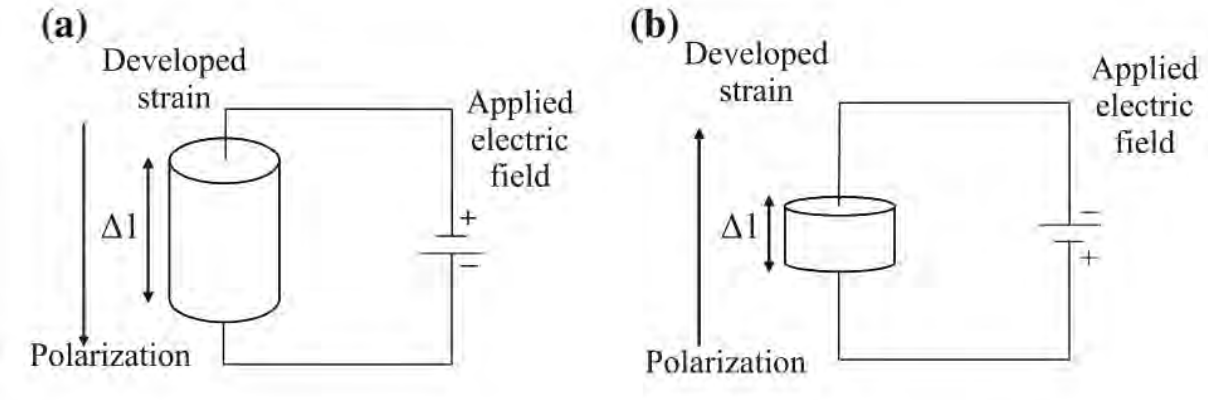

Figure 1.11 Inverse piezoelectric effect at applied electric field: (a) in upward direction, (b) in downward direction [25]

1.7.1 Piezoelectric polymer:

Organic compounds with long range order and a sizable molecular weight are known as piezoelectric polymers. These materials are known for having excellent flexibility and durability, when compared to other type of materials [28]. Based on their dipole moment and topology, organic lead-free piezoelectric materials are categorized as piezoelectric polymer. The molecular structure of the material controls the piezoelectric properties of bulk polymers. Among the most studied piezoelectric polymers are PVDF and its copolymer (PVDF-TrFE). Strong polarity, a high d_{33} co-efficient value (20-28 pC/N), remarkable stretchability, mechanical flexibility, excellent durability, biocompatibility, and low acoustic impedance are just a few advantageous features of PVDF and its copolymer. Despite these features, materials made of piezoelectric polymers have some limitations such as poor low temperature stability and substantial leakage current [29]. Due to their various mechanical and physical properties which make them fit for numerous applications. Polymer materials, especially those that have piezoelectric capabilities, are of great importance. These materials can transform different mechanical forces into voltage, such as wind, acoustic vibrations, or human movements (including walking, jogging, stretching, muscle movements, and breathing). They can also absorb energy from common ambient sources like vibrations, air flow and noise [30].

1.8 Pyroelectricity:

The pyroelectric effect is characterized by the change in the polarization of a material because of being subjected to heating or cooling. As the temperature changes, the atomic position of the material also shifts slightly from its neutral state, resulting to a change in the polarization of material. When the change in temperature is not uniform across the sample, a temperature gradient may induce a mechanical stress that triggers piezoelectricity in addition to pyroelectricity. If the temperature change is uniform, then only the pyroelectric effect will be observed [11]. Figure 1.12 represents the pyroelectric phenomena in PVDF.

Pyroelectric materials have significant applications, including infrared (IR) [31] detectors, thermal imaging, gas sensing, fire alarms and sterilization [32].

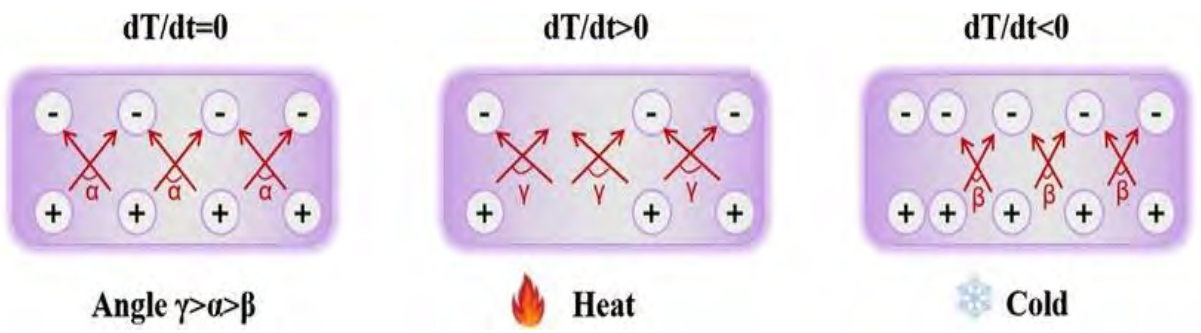

Figure 1.12 Pyroelectric effect in PVDF [33]

1.9 Ferroelectricity:

Ferroelectric materials are a unique type of insulator that exhibits spontaneous polarization. Spontaneous polarization arises without any external electric field due to the spontaneous alignment of dipole moment of each unit cell with its adjacent unit cells. The phenomenon of ferroelectricity is observed in crystalline structures which are ordered electrically. However, this alignment of dipole moments results in the formation of a domain structure that increases the net free energy of the system. To minimize this energy, the formation of multiple domains with opposing dipole moment directions occurs within a single crystal. As a result, the vector sum of all the dipole moments of these domains cancel the effect of each other and yielding a zero net dipole moment [11]. In the presence of external electric field, the disordered domains in ferroelectric material align themselves parallel in the direction of field applied which led to a net electric polarization within the crystal. In the absence of external field, the dipole moments do not entirely revert to their original disordered state and the material retains a residual polarization. The correlation between the electric field and polarization can be studied through a hysteresis loop [11]. Figure 1.13 illustrates the domain structure of ferroelectric material in the presence and absence of external electric field.

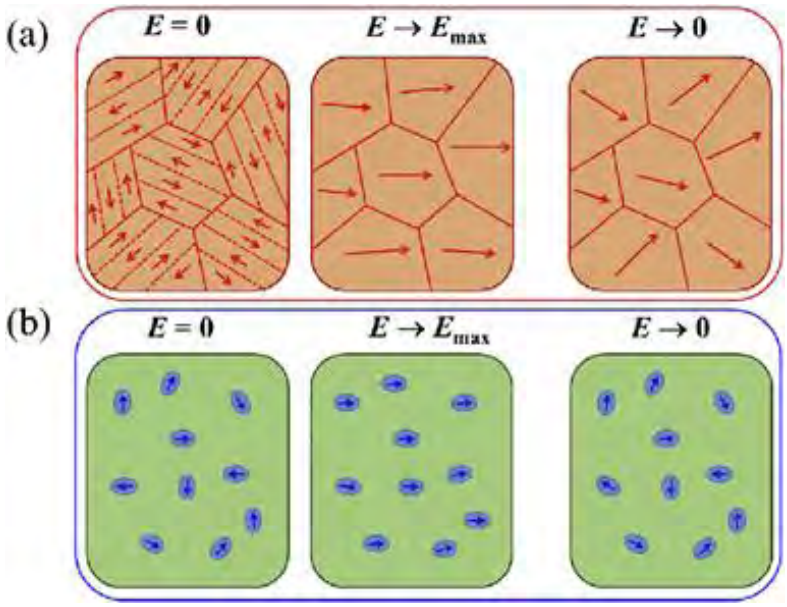

Figure 1.13 Domain structure in a ferroelectric material [34]

1.9.1 Ferroelectric hysteresis loop:

The correlation between the applied alternating electric field (E) and the intrinsic polarization (P) in ferroelectric materials is represented by a hysteresis loop, commonly referred to as the ferroelectric hysteresis loop or $P-E$ loop [35]. Figure 1.14 displays a hysteresis loop ($P-E$) for ferroelectric materials.

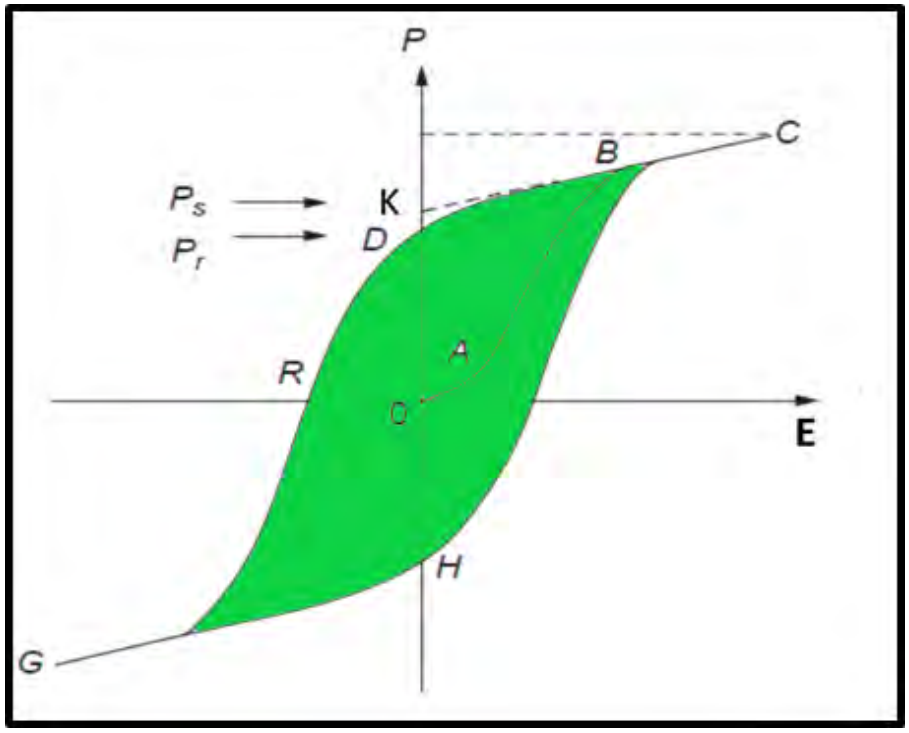

Figure 1.14 Schematic representation of ferroelectric ($P-E$) hysteresis loop [11]

In the ferroelectric hysteresis loop, the region where the domains are not switched due to insufficient electric field strength is referred to as the OA segment. As the electric field gradually increases, the randomly aligned ferroelectric domains begin to orient themselves parallel in the direction of applied field which lead to a rapid increase in polarization and represented by the segment AB. Point C is known as the saturation polarization (P_s). A this point, nearly all the ferroelectric domains are aligned in the field direction which result in the maximum achievable polarization [11].

The point D in the hysteresis loop represents the remanent polarization (P_r). The point where the electric field is zero but still polarization remains non-zero and indicates that some of domains are still aligned. The electric field then decreases to zero before gradually increasing in the opposite direction. At point R, the net polarization is zero and indicates that all domains have reverted to their original random orientations. This point is termed as the coercive field and is represented by E_c. As the electric field continues to increase in the opposite direction, the ferroelectric domains switch in the reverse direction which leads to a new saturation point in the opposite direction. In the opposite direction, the saturation point is termed as G. The cycle is completed at H. Where the electric field is again zero, representing the new remanent polarization point where domains are aligned in the reverse direction. In the ideal case, a symmetric hysteresis loop displays the same positive and negative values of saturation polarization (P_s), remnant polarization (P_r), and coercive field (E_c). Factors such as defects, thermal treatment, mechanical stress, and preparation conditions can impact the shape of a ferroelectric ($P - E$) hysteresis loop [36].

Ferroelectric materials possess both pyroelectric and piezoelectric properties, while the opposite is not necessarily true. An additional property of ferroelectric materials is their ability to exhibit reversible spontaneous polarization [35].

1.9.2 Phase Transition in ferroelectric materials:

Ferroelectric materials exhibit spontaneous polarization only below curie temperature (T_c). Above T_c, they behave as non-polar paraelectric materials. The ferroelectric phase transition that occurs above T_c is caused by a change in the unit cell structure, leading to a change in the spontaneous polarization of the material [20]. Once the temperature exceeds T_c, the ferroelectric properties of the material disappear entirely. T_c is the temperature where transition from ferro-electric to para-electric occurs and it varies among different materials. Above T_c, it is still possible to induce ferroelectric properties by applying an external electric

field that surpasses a specific threshold value. Furthermore, a significantly larger electric field can shift the T_c to a higher temperature.

When the temperature approaches T_c, the dielectric constant exhibits peculiar behavior by rapidly increasing to an exceptionally high value. Subsequently, after reaching T_c it follows the Curie-Weiss law and is expressed as [11].

$$\varepsilon = \varepsilon_o + \frac{C}{T - T_c} \qquad 1.16$$

Where C is the Curie-Weiss constant.

1.10 Factors Affecting Ferroelectric Hysteresis Loops:

There are some factors that affect the ferroelectric $P - E$ hysteresis loop and due to such factors, the hysteresis curves are unrelated to ferroelectricity either partly or completely. Three major factors that affect the $P - E$ hysteresis curves are as following.

- Dielectric permittivity
- Domain switching
- Electrical conductivity

Figure 1.15 illustrates the contribution of linear dielectrics, domain switching and electric conductivity in terms of current versus electric field.

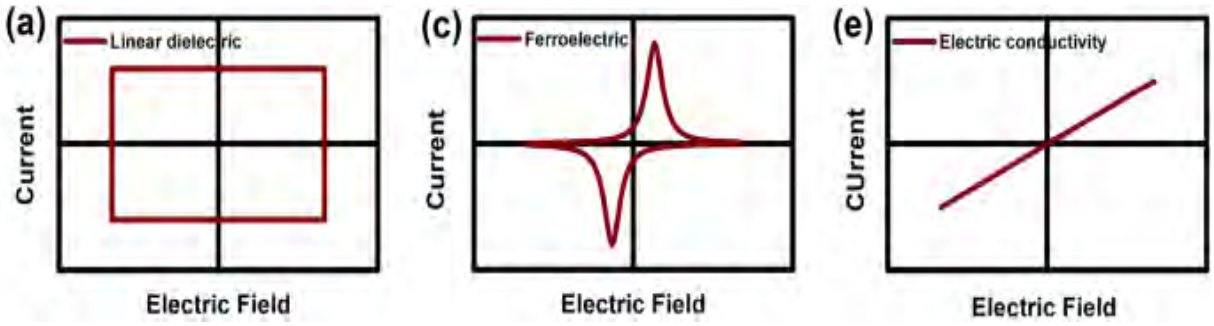

Figure 1.15 (a) Linear dielectric current (I) vs Electric field (E) (c) Ferroelectric current (I) vs Electric field (E) € Electric conductivity current (I) vs Electric field (E) [37]

Figure 1.16 illustrates the contribution of linear dielectrics, domain switching and electric conductivity in terms of current versus electric field.

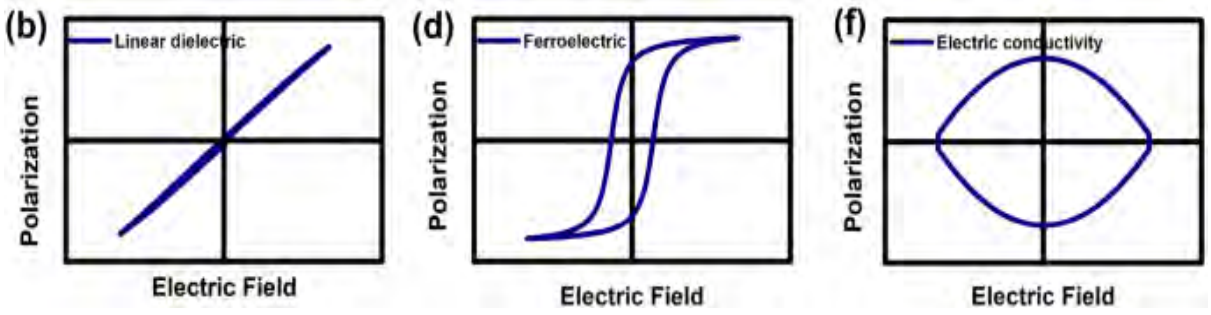

Figure 1.16 (b) Linear dielectric Polarization vs Electric field (d) Ferroelectric Polarization vs Electric Field (f) Electric conductivity Polarization vs Electric field [37]

1.10.1 Effect of Dielectric Permittivity:

A linear dielectric capacitor exhibits an ideal straight-line $P - E$ (Polarization-Electric field) graph and lacks ferroelectric properties. In this case, the dielectric permittivity is responsible for the current flow and resistivity is exceptionally high. Value of resistivity is greater than 10^{15} Ωm. Resistivity does not contribute to the current.

$$I = \frac{dQ}{dt} = \frac{d(CV)}{dt} \tag{1.17}$$

$$I = \frac{d}{dt}\left(\frac{\varepsilon AEd}{d}\right) = \frac{d(\varepsilon AE)}{dt} = \varepsilon A\frac{dE}{dt} \tag{1.18}$$

A represent area, d is a sample thickness, C is capacitance, V is voltage, and dE/dt is the rate of the applied electric field, where ε is the dielectric permittivity. Current is independent of electric field. A straight line showing non-hysteresis linear dielectric behavior [36].

1.10.2 Effect of domain switching:

Figure 1.16 (d) illustrates an ideal hysteresis $P - E$ loop. Near the coercive field, the occurrence of domain switching induces peaks in the current. As the electric field increases, the current decreases and eventually reaches zero. This signifies the complete switching of ferroelectric domains and lead to a saturated ferroelectric hysteresis loop [36].

1.10.3 Effect of Electrical conductivity:

The elliptical shape of ferroelectric hysteresis loop does not exhibit ferroelectric behavior. The waveform of both current and voltage is the same. With the increase in electric field current also increases.

$$I = \frac{V}{R} = \frac{Ed}{R} = \frac{EA}{\rho} \tag{1.19}$$

Where $$R = \frac{\rho d}{A}$$

R stands for electrical resistance and ρ is for electrical resistivity. According to equation 1.19, when voltage increases resistivity decreases, due to which conductivity increases. The non-hysteresis loop indicates that domain switching makes no contribution at all [36]. Additionally, the ferroelectric hysteresis loop is affected by temperature, frequency, and texture.

1.10.4 Effect of temperature:

The shape of the ferroelectric hysteresis loop is highly affected by temperature due to the temperature dependent nature of dielectric permittivity, electrical conductivity, and spontaneous polarization. As temperature increases, the current peaks that represent domain switching decreases. As temperatures exceed the T_c, a transition occurs from ferroelectric state into a paraelectric state and exhibiting a linear behavior. Figure 1.17 illustrates the temperature dependent ferroelectric hysteresis loop, where the loop gradually becomes sharper, thinner, and eventually disappears with increase in temperature [38].

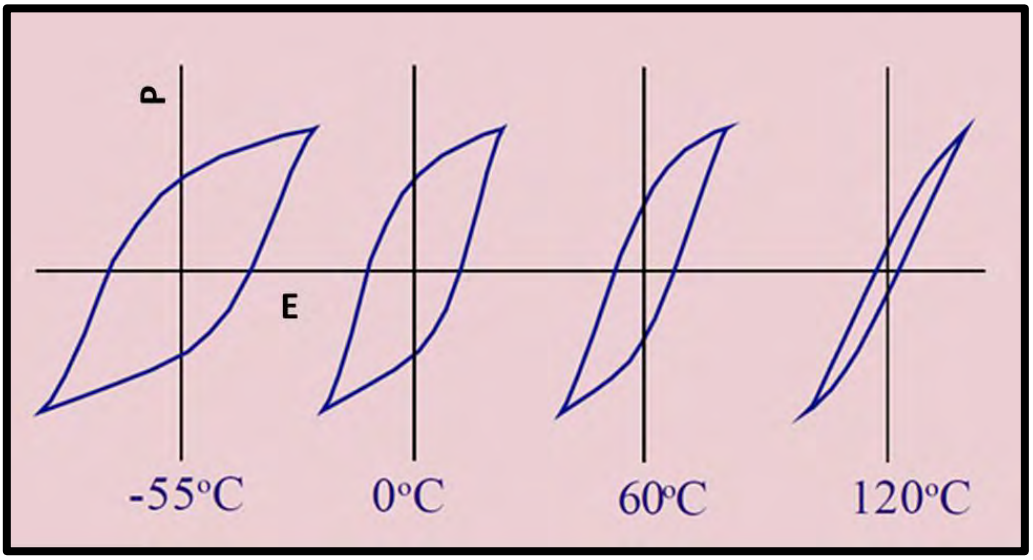

Figure 1.17 Temperature dependent ferroelectric hysteresis loops [38]

1.10.5 Effect of frequency:

The ferroelectric $P - E$ hysteresis loop is affected by frequency. At higher frequencies coercive field also experiences an increase. It is because higher frequencies correspond to a greater rate of change in the switching and electric field. As a result, the remanent polarization is reduced and the total polarization which was achieved at the maximum electric

field is also reduced. Therefore, with the increase of frequency the coercive field increases and total polarization decreases. Figure 1.18 illustrates ferroelectric hysteresis loop dependence on frequency [36].

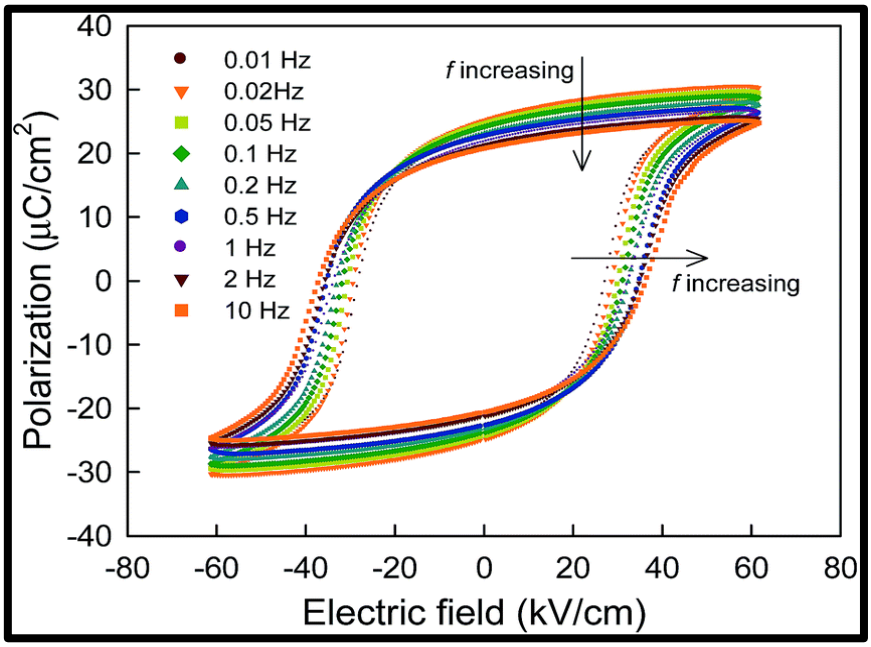

Figure 1.18 Frequency dependent ferroelectric loop [39]

1.11 Poly (vinylidene fluoride) (PVDF):

PVDF stands for Poly (vinylidene fluoride), exhibits semi-crystalline properties. The repeating unit that PVDF is made up of is $–(CH_2\text{-}CF_2)$-. If the molecular segments are arranged in a manner where they are 180° apart from each other with respect to the carbon backbone, it is referred to as a trans bond (T). In contrast, when the angle between them is either +60° or -60°, it is termed as a gauche bond (+G/-G). PVDF Curie temperature (T_c) is approximately 60 °C and glass transition temperature (T_g) is 35 °C. PVDF has 35-70 % crystallinity, and it depends on the method of preparation. The van der Waals radius for Fluorine (F) is 1.35 Å and for Hydrogen (H) it is 1.20 Å. A density range of 1.75 to 1.78 g/cm³ characterizes commercial PVDF. PVDF homopolymer in its molten state has a density ranging from 1.45-1.48 g/cm³ at 230 °C and 1.0 bar. The melting point of PVDF lie in the range of 155-192 °C [40]. Figure 1.19 presents the molecular structure of PVDF.

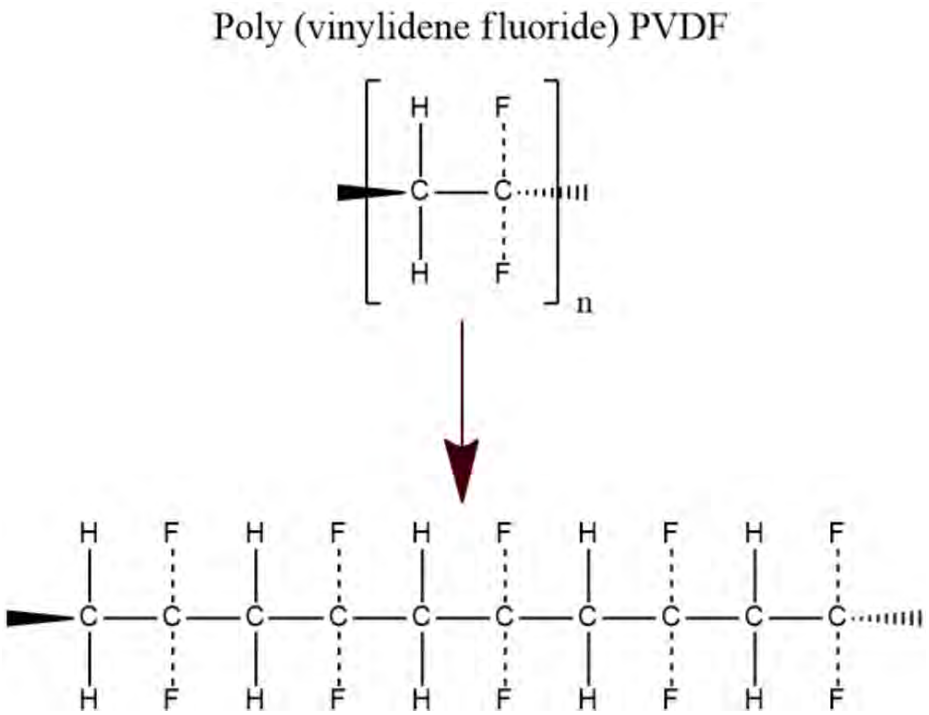

Figure 1.19 Molecular structure of PVDF

PVDF exceptional mechanical properties as well as its chemical and thermal stability, along with high piezo and pyro coefficients, make it an attractive material for numerous applications which includes transducers, detectors, sensing, memory devices, and biomedicine [41]. Furthermore, ferroelectric, and piezoelectric properties of PVDF are significantly dependent on its structural composition. PVDF exist in four primary forms: alpha (α), beta (β), gamma (γ), and delta (δ) phases.

1.11.1 Alpha phase:

The alpha (α) phase of PVDF exhibits a $TG^{+}TG^{-}$ chain conformation. The molecular chains in the α-phase of PVDF is arranged in an anti-parallel manner, making a non-polar structure. This phase is the most stable and is particularly suitable for mechanical applications. On the other hand, the delta (δ) phase is a polar variant of the α-phase, exhibiting ferroelectric properties. In δ-phase, every other molecular chain is rotated at an angle of 180° which aligned the dipoles parallel and making it polar [40]. For the α-phase of PVDF, the lattice parameters are measured to be a = 4.96 Å, b = 9.64 Å, and c = 4.62 Å [40]. α-phase can be transformed to β-phase through stretching, to gamma phase via thermal treatments, and to delta phase through poling at applying high fields [3].

1.11.2 Beta phase:

The beta (β) phase of PVDF is a polar phase characterized by chains oriented in a TTTT configuration, where T is the symbol for trans bond that maintains alignment with the carbon backbone within the same plane [42]. In this arrangement, dipoles are oriented perpendicular to the chain axis and each unit cell contains two chains with dipoles pointing in the same direction. PVDF in the β-phase has a crystal structure with hexagonal symmetry, and its lattice parameters are measured to be a = 8.58 Å, b = 4.91 Å, and c = 2.56 Å. The β-phase of PVDF is considered as the most thermodynamically stable phase [40]. β-phase can be obtained by stretching α-phase near its melting point [3]. Off all the phases, the β-phase have the best piezoelectric and ferroelectric properties [40]. The non-zero dipole moment arises in this phase because H_2 and F_2 are located on opposite sides of the carbon backbone [43]. Figure 1.20 illustrates the different methods used to achieve the β-phase from all the other phases.

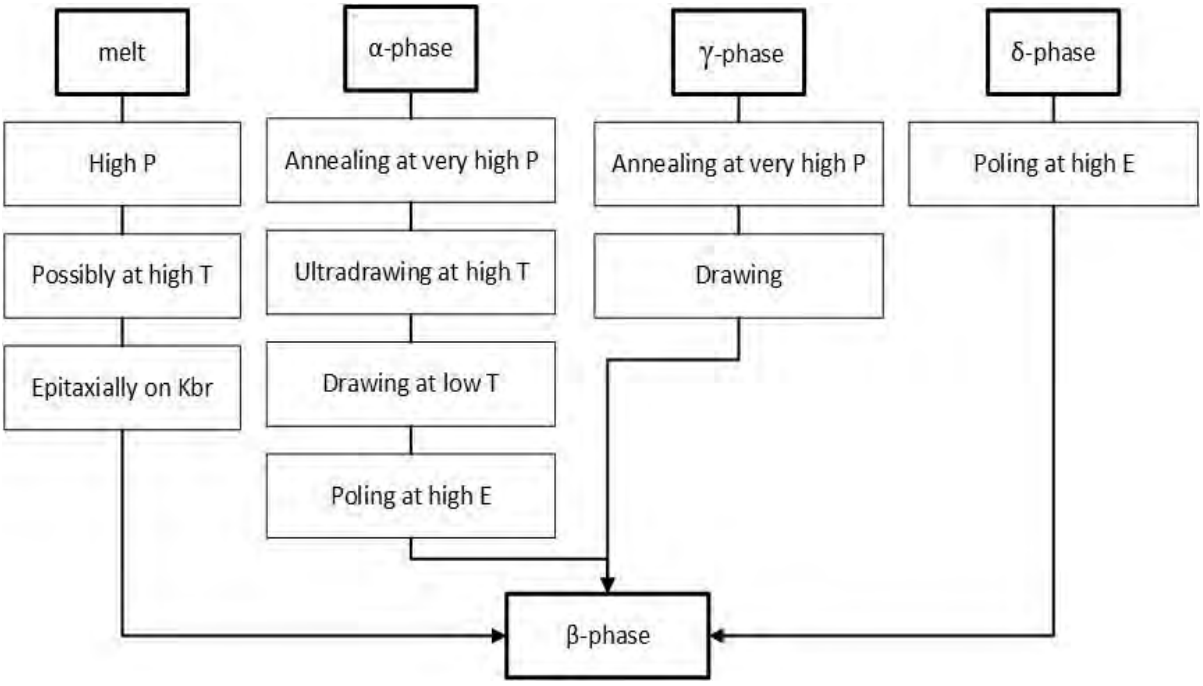

Figure 1.20 Different Methods to achieve β-phase from different phases [44]

1.11.3 Gamma phase:

The gamma (γ) phase exhibits a $T_3G^+T_3G^-$ conformation and has lattice parameters of a = 4.97 Å, b = 9.66 Å, and c = 9.18 Å. The γ-phase has a density of 1.97 g/cm³. γ-phase density of dipole moments is lower than that of the β-phase [40]. Isothermal crystallization at

high temperatures may results in formation of γ-phase [45]. The phase under consideration is ferroelectric. It exhibits lower polarization when compared to β-phase. Additionally, the ε – phase is referred to as the non-polar version of the γ-phase [45]. Figure 1.21 represents the conformation of PVDF phases.

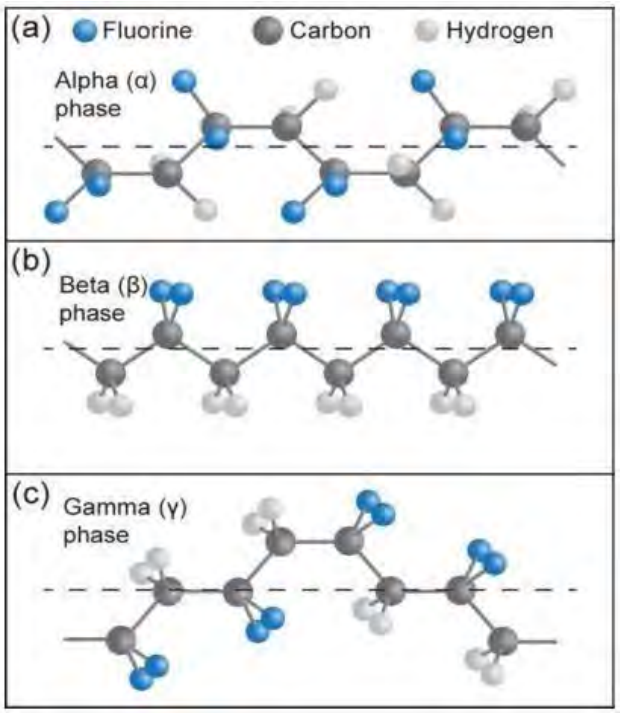

Figure 1.21 Conformation of PVDF (a) α-phase (b) β-phase (c) γ-phase [46]

1.12 Defects in PVDF:

Commercially available PVDF is composed of (-CH_2-CF_2-) repeating units, although it may contain some defects. The defect density of commercially available PVDF polymer is approximately 4-5 %. PVDF contains two types of defects known as Head-to-Head (HH) and Tail-to-Tail (TT) defects. HH defect exhibits (-CF_2-CF_2-) while TT defect has (-CH_2-CH_2-) crystal structures, respectively. The formation of one defect is closely followed by the creation of the other, resulting in their existence as pairs referred to as HHTT [47].

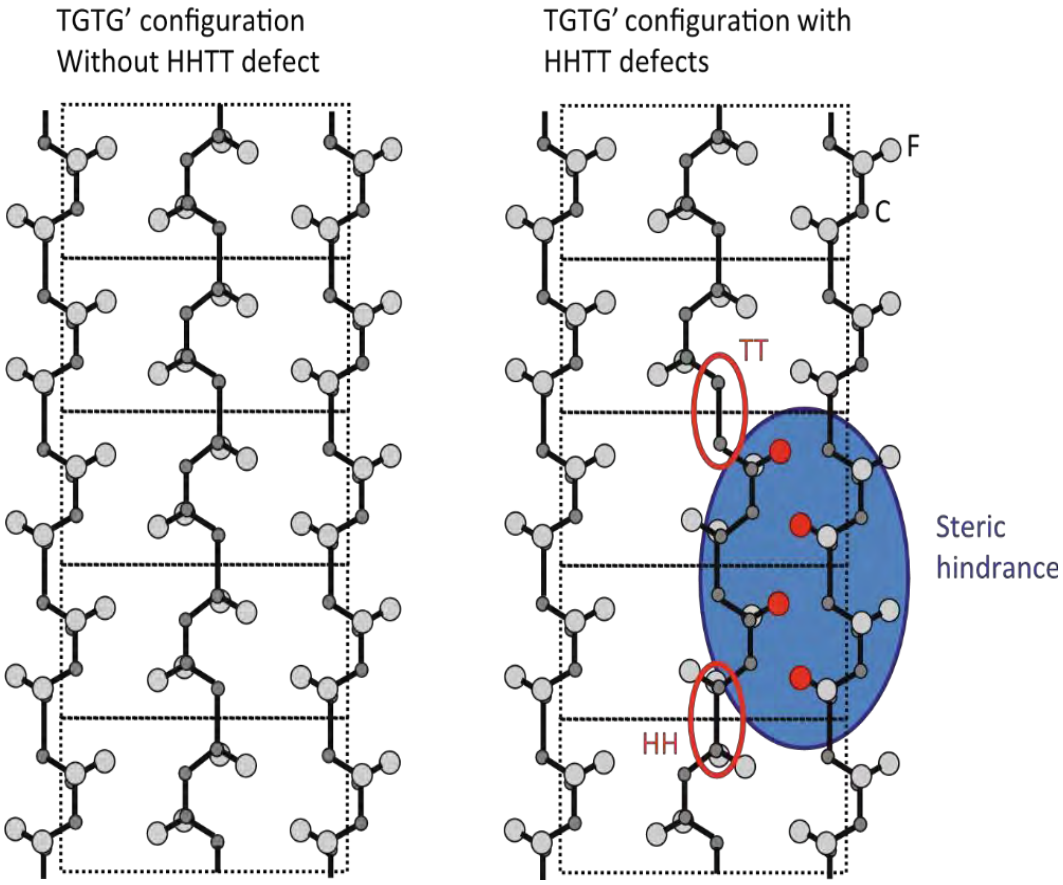

Figure 1.22 PVDF α-phase Steric Hindrance [44]

- In α-PVDF, the steric hindrance between neighbouring chains is caused by the presence of HH and TT defects. This defect led to an increase in energy of the crystal. The large radius and electronegativity of fluorine atoms causes hindrance with adjacent chains, which is highlighted by the red color in Figure 1.22. The formation of α-phase is favored when the defect density is limited to 10% or below [44].
- In contrast, the steric hindrance caused by HH and TT defects in the β-phase structure is not significant as illustrated in Figure 1.23. The increase in energy caused by such defects in the β-conformation is very small, due to which β-phase is more stable than α-phase. The β-conformation remains more stable even the defect density exceeds 10% [44].

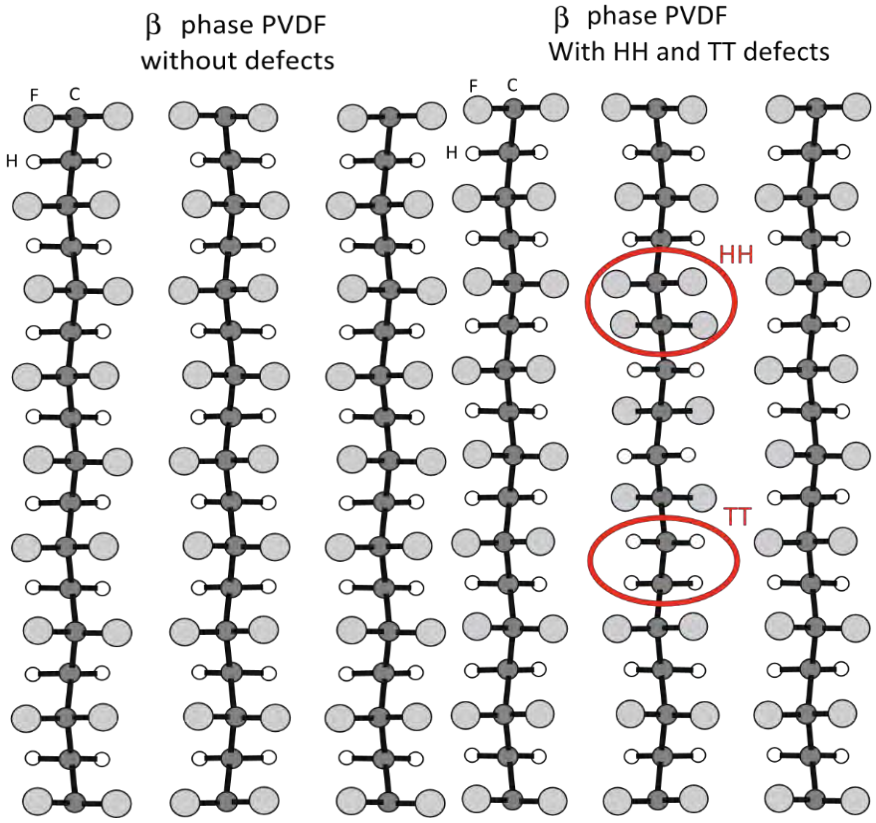

Figure 1.23 PVDF β-phase no Serious Steric Hindrance [44]

1.13 Poly (vinylidene fluoride-trifluoroethylene) P(VDF-TrFE):

P(VDF-TrFE) exhibits a semi-crystalline structure. It is composed of two monomers, namely VDF and TrFE. TrFE is a chemical abbreviation for CHF-CF_2 [48]. Melting temperature (T_m) of P(VDF-TrFE) can vary from 55-128 °C depends on the quantity of TrFE content present in the polymer. However, its Curie temperature (T_c) is lower than its T_m [49]. The ferroelectric property observed in copolymers is a result of the presence of a crystalline β-phase. In β-phase all polymer chains have trans (TTTT) configuration, and the fluorine atoms are arranged unilaterally in the chain [50]. Addition of TrFE content into the copolymer favor the trans bonds over gauche bonds due to the replacement of hydrogen with fluorine. The large size of the fluorine atom leads to steric hindrance of neighboring gauche bonds. The addition of a minimum of 20% TrFE content to VDF may cause significant steric hindrance in the α-conformation, but not in the β-conformation [44].

To attain ferroelectric properties in the copolymer, it is ideal to have TrFE content ranging from 90/10 to 70/30. If the TrFE content is increased beyond this range, the resulting copolymer will result a decrease in ferroelectric properties due to decrease in crystallite size [44]. Figure 1.24 represents the molecular structure of P(VDF-TrFE).

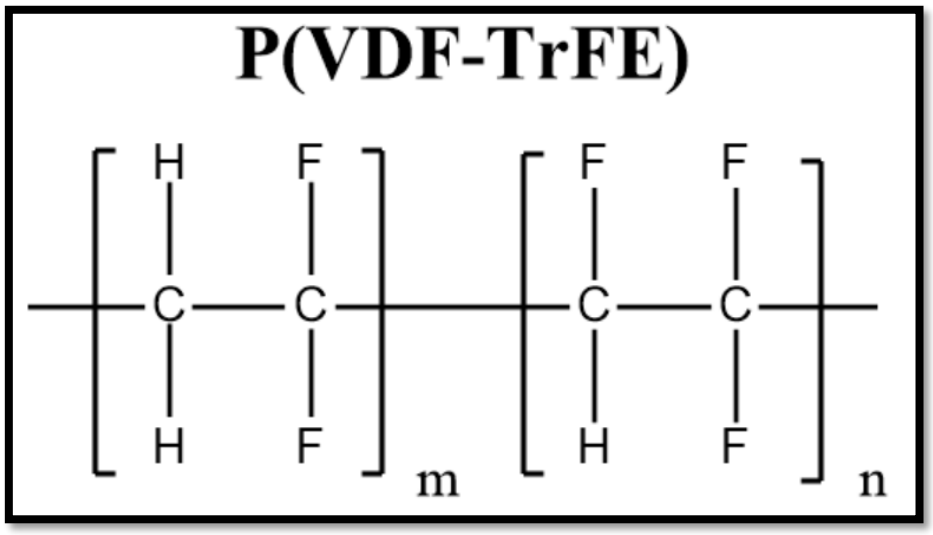

Figure 1.24 Molecular structure of P(VDF-TrFE)

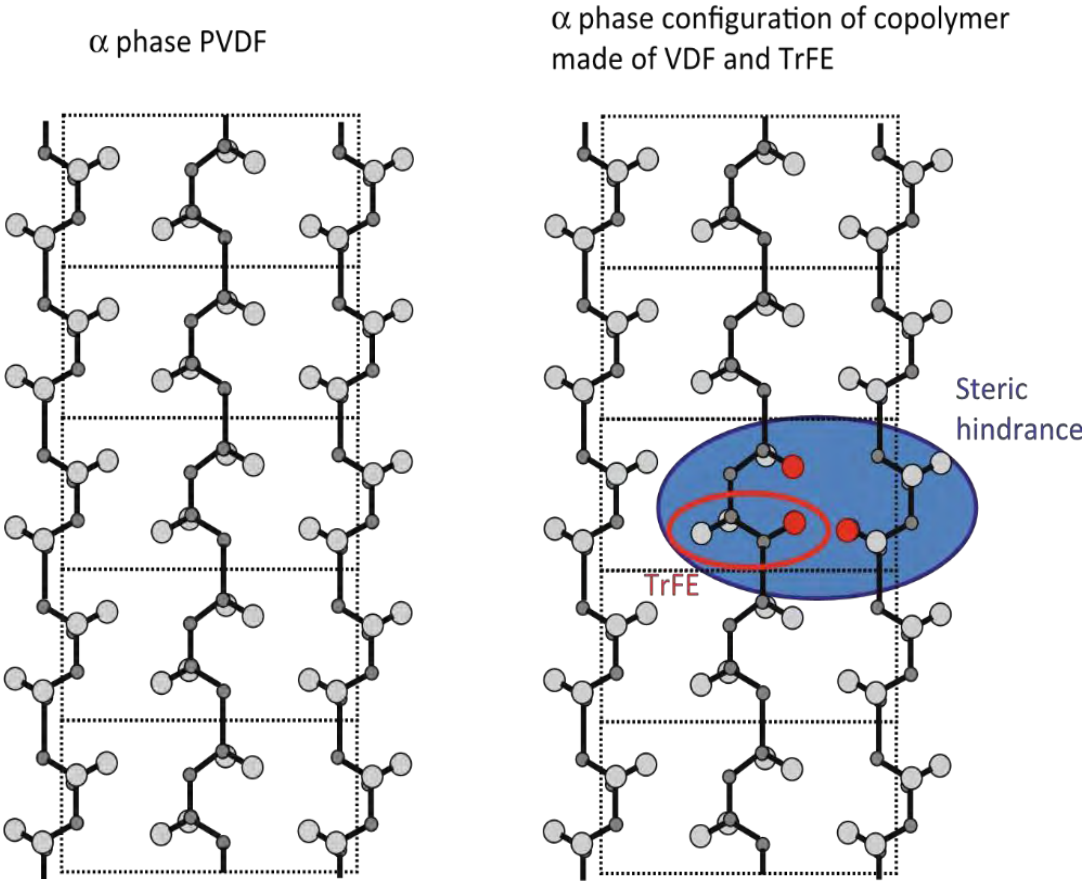

Figure 1.25 Effect of steric hindrance on α-phase [44]

Addition of TrFE monomers into the PVDF chain functions in a comparable manner to HH and TT defects. The addition of TrFE content in PVDF raises the energy level of the α-phase and result in an unstable conformation as represented in Figure 1.25. When the TrFE content surpasses 20%, severe steric hindrance occurs between the fluorine atoms in the α-

phase and the copolymer directly crystallizes into the ferroelectric β-phase. The steric hindrance caused by TrFE monomers in the β-conformation is relatively minor as shown in Figure 1.26 and making it a more stable configuration for copolymers with TrFE content exceeding 20% [40].

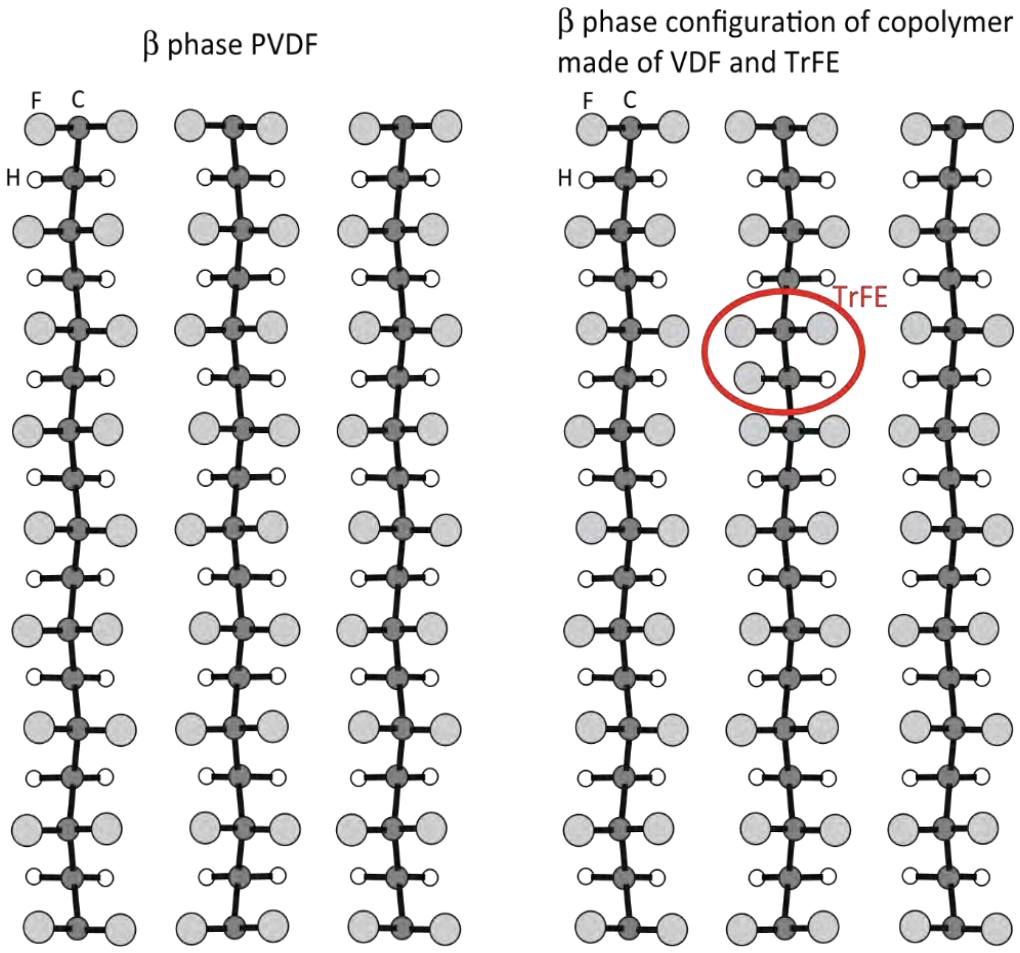

Figure 1.26 Effect of steric hindrance on β-phase [44]

1.14 Indium tin oxide (ITO):

Indium tin oxide (ITO) is widely used as an electrode material in various scientific fields because of its optical transparency and high conductivity properties exhibited by ITO films. Because of these properties, ITO films have been successfully utilized in several devices including electrochromic devices, photovoltaics, sensors, plasmonic devices, and light-emitting diodes [51].

1.15 Applications of PVDF and P(VDF-TrFE):

PVDF and P(VDF-TrFE) are well known for sensing. Both the materials possess piezoelectric property which makes them suitable for strain, vibration, pressure, and temperature sensing.

1.15.1 Energy harvesting performance of P(VDF-TrFE) bilayer with graphene oxide:

Ferroelectric materials have gained significant attention in recent years due to their vast applications in energy harvesting, particularly because of their piezoelectric properties. Ferroelectric polymers have the advantage of flexibility and the ability to withstand larger strains as compared to inorganic, making them attractive for converting mechanical vibrations into usable energy. In this study, improved performance of piezoelectric energy harvesting achieved using bilayer sheets composed of poled P(VDF-TrFE) and graphene oxide (GO) [52].

The sheets are fabricated through drop casting with a thickness of approximately 30 μm. To enhance the ferroelectric crystalline phase, the sheets were annealed for 2 hours at 135 °C. After annealing, the films were cooled naturally to room temperature. Subsequently, all the prepared sheets were poled at an applied field of 30 MV/m. For electrode fabrication, ITO is used as bottom electrode, while the top electrode was sputtered coated gold. The P(VDF-TrFE) and GO bilayer sheets were prepared by drop casting technique. For optimization, the thickness of GO is varied for better output. At thickness of 20-30 μm the output voltage increases up to 4 V. From 3-20 μm, an increment in output voltage is observed which is due to the higher charge in graphene oxide [52].

Poled P(VDF-TrFE) showed approximately 1.40 V output voltage. The bilayer, with non-poled P(VDF-TrFE) layer delivers a poor response and generates approximately 0.3 V output voltage. In this case, the output voltage corresponds to the electrostatic component. The bilayer, with poled P(VDF-TrFE) generates maximum voltage equals to approximately 4.3 V [52]. The mechanism of bilayer films is presented in Figure 1.27.

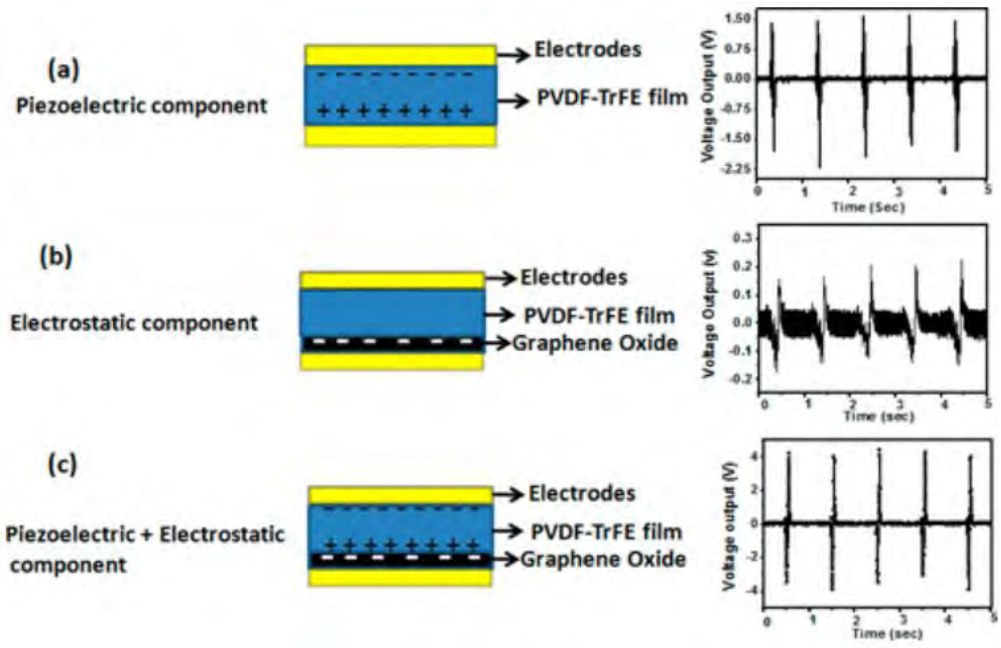

Figure 1.27 Mechanism of bilayer films (a) Poled P(VDF-TrFE) response (b) Response of non-poled P(VDF-TrFE) with electrostatic layer (c) Response of bilayer film with both components [52]

1.15.2 PVDF Piezoelectric nanogenerator for respiration and healthcare monitoring:

For respiratory and healthcare monitoring a flexible and wearable piezoelectric nanogenerator is fabricated. The fabrication process involved polarizing a thin film of Poly (vinylidene fluoride) on a silicone substrate by using electrospinning process. The electrical property of resulting flexible nanogenerator was then studied. Nanogenerator is primarily composed of three main components: (a) the piezoelectric layer, after compression the average thickness of PVDF is 200 µm. (b) electrodes; gold is used as top and bottom electrode component (c) elastic substrate, silicon is used as elastic substrate. At first, the PVDF film is polarized, and all the dipoles are aligned parallel to applied field. The dimensions of the piezoelectric active sensor (PEAS) are $42\ mm \times 20\ mm \times 0.6\ mm$. The PEAS with all its components is represented in Figure 1.28 [53].

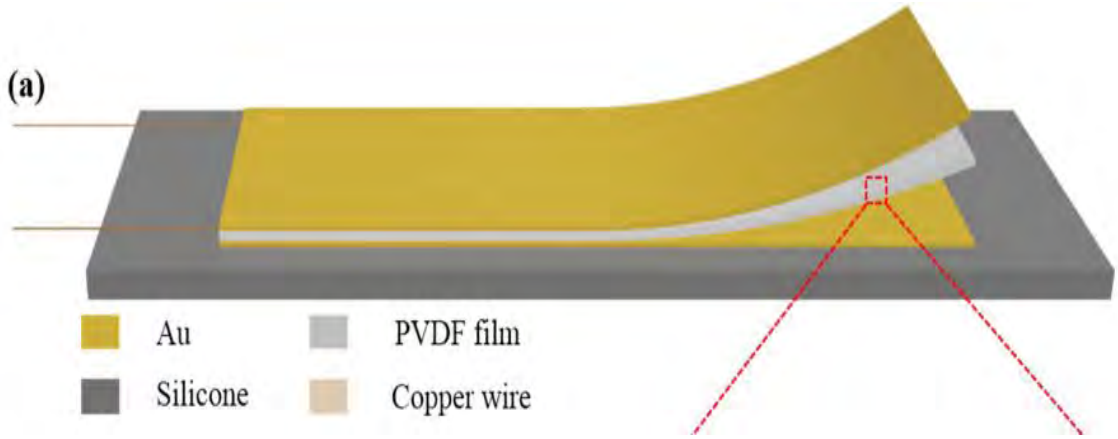

Figure 1.28 Piezoelectric active sensor (PEAS) [53]

Once the PEAS (Piezoelectric active Sensor) gets connected with bandages on both sides, it can be comfortably worn to any part of human body to detect respiratory signals. The excellent flexibility of the PVDF film and silicone substrate allows the PEAS to worn on different parts of human body [53].

Figure 1.29 (a) illustrates when nanogenerator (NG) is attached to human chest. To measure the respiratory signal a system named Biopac MP150 is used. It measures signals at different frequency. 20 seconds data is recorded on both open circuit voltage output and Biopac MP150. The open circuit voltage generates approximately 70 mV as illustrated in Figure 1.29 (b) and (c) represents the respiratory signal measured through Biopac MP150 [53].

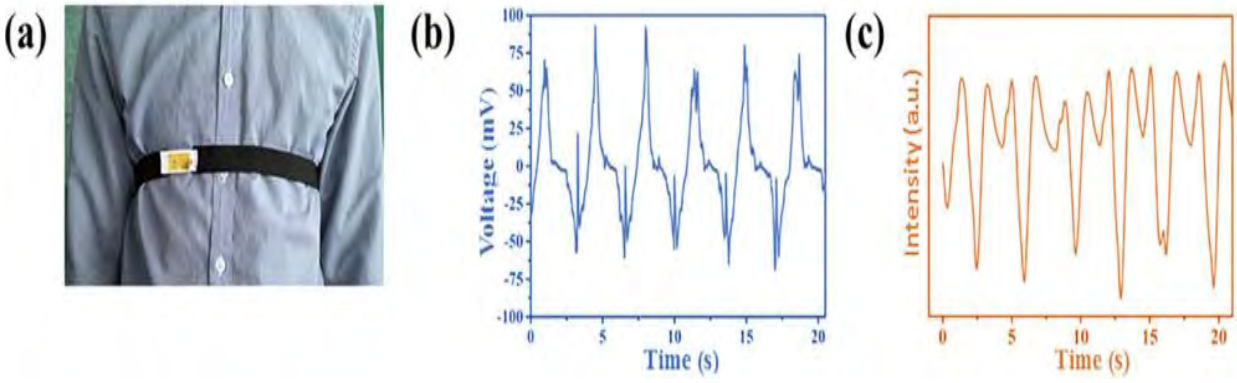

Figure 1.29 (a) NG connected to human chest (b) Open circuit voltage response (c) Respiration signals [53].

For healthcare monitoring PEAS is connected to the wrist of human body for the detection of muscles and tendons movements as shown in Figure 1.30 (a). PEAS shows

different response for different movements of arm muscles which indicates that it can detect small movements of tendons and muscles. It can also detect the vibration of vocal cards when PEAS is connected to throat as in Figure 1.30 (b). PEAS shows no response to silent state of vocal cords. But a signal is observed when the volunteer is speaking as presented in Figure 1.30 (c) [53].

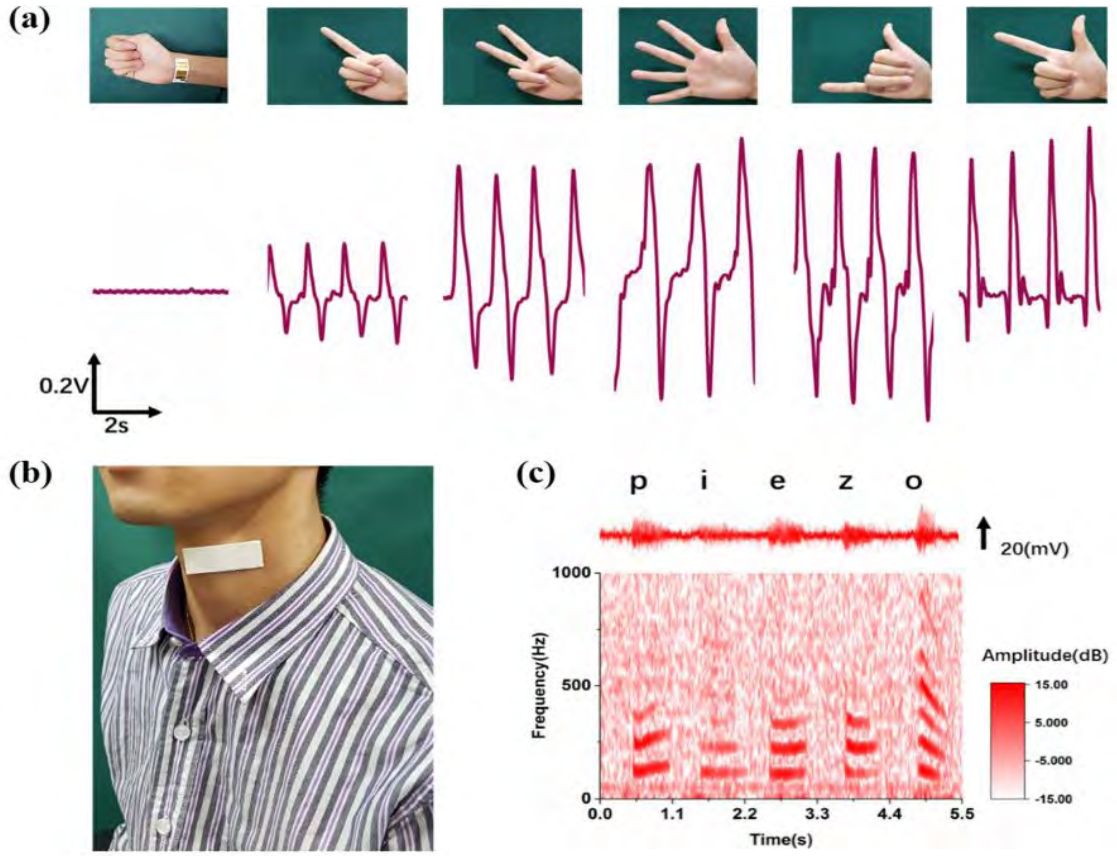

Figure 1.30 (a) PEAS connected to wrist for health care monitoring (b) PEAS connected to throat (c) Response of PEAS after a volunteer spoke the letters P, I, E, Z, O and sonogram of short time Fourier-Spectrum of the signal generated [53]

1.16 Motivation:

Ferroelectric PVDF has received the most attention amongst all the polymers due to its distinctive qualities, such as its remarkable pyroelectric, piezoelectric properties, high dielectric constant, and ease of manufacturing. PVDF is a semicrystalline material. PVDF is used widely in electronic components due to its minimal water absorption, flexibility, chemical inertness, thermal stability, and non-toxicity. PVDF exists in a variety of polymorphs (α, β, γ, and δ). Among these polymorphs, β-PVDF exhibits excellent ferro-electric, pyro-electric, and piezo-electric properties. β-PVDF exhibits higher piezoelectric coefficient (d_{33}) when compared with PVDF due to which β-PVDF is more suitable and attractive for applications like ultrasonic transducers, memory devices, biomedicines, and actuators [54].

Materials that have high dielectric constant (capacitance), low dielectric loss (dissipation), and high dielectric strength (E_b) are suitable for energy storage devices, electric powered vehicles, capacitors, actuators, sensors, piezoelectric transducers, and many other electronic applications. Organic and in-organic are the two types of dielectric material. The disadvantage of inorganic dielectrics includes brittleness, and they have a very low dielectric strength (E_b). Mostly in-organic dielectrics are ceramics and metal oxides. High temperature is required for their processing. In contrast, organic dielectrics (such as polymers) have a very high dielectric strength (E_b) and are very flexible. Even at low temperatures, their processing is possible. P(VDF-TrFE) possesses large dielectric constant value as compared to PVDF and β-PVDF. This makes P(VDF-TrFE) an attractive candidate for capacitor application. Moreover P(VDF-TrFE) also exhibits a larger d_{33} value and remanent polarization (P_r) when compared with PVDF and β-PVDF, due to which P(VDF-TrFE) can be used as flexible piezoelectric material [55, 56].

Chapter 2 Characterizations and Techniques

In this chapter, a detailed discussion of the experimental methods utilized to look over the structural and electrical properties of polymer films. A flowchart for all the characterizations is given in Figure 2.1.

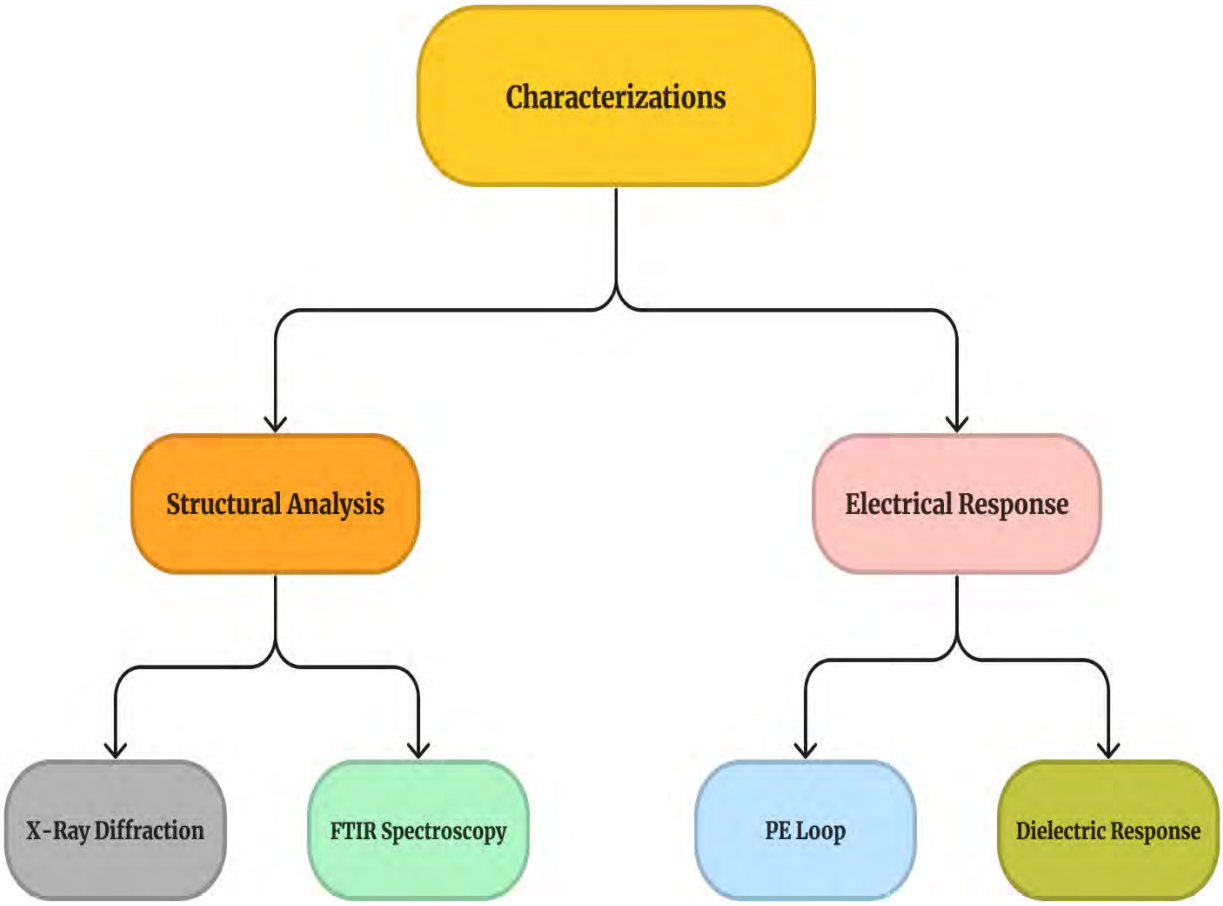

Figure 2.1 An overview of all characterization techniques.

2.1 Solvent Casting:

Solvent casting is the oldest technology used for flexible (plastic) films manufacturing. This technique was initially introduced over a hundred years ago to fulfill the demands of the emerging photographic industry. After 1950, new film techniques using thermoplastic polymers took over as the primary method for producing plastic films. This causes a decline in the significance of solvent cast technology. In recent times, interest in solvent cast technology has been grown up due to its ability to produce films of exceptionally high quality [57].

The sublingual film preparation utilizes the solvent casting method, Ih Is an old-age technique. In this process, the polymers are used as solute and are initially dissolved in a desired solvent. The drug and other additives are dissolved with a suitable solvent in a separate beaker. The two solutions are then mixed and stirred for some specific time. To eliminate the air bubbles, the solution undergoes sonication process. The solution is poured onto a Teflon or petri dish and left overnight or for some specific time to dry at a temperature of almost 50-60 °C. Then the prepared film is peeled off. The prepared film is kept in a desiccator [58]. Figure 2.2 illustrates the process of solvent casting.

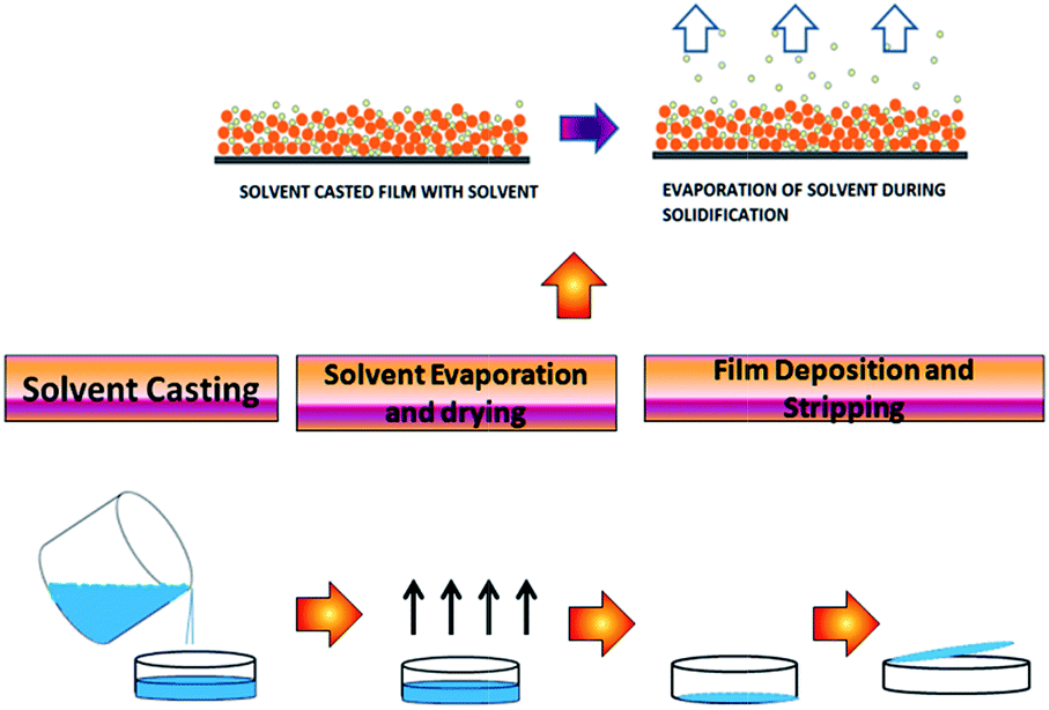

Figure 2.2 Technique of Solvent Casting [59]

Solvent casting is a technique widely used to fabricate thin, thick films and membranes. Film formation in this technique is done by casting the solution onto a substrate which results in the formation of thin/thick films. After casting the solution, allow the solution to evaporate under specific conditions. The solution will solidify after evaporating and formation of thin/thick film will take place. Different substrates can be used such as metal, glass or any other material depending on the application. Silicon can be used as flexible substrate. Advantages of solvent casting techniques includes [57].

- Thickness control
- Cost effectiveness

- Dimensional stability
- uniformity
- Excellent flatness

However, this technique also has a few disadvantages. The solvent volatility has a significant role in the film formation [60]. Less volatile solutions will take longer time to evaporate and will delay the drying of polymer film. Additionally, less volatile solvents tend to leave more residual solvent in the prepared film. For the recovery of solvent in this technique, high energy and high cost is required. Despite all disadvantages, solvent casting produces polymer films with superior properties as compared to those using other techniques.

2.2 X-Ray Diffraction (XRD):

In 1917, Albert Wallace Hull conduct the first in-situ diffraction experiment. Since then, diffraction techniques have developed and become a powerful tool for determining materials structure [61].

X-Ray diffraction (XRD) is a potent nondestructive technique used for the study of crystalline material. XRD provides information about material structure, phases, texture. Inter-planar spacing, average grain size and crystallinity can be calculated from XRD data. XRD is like a fingerprint of periodic atomic arrangements within a material. X-rays are ideal for materials structural study because the wavelength of X-rays and the distance between atoms in crystals are similar. So, the x-rays get diffracted by a crystal within a material [62].

2.2.1 Working principle of XRD:

Bragg's law is the fundamental principle behind the operation of X-ray diffractometers, expressed as,

$$n\lambda = 2dsin\theta \quad (2.1)$$

Where n is the order of reflection, λ is the wavelength of the incident X-rays, the interplanar spacing of the crystal is represented by d, and θ is the angle of incidence.

Bragg's law forms a relationship which links the angle of incidence (θ), interplanar spacing (d) and wavelength of incident ray (λ). Figure 2.3 shows two monochromatic X-ray beams A and A' are directed at a crystal at an angle of θ. The rays reflected from its atomic

planes and beam C' covers a greater distance than reflected beam C because it is reflected from a lower plane.

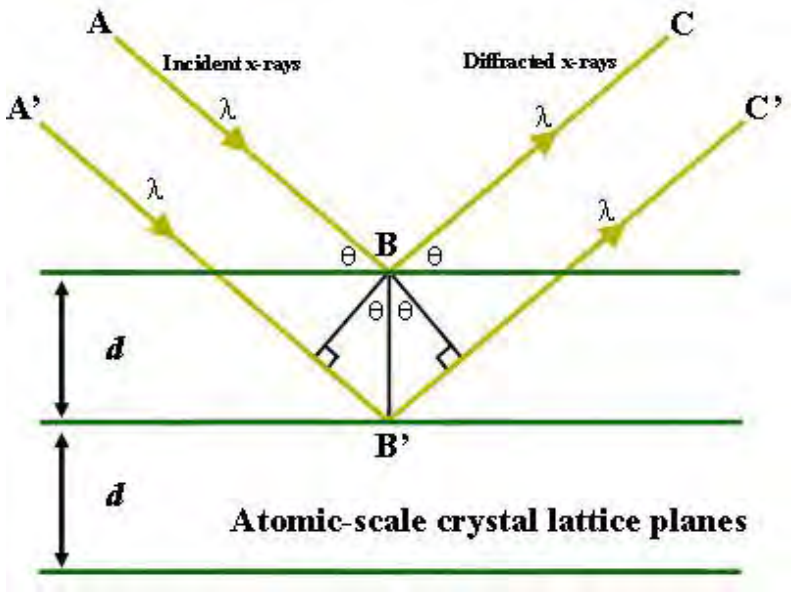

Figure 2.3 Bragg's Law reflection [63]

The interference between the two reflected beams can either be constructive or destructive, and it depends on the path difference between them. For constructive interference to occur, the difference in the path taken by the two reflected beams must be a whole number multiple of the wavelength. When constructive interference occurs, the X-ray beam diffracts from the crystal at an angle that matches the angle of incidence. The resultant XRD pattern consists of peaks of varying intensities at different angles. This spectrum is further compared to a reference database to study the material structure.

Using the Scherrer's formula from the diffraction peak and Bragg's law, the average size of the crystalline phase and interplanar spacing (d) can be measured.

$$< D > = \frac{K\lambda}{\beta cos\theta}$$

Where D is the crystalline phase average size, θ is the Bragg's angle, λ is the wavelength of the X-ray beam (λ = 1.53Å), K is the Scherrer's constant and its value for unknown crystallite size is 0.9, β is the Full Width Half Maxima (FWHM) of the diffraction peak. Maximum intensity peaks in the XRD pattern are typically used to determine the size of the crystallites [64].

The PANalytical Empyrean system was used to perform XRD scans In this study as shown in Figure 2.4. The system consists of an X-ray tube with a Copper (Cu) source, an X-ray detector, a sample holder, and a PC. The Cu source emits X-rays of characteristic wavelengths $K_{\alpha 1}$ ~1.540593 Å, $K_{\alpha 2}$ ~1.54442 Å and K_{β} ~1.54187 Å. This system operates at 45 kV and 40 mA. XRD data was collected in the range of 10° to 60° with a 0.01° step size using the Bragg-Brentano geometry for analysis.

Figure 2.4 PANalytical Empyrean System

2.3 Fourier Transform Infrared Spectroscopy (FTIR):

This technique uses infrared radiation (*IR*) beam to recognize the functional groups of different materials. This technique generates a spectrum that shows transmittance (%) versus wave number. To detect the functional groups, molecules must be *IR* active and have a dipole moment. The *IR* collaborates with the covalent bonds of material, causing the molecule to absorb energy and vibrate in a back-and-forth oscillation [65]. Due to bending, stretching and contraction of bond length vibrations of molecules occurs. Due to these vibrations change in

net dipole moment of a molecule occurs and leads to the absorption of *IR*. The energy of these vibrations is comparable to the quantum mechanical system of these molecules. So, the energy of these vibrations can be determined by using a simple harmonic oscillator (SHO) as in equation 2.2.

$$E_n = (n + \frac{1}{2})\hbar\omega_0 \qquad 2.2$$

Where ω_0 is the frequency of simple harmonic oscillator, $\hbar = 1.054 \times 10^{-34}$ Js and n can be chosen according to energy level. For, $n = 0$ equation 2.2 becomes,

$$E_0 = (\frac{1}{2})\hbar\omega_0 \qquad 2.3$$

Equation 2.3 shows that even in the ground state, vibration of molecules occurs. Fourier transforms infrared spectrometer can be used to measure these vibrations. Nicolet 5700 FTIR Spectrometer is used to measure these vibrations as shown in Figure 2.5.

Figure 2.5 Nicolet 5700 FTIR Spectrometer [66]

Molecules that are symmetrical or consist of a single atom do not absorb *IR*. Every bond has a unique vibrational frequency, only specific frequencies of infrared radiation will be absorbed.

2.3.1 Michelson interferometer:

The main component of FTIR is a Michelson interferometer as illustrated in Figure 2.6, that separates *IR* into its many components of wavelength. The Michelson interferometer is composed of three primary components: a moving mirror, a fixed mirror, and a beam splitter. Beam splitter is a semi-transparent device. The other both mirrors are perpendicular to one another [67].

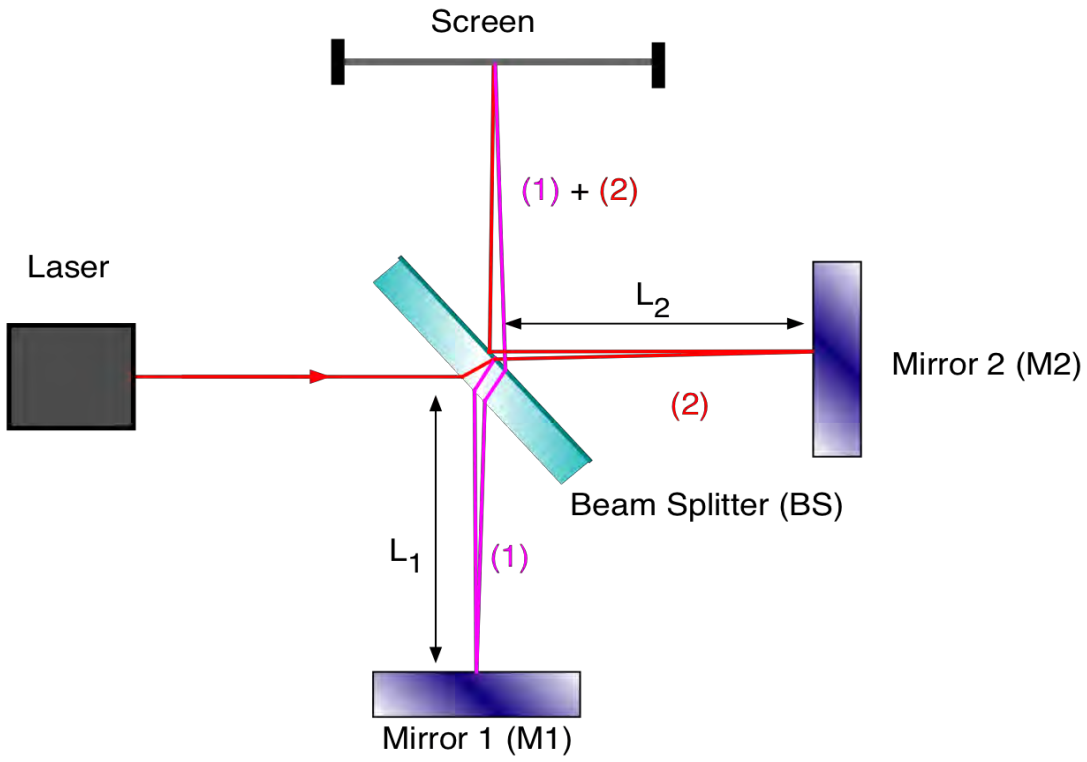

Figure 2.6 Michelson interferometer [68]

The beam splitter reflects the remaining part of the incident *IR* beam while transmitting some part of it. The transmitted part strikes on the fixed mirror while the reflected portion hits the moving mirror. Again, reflected by both mirrors, these incident beams are transmitted in the direction of the beam splitter. Both the beams are combined at the splitter. The detector collected the beam for the analysis of the sample after interference. Since the vibrations lie in the *IR* region, *IR* radiation is used to detect them. The Fourier Transform converts each absorption value into a single frequency value [69].

The background spectrum of KBr (potassium bromide) is collected first in thin pallets. After combining this small sample amount with KBr, the resulting blend is pelletized at a pressure of 4 tons/cm^2. The prepared pellet is placed in the spectrometer sample holder.

The wavelength ranges from 400 to 1500 cm^{-1}. On the computer monitor, we can observe the vibration modes for prepared samples. The obtained spectra were studied using "Omnic" software [70].

2.4 Electrical Measurement:

To conduct dielectric and $P-E$ loop measurements, silver (Ag) electrodes were deposited onto the prepared films using a sputter coater. The electrodes were circular in shape and coated on both sides of the film. Film was placed in a mask having circular holes of some specific diameter. This resulted in the formation of a capacitor. The capacitor was then used to study the electrical properties of a material.

2.4.1 Sputtering:

Sputtering involves the removal of particles from the surface of a solid material when ions are bombarded onto it. In this technique, the target material is deposited onto the material in its vapor phase [71].

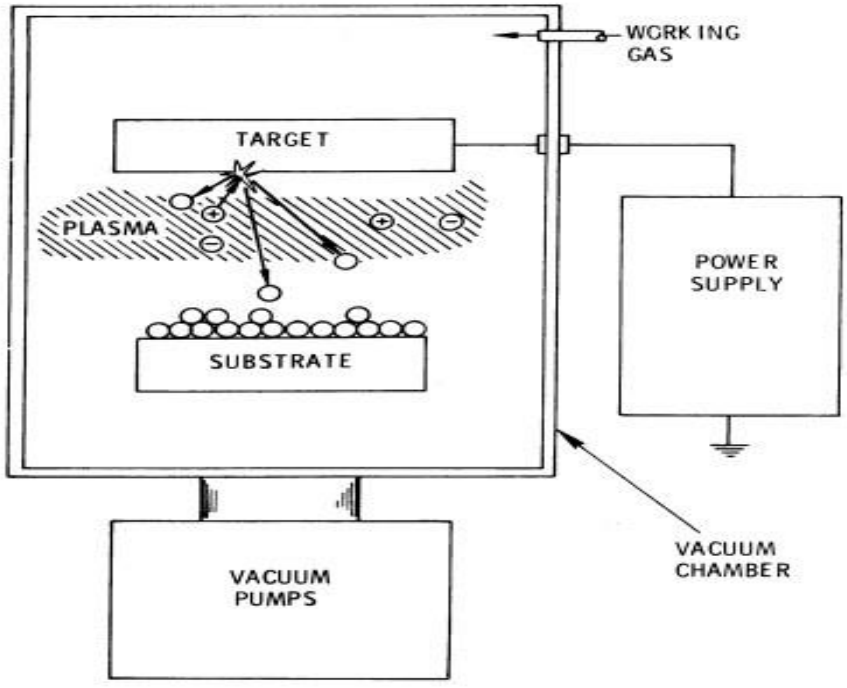

Figure 2.7 Basic components of a sputter coater [72]

The sputtering process involves a target material that is to be deposited onto a substrate or film placed below it. Particles in the air can resist the sputtering process, so a vacuum is created inside the chamber by using a vacuum pump. Once the chamber is

evacuated, it is backfilled with an argon gas. Potential is applied to generate plasma, due to which electrons are knocked out of the argon atoms and ionizing the gas into positively charged ions. These ions are then attracted towards the negatively charged target material and they collide with enough energy to dislodge particles from the target surface. The dislodged particles then fall towards the film which results in growth of electrodes on the film [72]. Figure 2.7 illustrates the basic components of a sputter coater.

GSL-1100X-SPC-12 Compact Plasma Sputter Coater in Figure 2.8 is used in this work to deposit the electrodes. The coater comprises a vacuum chamber, a target, a needle valve, a time adjustment knob, and a display indicating the vacuum and current settings. It operates within a medium vacuum range of up to 10-3 mmHg, and the sputtering duration can be adjusted from 0 to 110 seconds. Silver (*Ag*) was used as a target metal. During all the measurements deposition rate was kept 1 minute. 7 layers of electrodes were grown on each sample with a time gap of 10 minutes after each layer. The gas flow can be controlled using the needle valve, the corresponding settings for gas flow and current are displayed on the screen.

Figure 2.8 GSL-1100X-SPC-12 Plasma Sputter Coater and Vacuum Pump

2.5 Measurement of Dielectric Properties:

In this study, the LCR Meter is utilized to determine the dielectric constant of the samples at varying frequencies as a function of temperature. The Wayne Kerr LCR meter is

employed to measure the capacitance and dissipation of the samples across a frequency range from 1 kHz-1 MHz. The temperature controller displays the change in temperature. The range of temperature for the measurements is between 90 to 460 K. The data is recorded and displayed on a computer system connected to the LCR meter. The sample holder in the Cryostat Advanced Research System LN400 is coupled to a temperature controller. This system operates under vacuum conditions with a special LabView program. Figure 2.9 depicts the setup used for dielectric measurements.

Figure 2.9 High temperature dielectric setup

2.5.1 LCR meter:

An LCR meter is an electrical instrument used for measuring the capacitance, inductance, and resistance of circuits at various frequencies. Due to this property LCR meter name is given to this apparatus. Additionally, LCR meter provides information about quality factor, current, voltage, dissipation factor, phase angle, and equivalent series resistance [73]. It also evaluates the admittance components of susceptance and conductance. Moreover, the LCR meter can also measure the impedance of the circuit. This measurement involves applying a sinusoidal waveform at a specific frequency, then measuring the resulting sinusoidal current

and phase difference between the current and applied voltage impedance. Other electrical properties can be calculated using the impedance components.

2.5.2 Temperature Controller:

The Lakshore model 336 was used to measure and regulate the temperature of the heater. The model is equipped with two input sensors and two output heaters, offering a maximum output power of 50W and 100W. A type E thermocouple was used as input sensor, while a resistance temperature detector (RTD) with a platinum 100-ohm (Pt-102) sensor capable of measuring temperatures ranging from 14-873 K was connected for measurement and control of the sample temperature. A closed-loop temperature control system operating in proportional-integral-derivative (PID) mode was utilized to regulate the output power of the heater [74].

2.5.3 Dielectric Constant:

Dielectric constant can be defined as " the ratio of the material permittivity ($\mathcal{E}_m$) to the permittivity of free space ($\mathcal{E}_o$) ". Mathematically it is represented as,

$$\mathcal{E}_r = \frac{\mathcal{E}_m}{\mathcal{E}_o} \quad 2.4$$

The parallel plate capacitor setup comprises two conducting plates of area A and separated by a distance d as illustrated in Figure 2.10. The prepared material acts as a dielectric and is positioned between the plates, while the silver electrodes act as the two conducting plates. Upon the application of voltage to the parallel plates, they distribute electric charge and the potential difference between them is directly proportional to the quantity of charge stored on the plates.

$$Q \; \alpha \; V \quad 2.5$$

$$Q = CV \quad 2.6$$

Where capacitance is denoted by C and it is a fixed value that represents the capacity of a capacitor to accumulate electric charge while being subjected to an applied electric field. V refers to potential differences between plates. Figure 2.10 represents a parallel plate capacitor geometry.

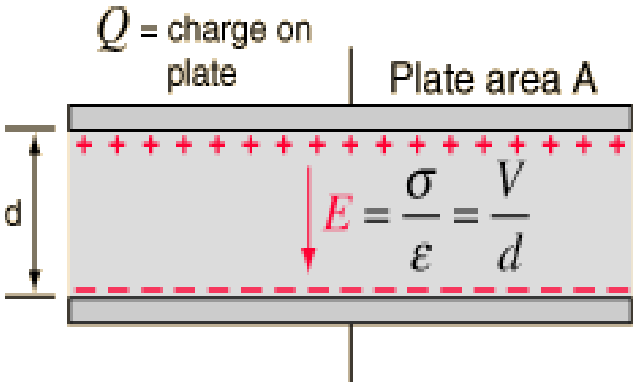

Figure 2.10 Parallel plate capacitor geometry [75]

The electric field strength, represented by E, that exists between the two plates of a capacitor can be determined through Gauss's law. The equation for E is as follows.

$$E = \frac{\sigma}{\varepsilon_o} \tag{2.7}$$

$$V = Ed = \left(\frac{\sigma}{\varepsilon_o}\right) d \tag{2.8}$$

$$V = \frac{qd}{\varepsilon_o A} \tag{2.9}$$

From Equation 2.6

$$C = \frac{Q}{V} = \frac{\varepsilon_o A}{d} \tag{2.10}$$

The insertion of a dielectric material between the plates of a capacitor leads to an increase in its capacitance, which is shown by equation 2.13.

$$C' = \varepsilon C = \varepsilon \frac{\varepsilon_o A}{d} \tag{2.11}$$

When a dielectric material is introduced between the plates of a capacitor and a DC voltage is applied, the capacitor can store more charge than if there was no dielectric material present. This is due to the inverse relationship between capacitance and the electric field produced across the plates of the capacitor, and the fact that the presence of the dielectric material reduces the effective electric field. The capacitance value in this case can be expressed as a function of the dielectric permittivity, which is related to the free space permittivity.

$$C_{med} = \frac{\mathcal{E}_r \mathcal{E}_o A}{d} \quad 2.12$$

$$C_{med} = \mathcal{E}_r C \quad 2.13$$

Dielectric constant has both real and imaginary components and is given as

$$\mathcal{E}_r = \mathcal{E}^{'} + i\mathcal{E}^{''} \quad 2.14$$

The real component of the dielectric permittivity is denoted by $\mathcal{E}^{'}$ and is associated with the amount of energy stored, while the imaginary component is denoted by $\mathcal{E}^{''}$, and is associated with the amount of energy lost.

2.6 Polarization vs Electric Field ($P - E$) loop measurement:

The plots of $P - E$ loops illustrate how the material polarization alters in response to an applied electric field. The deviation in the electric polarization value from the applied electric field is referred to as the hysteresis loop.

2.6.1 Sawyer Tower circuit:

In the 1930s, Sawyer and Tower conducted the initial measurement of hysteresis loops [76]. The ferroelectric system presented below in Figure 2.11 is utilized to determine the $P - E$ hysteresis loops of ferroelectric materials.

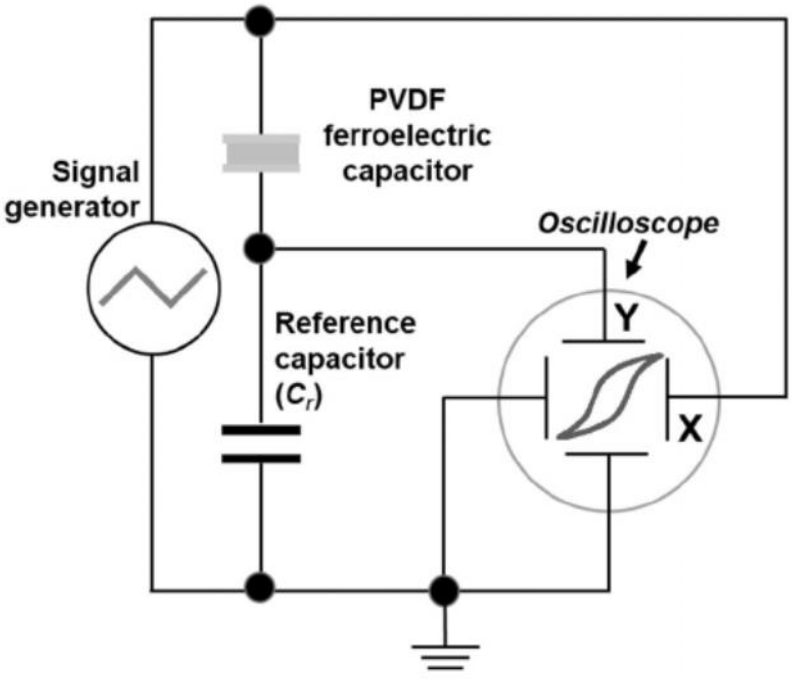

Figure 2.11 Sawyer-Tower circuit for ferroelectric hysteresis ($P - E$) measurement [77]

To measure the $P-E$ properties of a material, a circuit is employed, which includes two capacitors connected in series a reference capacitor C_r and a sample capacitor C_x. A resistive divider is employed to change the applied electric field across the sample capacitor. Value of C_r capacitance is known and is independent of voltage applied. AC signal of required waveform and frequency is applied on C_x. The current is integrated into charge by the reference capacitor. When a voltage is applied to the two inputs (X and Y) of an oscilloscope, a $P-E$ loop is produced**.**

The PolyK Polarization Loop and Dielectric Breakdown Test System depicted in Figure 2.12 were utilized to conduct $P-E$ measurements in this study. For measurement of bulk samples, the system is connected to a trek amplifier which provides voltage up to 10 kV. While in the case of thin samples the setup is not connected to trek amplifier and only provides voltage up to 200 V [78, 79]. Users can control voltage, waveform and frequency using LabView program installed on PC. Additionally, it can also measure charge less than 1nC.

Figure 2.12 PolyK Polarization loop and Dielectric Breakdown Test System

Chapter 3 Synthesis and Structural Characterizations

This chapter covers the synthesis and fabrication of PVDF, P(VDF-TrFE) and Indium Tin Oxide (ITO) Etched PVDF thick film along with its structural characterizations. For the synthesis of P(VDF-TrFE) 70/30 and PVDF thick films, solvent casting method is used. The ITO etched PVDF is obtained after ITO is removed from PVDF/ITO which is commercially available.

3.1 Synthesis of PVDF thick film:

3.1.1 Solution preparation of 10wt% PVDF:

In this procedure, a 10wt% solution of PVDF was prepared by mixing PVDF grains with calculated amount of DMF. Stoichiometric amount of DMF was added to glass bottle and heated for 5 minutes just to warm up the DMF. Then calculated amount of PVDF grains was added to that glass bottle. For a homogeneous solution, bottle was stirred for 2 hours at 60 °C. Figure 3.1 covers the whole process of solution preparation.

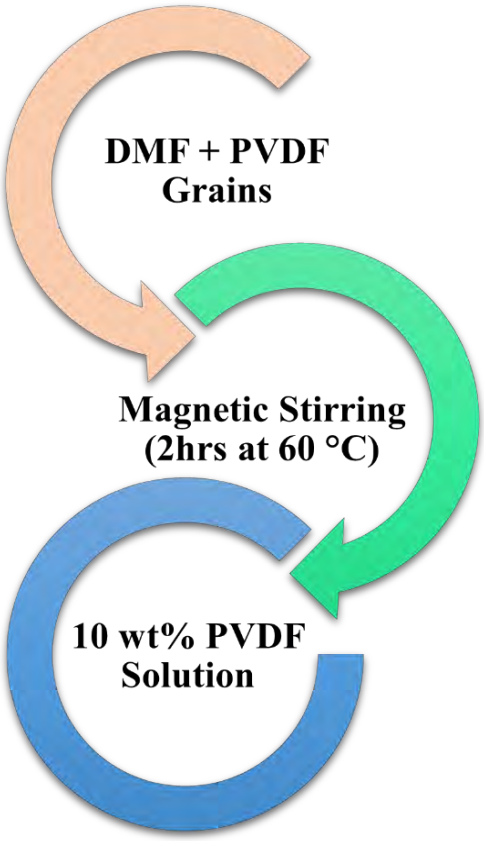

Figure 3.1 Solution preparation process

3.1.2 Preparation of PVDF thick film:

After 2 hours of magnetic stirring at 60 °C, uniform solution of 10 wt% PVDF was prepared.

- The calculated amount of prepared solution was poured in the glass cavity.
- The dimensions of cavity calculated were approximately equals to 2.01 inches in length, 1.97 inches of width and 1mm of height, which was equal to 0.0394 inches. The calculated volume for this glass cavity is 2.55 mL.
- The glass cavity filled with solution was put in oven for annealing. The cavity was annealed for 3 hours at 60 °C.
- After the process of annealing, a 27 µm thick film of PVDF was ready to peel off from the cavity. Area of prepared film was approximately 25.5 cm^2.
- The process for the preparation of PVDF thick film is shown in Figure 3.2.

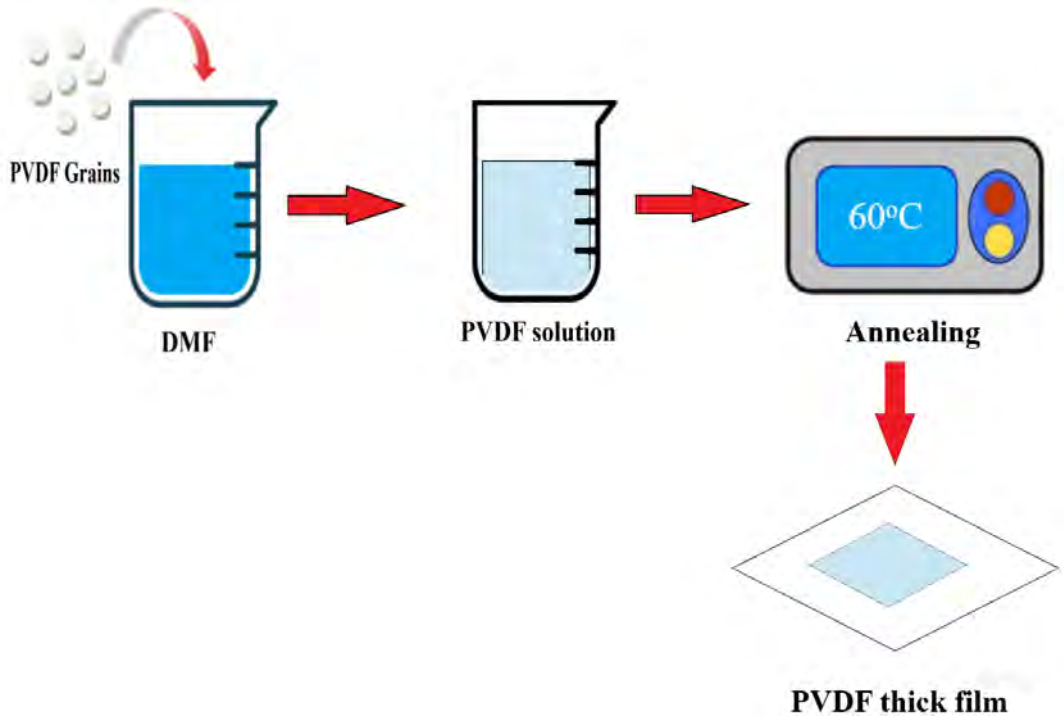

Figure 3.2 Preparation of PVDF thick film.

3.2 Synthesis of P(VDF-TrFE) thick film:

3.2.1 Solution Preparation of 6wt% P(VDF-TrFE):

In this process, the measured amount of P(VDF-TrFE) was dissolved in N, N-Dimethylformamide (DMF) to prepare a 6wt% solution of P(VDF-TrFE). Measured amount of DMF was poured in a glass bottle and stirred on a magnetic stirrer for 5 minutes just to

warm up. Used P(VDF-TrFE) 70/30 was purchased from USA (PolyK) and is available in powder form as shown in Figure 3.3. Stoichiometric amount of P(VDF-TrFE) was added to glass bottle already contain DMF in it and stirred for 1 hour at 70 °C to prepare a homogenous solution. The solution was further stirred for 24 hours at 50 °C to obtain proper chains alignments. Flow chart of the procedure used for the solution preparation of P(VDF-TrFE) is presented in Figure 3.4.

Figure 3.3 100-gram Resin of P(VDF-TrFE) 70/30 mol Copolymer [80]

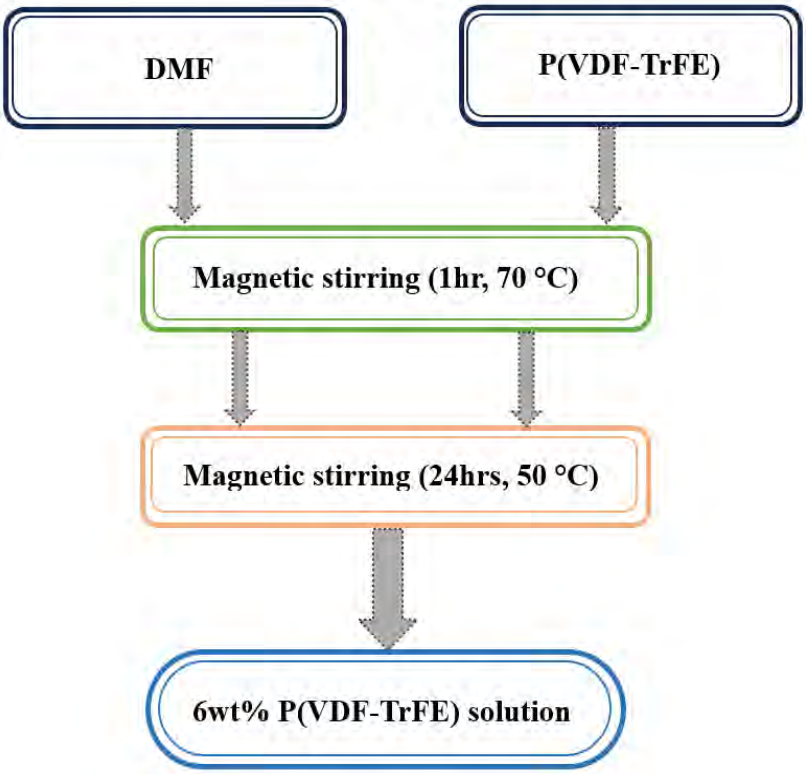

Figure 3.4 Flow chart of the procedure used for the preparation of P(VDF-TrFE) solution.

3.2.2 Preparation of P(VDF-TrFE) thick film:

After 24 hours of magnetic stirring, uniform solution of 6wt% P(VDF-TrFE) was obtained.

- The calculated amount of solution was poured into a self-made glass cavity using a glass syringe.
- The calculated dimensions of cavity were approximately equal to 2.89 inches of length, 1.04 inches width and 0.19 inches of height. The volume calculated for this cavity is 9.36 mL.
- For annealing, a filled glass cavity was placed in oven for 3 hours at 130 °C.
- After annealing, a 28 µm thick film with area approximately equals to 19.3 cm^2 was obtained and ready to peel off from the cavity. The process of peeling off is shown in Figure 3.5.
- The thickness of prepared films depends on the quantity of solution poured into the glass cavity.

❖ The process for the preparation of P(VDF-TrFE) thick films is illustrated in Figure 3.6.

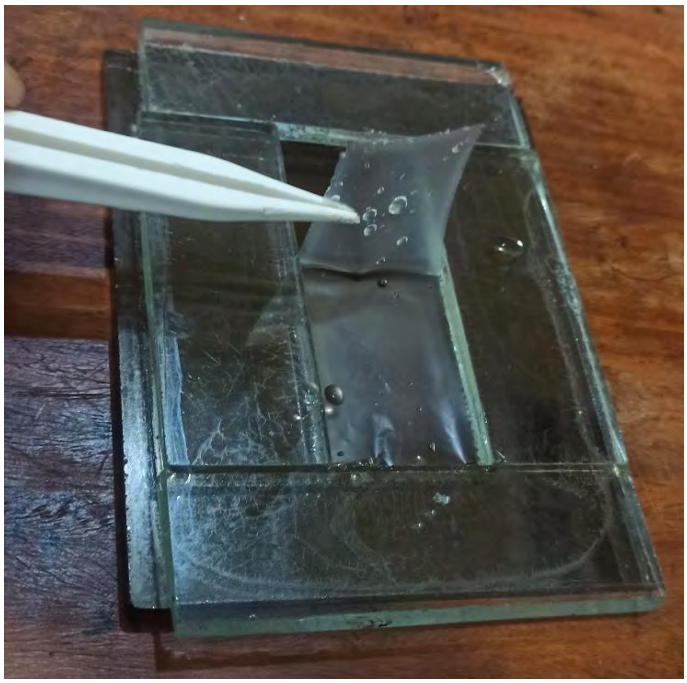

Figure 3.5 28 µm thick film of P(VDF-TrFE) 70/30

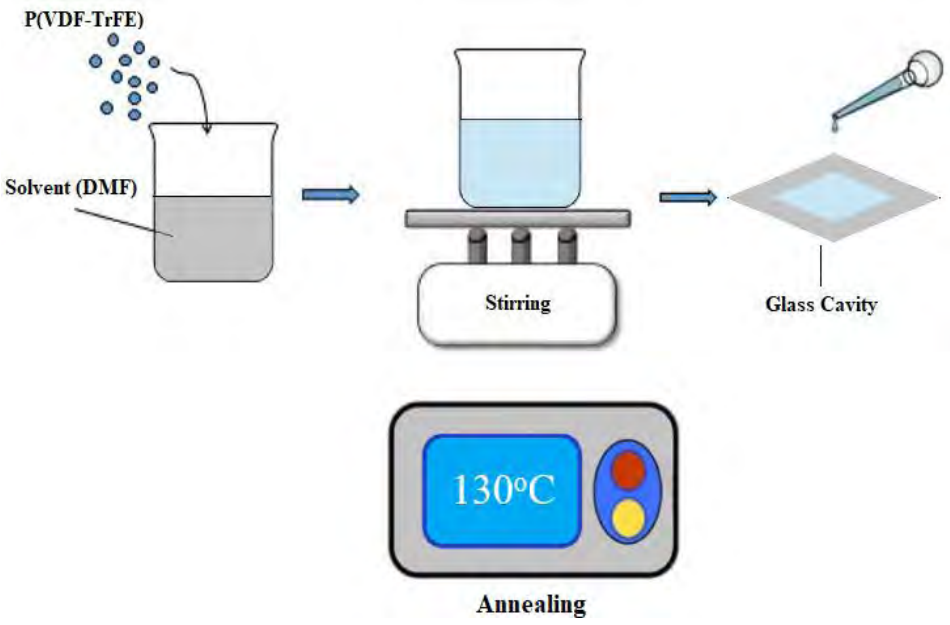

Figure 3.6 Fabrication of P(VDF-TrFE) 70/30 thick films

3.3 Beta PVDF:

A beta PVDF/ITO sheet of thickness 28 μm was purchased from PolyK (USA). β-phase of PVDF is already discussed in chapter 1 section 1.11.2. β-phase can be achieved by mechanical stretching, straining, quenching [81] or applying electric field [82]. The sheet is optically transparent with grown ITO electrodes on both sides. The resistance on both surfaces is 300 ohms /square. The β-sheet is uniaxially oriented with high d_{31} which is 29-31 pC/N and d_{33} is around 23-28 pC/N. Modulus of sheet is around 2.3 GPa. The piezoelectric response of the sheet is exceptionally great, hence it is used in piezo energy harvesting, microphones, loudspeakers, transparent flexible piezo sensors, robotics, actuators [83].

3.3.1 Wet Etching of ITO:

Wet etching was done to remove the layer of ITO from PVDF/ITO sheet. The etching process was done to grow silver electrodes through plasma sputter coater to analyze its difference in various physical properties. Etching of ITO was done through dilute Hydrochloric acid (HCl). Dilute HCl was prepared by adding 1ml of HCl to 10ml of deionize water in a beaker. The required sheet was dipped for 3 minutes in the beaker filled with dilute HCl. After 3 minutes of dipping, the sheet was then taken out of the dilute HCl. The sheet was further dipped in deionized water for 1 minute, this step was done for cleaning purposes. Digital multimeter was used to check the conductivity of the sheet. The sheet shows no sign of conductivity which indicates that ITO was completely removed from the surface of PVDF. Figure 3.7 illustrates the process of wet etching.

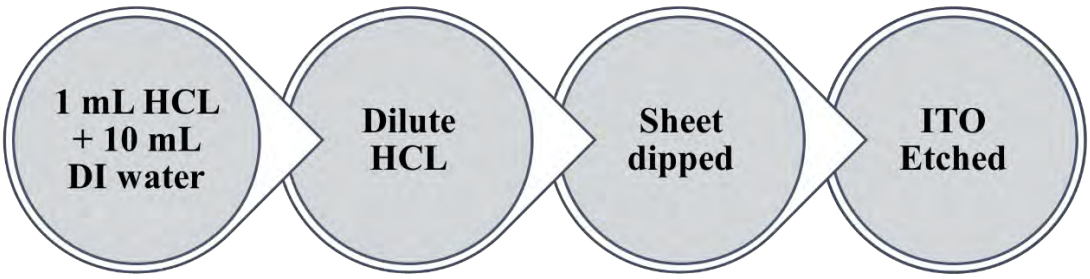

Figure 3.7 Etching process.

3.4 Fabrication of Electrodes:

For electrical characterizations such as ferroelectric loop and dielectric measurements, electrodes were grown on the films of solvent cast PVDF, ITO etched PVDF and P(VDF-TrFE). For this purpose, two metal masks were used. The diameter and area of both the

masks were different from each other. Figure 3.8 (a) represents the upper metal mask. The diameter of the upper metal mask is 3.048 mm, and the area is 0.07065 cm^2. Figure 3.8 (b) represents a lower metal mask; its diameter and area are 2.032 mm and 0.0314 cm^2. The samples were sandwiched in between the two-metal mask. Silver (Ag) electrodes were grown on the films using a plasma sputter coater.

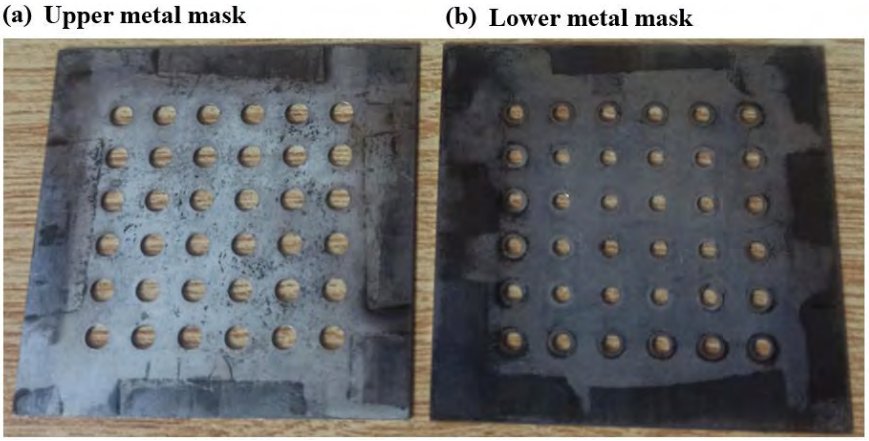

Figure 3.8 (a) upper metal mask (b) lower metal mask

3.5 X-Ray Diffraction:

X-Ray diffraction (XRD) was used for the structural analysis of all the specimens. For XRD PANalytical Empyrean system was used and scan was taken within the range of 2θ = 10° to 60° with angle increment equals to 0.01° and step time of 1 second. XRD patterns were observed at room temperature and presented in Figure 3.9.

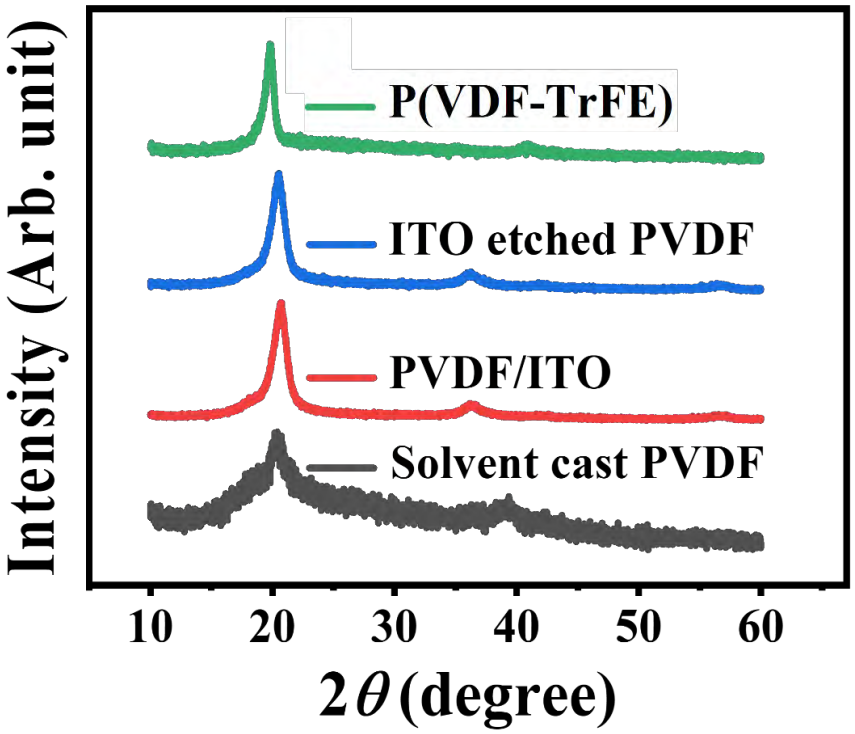

Figure 3.9 XRD spectrum of solvent cast PVDF, PVDF/ITO, ITO Etched PVDF and P(VDF-TrFE)

XRD analysis of solvent cast PVDF indicates the presence of two peaks at 2θ = 20.3° and 39°. A broader hump was also observed at 2θ =18.4°. In PVDF/ITO sample, peaks were observed at 2θ = 20.7°, 36.4° and 56.9° with small evidence of hump was observed along with the highest intensity peak, while peaks of ITO etched PVDF were observed at 2θ = 20.4°, 36.3° and 56.6°. Along with the highest intensity peak, a small hump was observed in PVDF/ITO and ITO etched PVDF. In P(VDF-TrFE) two peaks were observed at 2θ = 19.8° and 41°. Table 3.1 presents the details about phases associated with their angles for all samples.

Solvent Cast PVDF		PVDF/ITO		ITO Etched PVDF		P(VDF-TrFE)	
2θ	Phase	2θ	Phase	2θ	Phase	2θ	Phase
18.4°	α	20.7°	β	20.4°	β	19.8°	β
20.3°	β	36.4°	β	36.3°	β	41°	β
39°	α	56.9°	β	56.6°	β	-	-

Table 3.1 Phases at different angles for all the samples

A broad peak is observed in the XRD spectrum of solvent cast PVDF, which confirms the presence of more than one phase. Peaks observed at $2\theta = 20.3°$, $20.7°$ and $20.4°$ in solvent cast PVDF, PVDF/ITO and ITO etched PVDF respectively, corresponds to β-phase, and attributed to (110), (200) planes. Small humps located at $2\theta = 18.4°$ and $39°$ indicates the presence of α-phase in solvent cast PVDF sample and corresponds to (020) and (002) planes respectively. Peaks observed at $2\theta = 36.4°$ and $56.9°$ in PVDF/ITO is associated with β-phase and attributed to (101) and (020) planes respectively. Peaks at $2\theta = 36.3°$ and $56.6°$ in ITO etched PVDF also correspond to β-phase [84-90]. In the XRD spectra of P(VDF-TrFE), one sharp peak at $2\theta = 19.8°$ and minor hump at $2\theta = 41°$ observed in XRD spectra is associated with β-phase. The peak at $2\theta = 19.8°$ corresponds to the superposition of reflection from (110) and (200). It corresponds to high degree of crystallinity in β-phase. The minor hump at $2\theta = 41°$ shows reflection from (201) lattice planes [91-95].

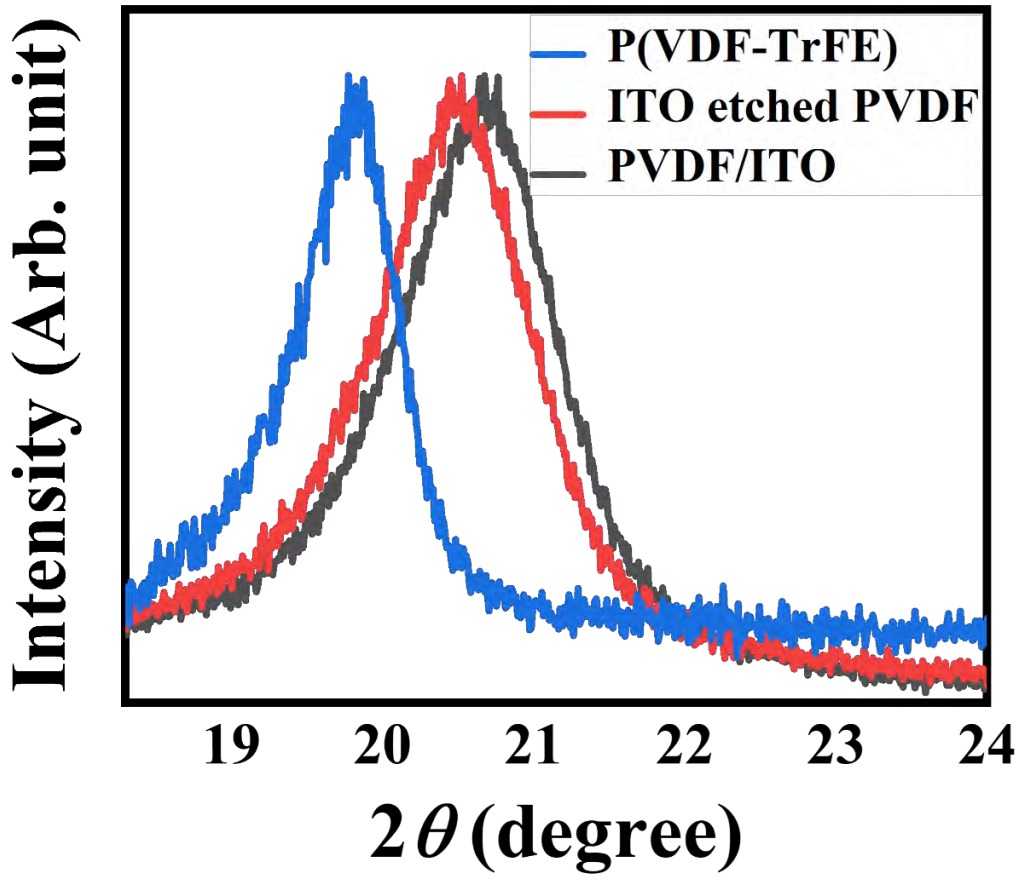

Figure 3.10 Peak shift in XRD spectrum of ITO etched PVDF and P(VDF-TrFE)

XRD spectrum of PVDF/ITO, ITO etched PVDF and P(VDF-TrFE) are combinedly plotted between the angle $2\theta = 18°$ to $24°$ to clearly observe the shift in the highest intensity

peak as shown in Figure 3.10. A prominent shift in the peaks corresponds to the β-phase are observed in ITO etched PVDF and P(VDF-TrFE) sample as compared to PVDF/ITO sample peak. ITO grown on the surface of PVDF exerts strain on the PVDF. When ITO is etched from PVDF, it results in uniform expansion due to which interplanar spacing (d) increases. Increase in d-spacing results an increase in lattice parameters [96]. According to Bragg's law relation $n\lambda = 2dsin\theta$ increase in d cause shift in peak towards lower angle. From Figure 3.10 it is observed that Peak of P(VDF-TrFE) shifts towards lower as compared to PVDF/ITO, ITO etched PVDF. Polymer chains of P(VDF-TrFE) are less densely packed in the crystal cell than that of PVDF/ITO and ITO etched PVDF [97] which cause an increase in d-spacing and results in shifting of peak towards lower angle. Table 3.2 shows d-spacing calculated for all the prepared samples using Bragg's law.

PVDF is made up of CH_2 and CF_2 chains, while TrFE is made up of CHF and CF_2 chains. TrFE content in P(VDF-TrFE) is responsible for transforming the chain conformation into all trans (TTTT) configuration, which may be correspond to difference in steric hindrance between CFH and CF_2 [97]. When TrFE content is added to PVDF, hydrogen (H) atom is replaced by fluorine (F) atom. Addition of TrFE favor trans (T) bond instead of gauche (G) bond. The larger size and high electronegativity of fluorine atom changes its lattice parameters due to which diffraction angle changes and shift in peak is observed.

Solvent Cast PVDF		PVDF/ITO		ITO Etched PVDF		P(VDF-TrFE)	
2θ	d (Å)	2θ	d (Å)	2θ	d (Å)	2θ	d (Å)
18.4°	4.81	20.7°	4.27	20.4°	4.33	19.8°	4.47
20.3°	4.36	36.4°	2.46	36.3°	2.46	41°	2.20
39°	2.30	56.9°	1.60	56.6°	1.62	-	-

Table 3.2 Interplanar spacing (d) of solvent cast PVDF, PVDF/ITO, ITO Etched PVDF and P(VDF-TrFE)

3.6 Fourier Transform Infrared Spectroscopy:

Fourier Transform Infrared Spectroscopy (FTIR) is used for the identification of different types of phases exist and detection of different bonds present in a crystal. The FTIR

pattern of all the prepared samples is presented in Figure 3.11. From FTIR pattern, presence of mixed phases (α, β and γ) are observed. The FTIR scan is performed within the range of 400-1500 cm^{-1} for solvent cast PVDF, PVDF/ITO, ITO Etched PVDF and P(VDF-TrFE).

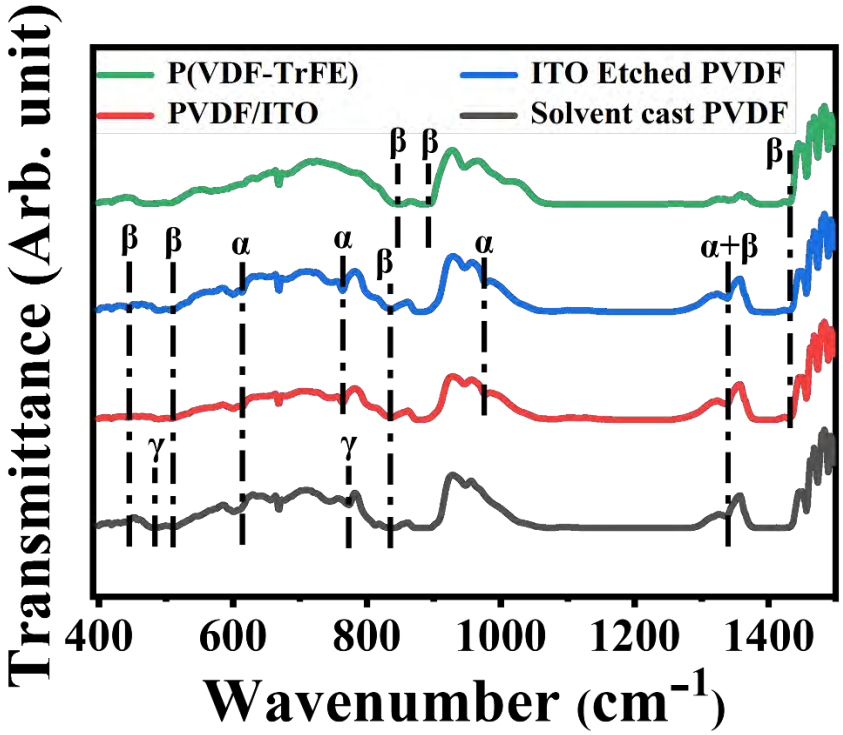

Figure 3.11 FTIR spectra of solvent cast PVDF, PVDF/ITO, ITO Etched PVDF and P(VDF-TrFE)

In FTIR spectrum of the Solvent cast PVDF, PVDF/ITO and ITO etched PVDF these different vibrational bands are observed which are located at 443, 510, 482, 612, 764, 775, 834, 975, 1337 cm^{-1} The band at 443, 510, and 834 cm^{-1} corresponds to polar β-phase in all the three samples, in which 510 cm^{-1} is attributed to the bending of CF_2 bond [98, 99]. The band at 482 and 775 cm^{-1} indicates γ-phase in solvent cast PVDF [99, 100], while no vibrational band corresponding to γ-phase is observed in PVDF/ITO and ITO etched PVDF sample Dips associated with α-phase are observed at 612, 764, 975 cm^{-1} in all the three samples. The vibrational band at 612 cm^{-1} is present in all the three samples and corresponds to C-C-C skeletal vibration and bending of CF_2. 764 and 975 cm^{-1} bands were observed in PVDF/ITO and ITO etched PVDF. Mode at 764 cm^{-1} corresponds to CH_2 skeletal bending [98, 99, 101, 102]. Dip at 1337 cm^{-1} is attributed to zeta (α+ β) phase in the three samples except P(VDF-TrFE) and corresponds to plane bending (twisting or wagging). Zeta phase is

the sum of α and β phase [103]. 1432 cm^{-1} band in PVDF/ITO and ITO etched PVDF corresponds to β-phase [100].

In P(VDF-TrFE), vibrational bands are observed at 844, 890, 1400 and 1432 cm^{-1}. All the mentioned bands correspond to polar β-phase. The vibrational band at 890 cm^{-1} corresponds to *a*-axis, dip at 848 cm^{-1} associated with *b*-axis and band at 1400 cm^{-1} indicate *c*-axis. Band at 844 cm^{-1} show CF_2 symmetric vibrations coupled with the symmetric stretching vibration of C-C. Bands located at 1400 and 1432 cm^{-1} were attributed to wagging vibration of CH_2 and CH_2 bending [104-106].

FTIR pattern confirms the presence of three phases (α, β and γ) in PVDF prepared by solvent casting technique, while PVDF/ITO and ITO etched PVDF confirms the presence of β-phase along with minor α-phase. This minor α-phase may correspond to small hump that was observed along with the highest intensity peak as reported in XRD of PVDF/ITO and ITO etched PVDF. FTIR spectra of ITO etched PVDF is same as that of PVDF/ITO. The only difference between their FTIR spectra is their bands intensity. When compared to PVDF/ITO, the intensity of the bands in ITO etched PVDF is higher, which may be due to the removal of conductive surface (ITO) through wet etching. After the removal of ITO, PVDF is more exposed to light, and it could lead to bands of higher intensities. P(VDF-TrFE) shows the presence of only crystalline β-phase, which is due to the addition of TrFE content. TrFE content increases crystallinity which results in β-phase which is much crystalline as compared to other phases.

Chapter 4 Results and Discussion

In this chapter, the electrical response of solvent cast PVDF, ITO etched PVDF and P(VDF-TrFE) thick films will be discussed briefly. For the study of electrical properties, silver (*Ag*) electrodes were sputtered on the prepared thick films of solvent cast PVDF, ITO etched PVDF and P(VDF-TrFE).

4.1 Dielectric Response of solvent cast PVDF, ITO etched PVDF and P(VDF-TrFE):

The dielectric response of solvent cast PVDF, ITO etched PVDF and P(VDF-TrFE) is measured at different frequencies (1 kHz-1 MHz) within the temperature range of 90-430 K. Figure 4.1 (a, b) presents the in-phase (ε') and out-of-phase (ε'') part of solvent cast PVDF sample while (c) and (d) corresponds to ε' and ε'' part of ITO etched PVDF.

It is observed from Figure 4.1 (a, b) that in-phase (ε') and out-of-phase (ε'') of dielectric constant as a function of temperature exhibits three different regions. The first region (80-200 K) demonstrates the independent region of temperature. In the first region all the dipoles remain frozen, and hence resulting in no noticeable change in the real and imaginary part. In the second region (200-350 K), a significant increase in ε' and a consistent peak in ε'' is observed. In the third region (above 350 K), a sharp rise is observed in both ε' and ε''.

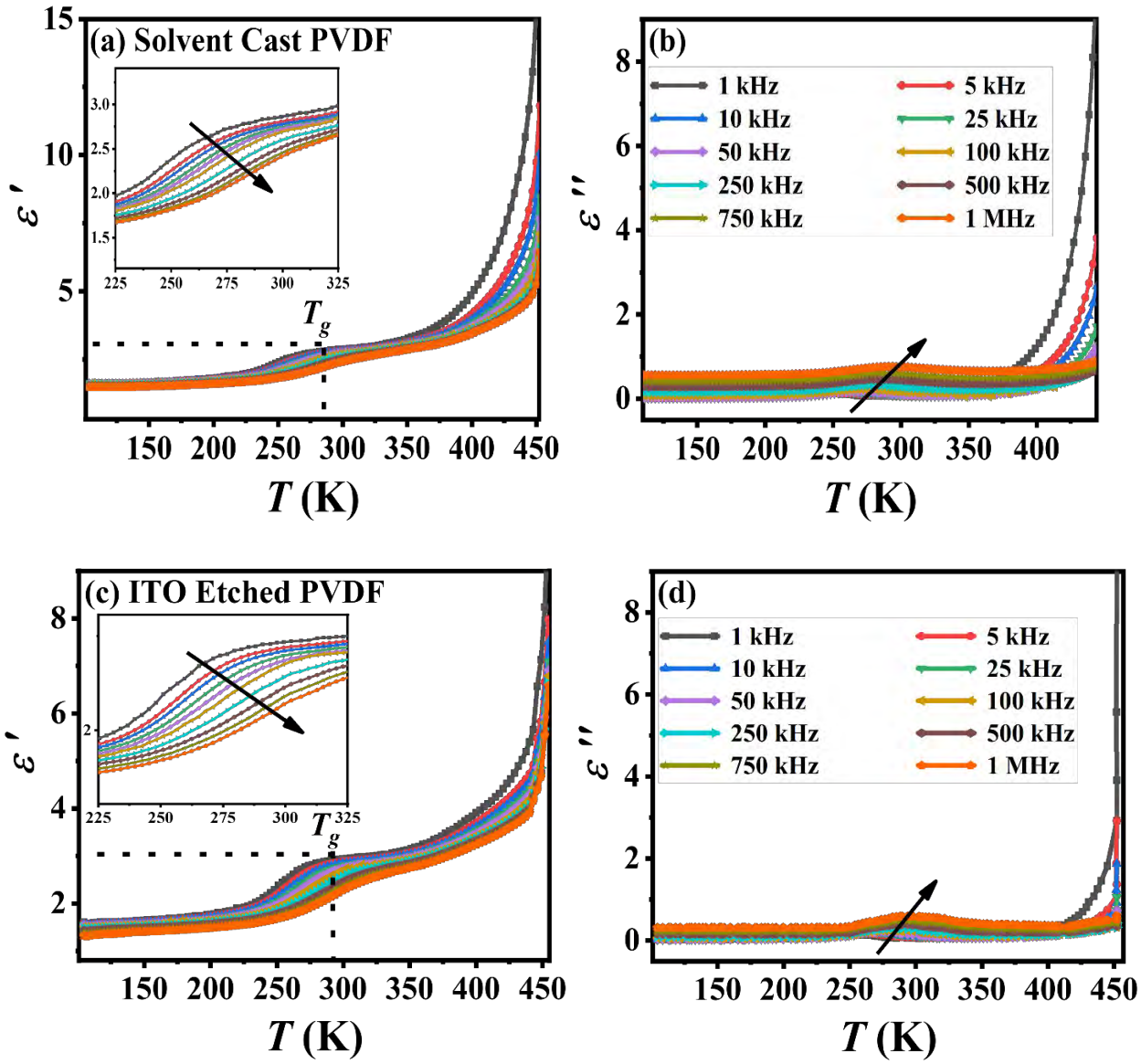

Figure 4.1 Dielectric spectra (a) ε' component of solvent cast and (b) ε'' component of solvent cast PVDF, (c) ε' part of ITO etched PVDF, (d) ε'' part of ITO etched PVDF (Arrow-Head points towards increasing frequency)

The first region (80-200 K) in both solvent cast PVDF and ITO etched PVDF is defined as the temperature independent region and both the ε' and ε'' remain constant as a function of temperature. This response arises because of segmental polarization of C-F bond. In low temperature regions, polar C-F bond does not vibrate and shows no mobility. In this region, dipoles become frozen and stiff. Also, polar materials such as PVDF exhibit non-polar behavior and did not respond to temperature change in the first region. This further supports the fact that 200 K can be identified as the critical temperature (T_c) for solvent cast PVDF and

ITO etched PVDF. Below T_c nature of PVDF convert from polar into a non-polar state [107, 108].

The second region (200-350 K) is known as a temperature dependent region. An increase is observed in this region for both ε' and ε'' parts. According to literature, the relaxation mechanism observed in PVDF between 200-325 K temperature are known as α_a-relaxation, β-relaxation, or dipolar-relaxation. This relaxation is associated with glass transition temperature (T_g). In this region, the polymer chains become softer. Near T_g, chain segments in amorphous regions gain sufficient activation energy and dipoles tend to align themselves parallel to the applied field. As a result, both ε' and ε'' components of dielectric permittivity increases. This response is common in both solvent cast PVDF and ITO etched PVDF [98, 107, 109, 110].

Above 350 K, a sharp rise is observed in both the ε' and ε'' components of dielectric permittivity. Mobility of polymer chains is not the cause of increasing dielectric constant with temperature in this region. At high temperature, the increase in ε' and ε'' is primarily attributed to interfacial polarization. Both amorphous and crystalline regions are present in PVDF, hence heterogeneous interfacial polarization is responsible for the rise of dielectric constant in this region. This rapid increase may also be attributed to the Maxwell-Wagner effect. This effect is efficacious at low frequencies and high temperature regions. At low frequencies, space charges get active, and the phenomenon of Maxwell-Wagner arises [107, 108]. The curie temperature (T_c) of PVDF is higher than its melting point (T_m).

Another observation is the frequency dependence of dielectric permittivity in the second and third region of Figure 4.1. At lower frequencies ε' and ε'' exhibit higher value and vice versa. After T_g, dipoles exhibit inertia, and they require enough time to respond to the field applied. At higher frequencies (less time), ε' and ε'' exhibit lower value. When electric field is applied at higher frequencies, dipoles of polymer chains don't have sufficient time to align themselves parallel to field applied. Also, the applied electric field changes rapidly. Contribution of distortion and deformation of material structures results in lower value of ε' and ε''. At lower frequencies (more time), ε' and ε'' exhibits larger value. After an external field is applied, polymer dipoles have enough time to align themselves parallel to applied field, thus resulting in increase of ε' and ε'' and dipoles will attain their maximum value. This behavior of dipoles at low frequencies is termed as low frequency dispersion (LFD) or Maxwell-Wagner effect [110] [111].

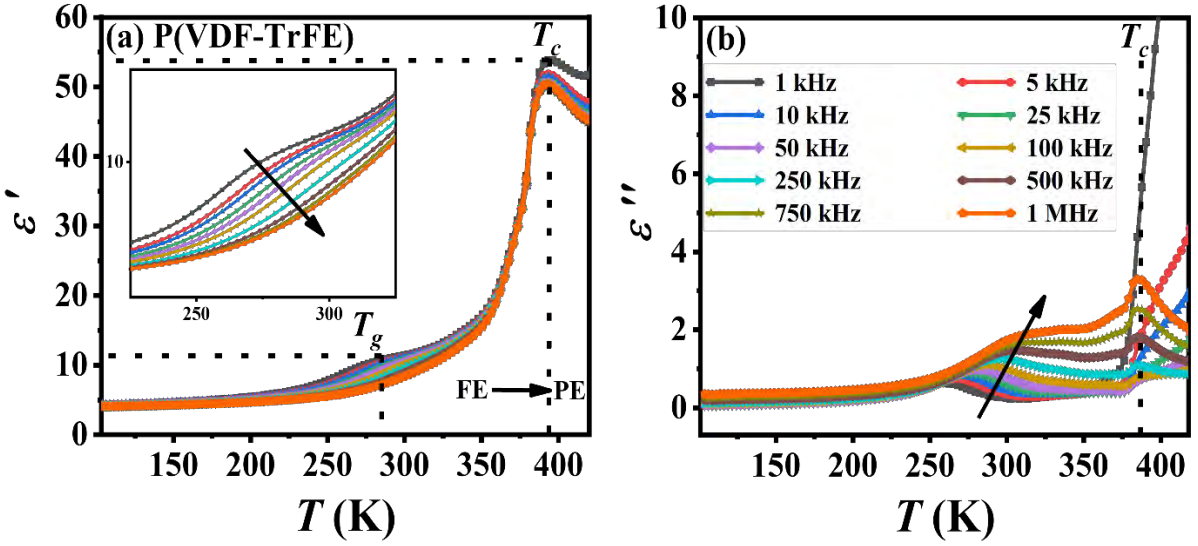

Figure 4.2 Dielectric spectra (a) real part, (b) imaginary part of P(VDF-TrFE)

The dielectric constant of P(VDF-TrFE) is also plotted as function of temperature and shown in Figure 4.2 in which (a) represents the real (ε') part and (b) depicts the imaginary (ε'') part of P(VDF-TrFE) dielectric permittivity. The overall pattern of the dielectric permittivity in P(VDF-TrFE) is same as that of solvent cast PVDF. The first two regions in which dielectric constant change as a function of temperature are similar to the regions observed in solvent cast PVDF and ITO etched PVDF sample. However, the third region is different.

The first region (90-200 K) is known as the temperature independent region. In this region, both ε' and ε'' show a constant behavior because dipoles have no mobility. The dipole gets frozen and becomes stiff. In this region, P(VDF-TrFE) exhibits non-polar nature [110].

In the second region (200-325 K), a slight increase is observed for both ε' and ε'' parts of dielectric permittivity, which corresponds to glass transition temperature (T_g). T_g is observed in the range of 245-300 K and is associated with the polymer chains relaxation [112]. In polymer chains of P(VDF-TrFE), fluorine atoms are positioned on one side and hydrogen atoms on the other side. The lattice packing of all-trans (TTTT) bonds in the polymer chain is responsible for the larger dipole moment in P(VDF-TrFE). Due to the dipole moment of these chains, ε' and ε'' components of dielectric constant increases [113].

In P(VDF-TrFE) sample, a prominent peak is observed in the third region (325-392 K) in both in-phase (ε') and out of phase part (ε''). This peak is defined as a transition peak and related with the transition of ferroelectric phase to paraelectric phase at curie temperature

(T_c = 392-399 K). At T_c, the all-trans (TTTT) chain conformation of P(VDF-TrFE) is replaced by TTTG configuration, where C-C bonds begin to rotate freely. The long chains sequence of highly polar P(VDF-TrFE) is divided into very short TTT segments with adequate polarity by TrFE in G or G'. Due to the alignment of these small chain segments under the influence of raised temperature and in the presence of a modest electric field may contribute significantly to polarity, which characterized the increase in ε' and ε'' components of dielectric permittivity at T_c [97].

The molar content of TrFE and the film processing parameters affect the value of T_c. Crystal size and interplanar distance (d) also affect the value of T_c. The energy barrier for the transition is reduced when the size of the lattice increases. Transition at T_c is induced by the mutual vibration of chains in ferro-electric domains. Small ferroelectric domains arise as the crystallite size decreases, thus resulting in lowering the energy barrier for the transition to occur [86, 114, 115].

After T_c, a decrease in dielectric constant is observed as a function of temperature. Above T_c dipoles get sufficient kinetic energy, which results in segmental rotation [113]. This increase in kinetic energy causes the disordering mobility of the ferroelectric domain which leads to a significant decrease in the real part and a rapid increase in the lossy component [97]. Dielectric loss (ε'') increases above T_c at low frequencies due to pre-melting points induced by impurity ions and conduction loss [97, 116].

The dielectric constant of solvent cast PVDF, ITO etched PVDF and P(VDF-TrFE) sample are plotted combinedly as a function of temperature at fixed frequency of 1 kHz as shown in Figure 4.3. From the graph it is observed that P(VDF-TrFE) exhibits a higher dielectric constant as compared to solvent cast PVDF and ITO etched PVDF. TrFE content affects the dielectric permittivity of the P(VDF-TrFE) copolymer. The large dielectric constant value of P(VDF-TrFE) is due to the high crystallinity and presence of ferroelectric β-phase. XRD spectra of P(VDF-TrFE) film also confirms the existence of dominant β-phase. Larger dipole moment in P(VDF-TrFE) chains is also responsible for the higher value of dielectric constant. [117, 118].

Larger value of dielectric permittivity in P(VDF-TrFE) is also related with the chain orientation [119]. Dipole moment and bond length in P(VDF-TrFE) is greater than that of solvent cast PVDF and ITO etched PVDF, which may also be attributed to high dielectric

constant [120]. At low frequency (1 kHz), dielectric loss of P(VDF-TrFE) is relatively high to that of the solvent cast PVDF and ITO etched PVDF. It may be due to conduction occurring at low frequencies [121].

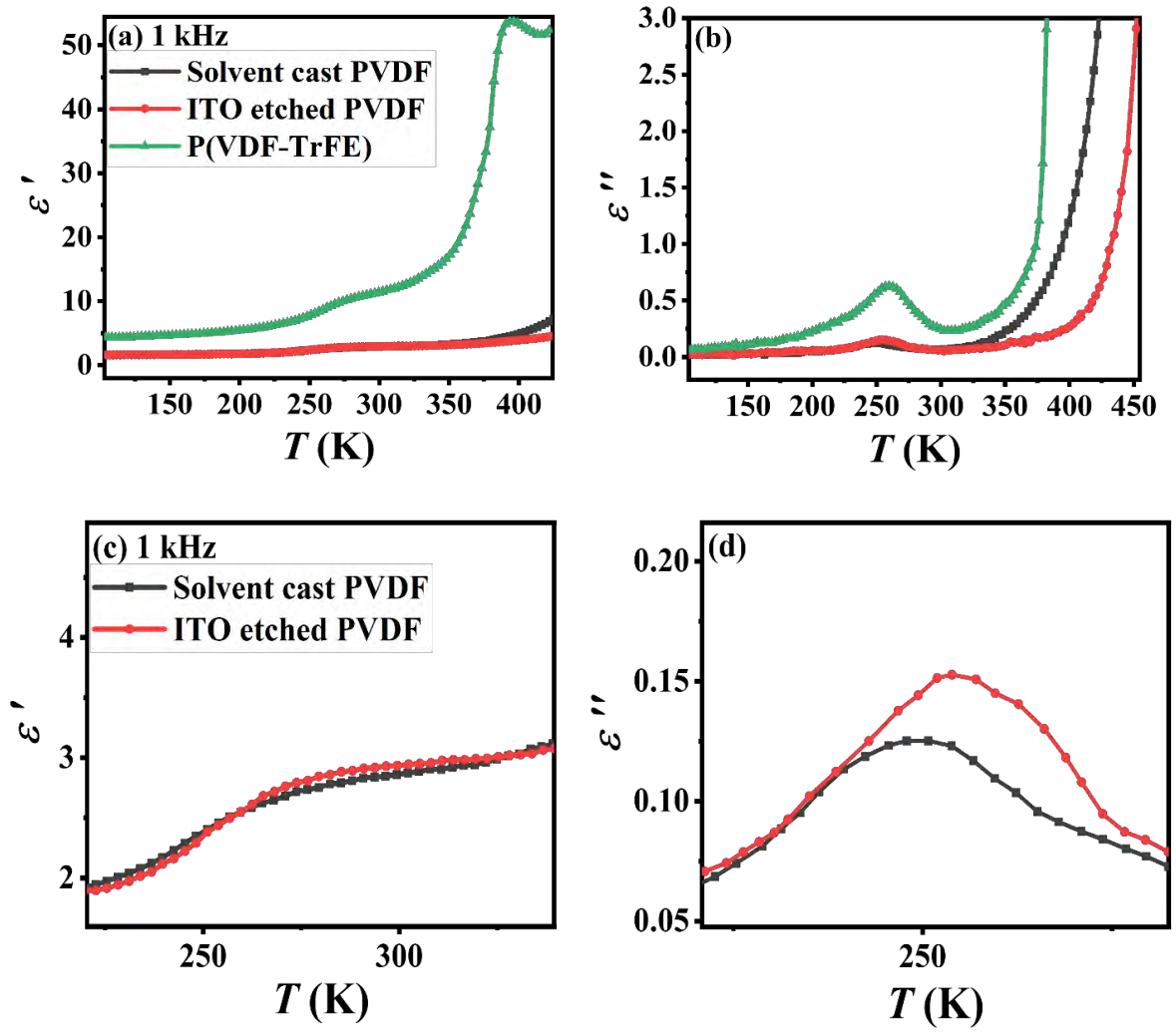

Figure 4.3 (a) Real part of solvent cast PVDF, ITO etched PVDF and P(VDF-TrFE), (b) Imaginary part of solvent cast PVDF, ITO etched PVDF and P(VDF-TrFE), (c) Real part of T_g of Solvent cast PVDF and ITO etched PVDF, (d) Imaginary part of T_g of Solvent cast PVDF and ITO etched PVDF.

Sample name	Glass transition temperature (T_g) (1 kHz)	ε' (1 kHz)	ε'' (1 kHz)
Solvent Cast PVDF	253.8	2.78	0.12
ITO etched PVDF	253.7	2.88	0.15
P(VDF-TrFE)	260.1	10.18	0.63

Table 4.1 Dielectric parameters calculated for solvent cast PVDF, ITO etched PVDF and P(VDF-TrFE) at 1 kHz.

Table 4.1 displays the glass transition temperature (T_g), dielectric constant (ε'), dielectric loss (ε'') for all the three samples at 1 kHz. The dielectric constant (ε') in P(VDF-TrFE) is higher than that of solvent cast PVDF and ITO etched PVDF. ε' in P(VDF-TrFE) is attributed to larger dipole moment. This larger dipole moment results in a larger value of in-phase component of dielectric permittivity. TrFE addition results in an increase of dielectric loss (ε'') component, hence ε'' of P(VDF-TrFE) is larger than that of solvent cast PVDF and ITO etched PVDF. ε' and ε'' in solvent cast PVDF and ITO etched PVDF are almost comparable.

4.2 Activation energy of solvent cast PVDF, ITO etched PVDF and P(VDF-TrFE):

Arrhenius law is used to determine the activation energy (E_a) related to β-relaxation for solvent cast PVDF, ITO etched PVDF and P(VDF-TrFE). Equation 4.1 represents the Arrhenius equation used to calculate E_a.

$$f = f_o e^{E_a/K_B T} \qquad 4.1$$

Where f is rate constant, f_o represents pre-exponential factor, E_a represents activation energy, K_B is Boltzmann constant, and T is temperature. Linear fitting for solvent cast PVDF, ITO etched PVDF and P(VDF-TrFE) is presented in Figure 4.4. Table 4.2 represents the data used to calculate E_a and Table 4.3 provides all the calculated activation energies for solvent cast PVDF, ITO etched PVDF and P(VDF-TrFE).

Frequency (Hz)	Solvent cast PVDF	ITO Etched PVDF	P(VDF-TrFE)
1 k	271.64	271.05	271.87
5 k	277.64	276.6	278.25
10 k	280.54	279.5	281.12
25 k	284.3	283.9	285.88
50 k	286.73	287.98	289.2
100 k	290.11	291.79	293.9
250 k	297.14	297.8	299.96
500 k	302.4	303.4	305.1
750 k	306.8	307.78	308.49
1 M	309.23	311.59	310.4

Table 4.2 Temperatures of β-relaxation peak at different frequencies for solvent cast PVDF, ITO etched PVDF and P(VDF-TrFE)

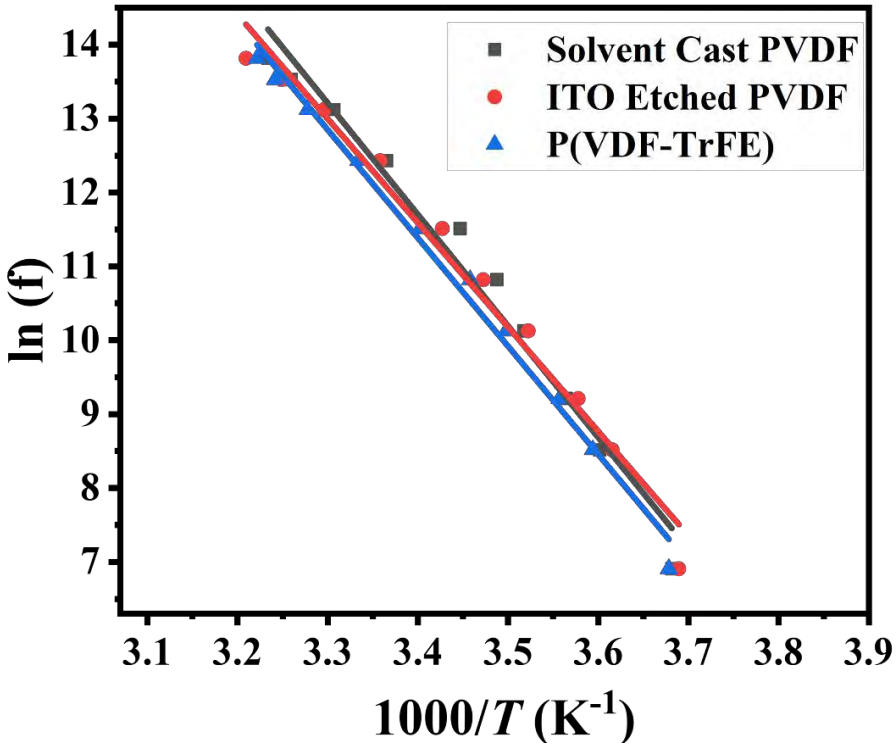

Figure 4.4 Arrhenius plots for E_a of solvent cast PVDF, ITO etched PVDF and P(VDF-TrFE)

It is observed that E_a lies within the range of 1.26-1.30 eV. Activation energy calculated for ITO etched PVDF and P(VDF-TrFE) is lower as compared to solvent cast PVDF because of the better alignment of dipoles and higher crystallinity.

Sample name	Activation Energy (eV)
Solvent Cast PVDF	1.30
ITO Etched PVDF	1.21
P(VDF-TrFE)	1.26

Table 4.3 E_a calculated from β-relaxation peak for solvent cast PVDF, ITO etched PVDF and P(VDF-TrFE)

4.3 Ferroelectric measurements:

Ferroelectric hysteresis loops (*P-E*) were measured at room temperature with 25 V increment per step. *P-E* loops are measured at 10 Hz frequency for all the prepared samples. The Sawyer Tower circuit was used for the measurement of ferroelectric loops.

4.3.1 Polarization versus Electric field response of solvent cast PVDF, PVDF/ITO and ITO etched PVDF and P(VDF-TrFE):

Ferroelectric hysteresis loop of solvent cast PVDF at room temperature is shown in Figure 4.5. Solvent cast PVDF exhibits lossy hysteresis loops without attaining maximum polarization.

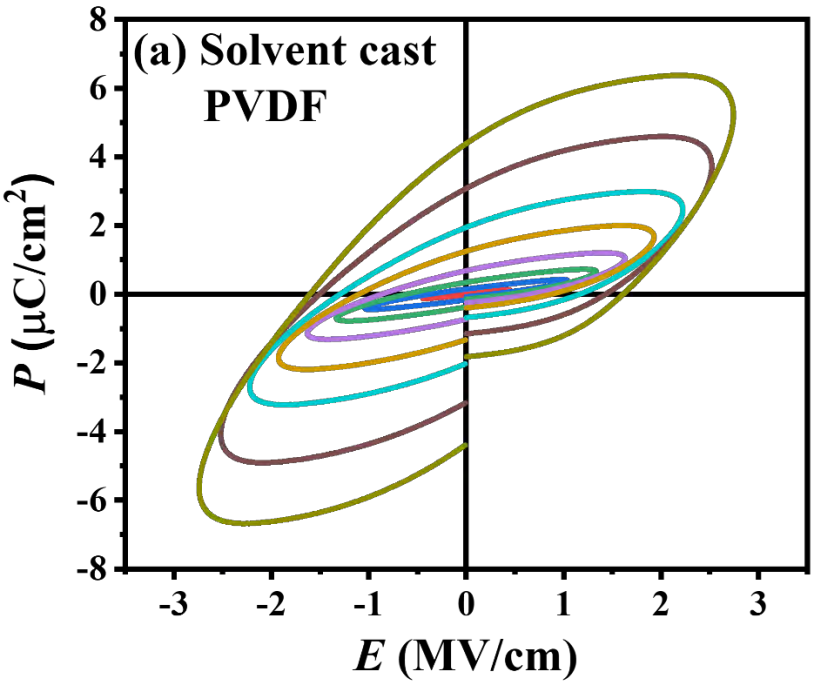

Figure 4.5 $P-E$ loops of Solvent cast PVDF.

At 10 Hz frequency, elliptical loops were observed for solvent cast PVDF as shown in Figure 4.5 (a). Which demonstrates the lossy nature of solvent cast PVDF. This lossy capacitive response at low frequency is attributed to space charge polarization. When electric field is applied to solvent cast PVDF, dipoles try to align themselves in the direction of applied field. Some of the charges get trapped at the interfacial barriers or crystal defects [108, 122]. Due to applied field, these charges result in motion. This motion of trapped charges causes interfacial polarization. Trapped charges at the interfaces induce their electric field which generates in opposite direction as compared to the external applied electric field. The opposing field within material is responsible for the elliptical shaped loop.

Ferroelectric hysteresis loops of PVDF/ITO and ITO etched PVDF samples are shown in Figure 4.6 (a and b). In PVDF/ITO sample non-saturated and resistive ferroelectric hysteresis loops are observed. While, in ITO etched PVDF saturated ferroelectric loops are observed when compared with PVDF/ITO sample.

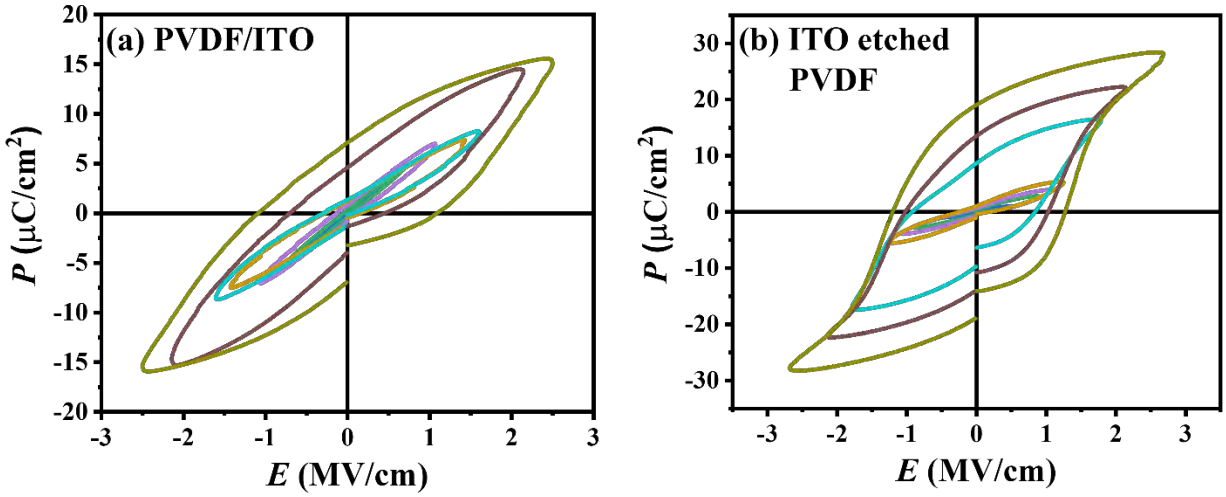

Figure 4.6 $P-E$ loops of (a) PVDF/ITO and (b) ITO etched PVDF

Loops of PVDF/ITO are not saturated. XRD of PVDF/ITO confirms the presence of crystalline β-phase but the loops observed are resistive due to low electrical conductivity as compared to silver (Ag) electrodes. ITO is an n-type degenerate semiconductor and has a maximum number of free electrons, and these free electrons are released by tin as a doping element. Extrinsic electron-donor dopant species Sn^{4+} ions replacing In^{3+} ions and generate one free electron which is responsible for the flow of electricity in ITO [123].

In contrast, ITO etched PVDF shows saturated ferroelectric behavior as compared to PVDF/ITO. Presence of crystalline β-phase in PVDF/ITO and ITO etched PVDF is already claimed in XRD. After etching of ITO electrodes, silver (Ag) electrodes were sputtered on the β-PVDF sheet. Like ITO, there are no free charge carriers present in Ag electrodes which are responsible for the generation of leakage current. Hence, leakage current get reduced and saturated hysteresis loops are observed.

Ferroelectric hysteresis loops of P(VDF-TrFE) sample are shown in Figure 4.7. Well saturated hysteresis loops are observed in P(VDF-TrFE) sample as compared to solvent cast PVDF, PVDF/ITO and etched ITO PVDF sample. However, in P(VDF-TrFE) as shown in Square shaped hysteresis loops are observed at higher electric field which is a sign of low leakage current and high crystallinity of the sample. The ferroelectric property in P(VDF-TrFE) arises due to the dipole created between H^+ and F^- atoms on either side of -C-C- chains. Addition of TrFE monomers results in the direct crystallization of ferroelectric β-phase [124].

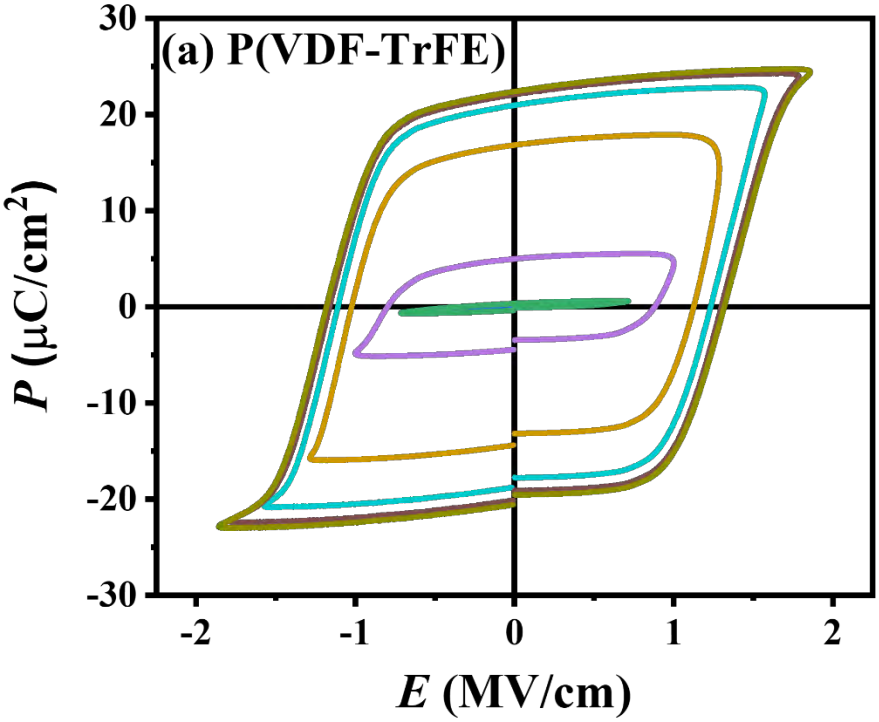

Figure 4.7 $P - E$ loops of Solvent cast PVDF.

Figure 4.8 illustrates the comparison of ferroelectric loops of solvent cast PVDF, PVDF/ITO, ITO etched PVDF and P(VDF-TrFE) sample at approximately 1.3 MV/cm electric field. Solvent cast PVDF sample exhibits a circular loop indicating a high percentage of leakage current in the system. PVDF/ITO sample indicates a resistive behavior but less lossy as compared to solvent cast PVDF sample. When ITO was etched from PVDF concentration of free charge carriers get reduced and saturation increases in ITO etched PVDF sample. While a well saturated hysteresis loop is observed in P(VDF-TrFE) sample.

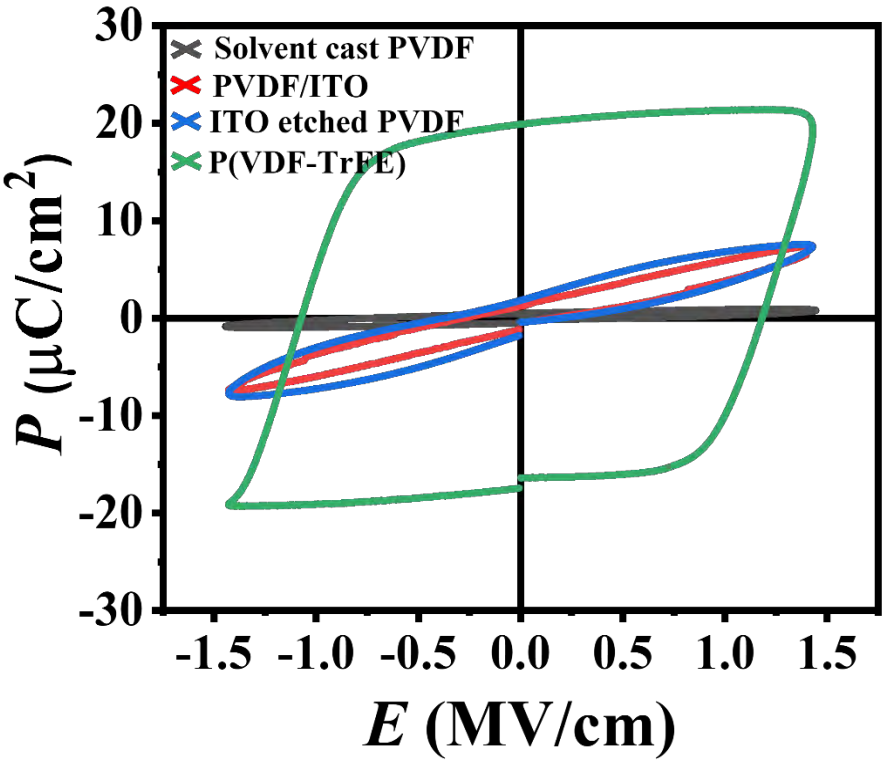

Figure 4.8 Comparison of $P-E$ loops of solvent cast PVDF, PVDF/ITO, ITO etched PVDF and P(VDF-TrFE) at 1.3 MV/cm

Maximum polarization (P_m), coercivity (E_c) and remanent polarization (P_r) is calculated for all the samples at around 1.3 MV/cm and is presented in Table 4.4. The value of P_m, P_r and E_c is larger in P(VDF-TrFE) as compared to solvent cast PVDF, PVDF/ITO and ITO etched PVDF sample.

Solvent cast PVDF has the lowest values of P_m and P_r, which is due to the higher percentage of leakage current. Values of P_m and P_r in PVDF/ITO is larger than that of solvent cast PVDF because β-phase is achieved in PVDF/ITO as claimed in XRD, but these values are small when compared to ITO etched PVDF and P(VDF-TrFE) due to the large concentration of free charge carriers. After etching of ITO, concentration of free charge carriers decreases which results in larger value of P_m and P_r. P(VDF-TrFE) exhibits larger values of P_m and P_r and these large values are attributed to larger dipole moment [97]. Addition of TrFE monomers to PVDF results in larger dipole moment as hydrogen atoms are replaced by fluorine atoms. F-atom is more electronegative than H-atom. Hence, the more electronegative an atom is, the larger will be the dipole moment or large electronegativity difference between atoms will result in larger value of dipole moment. Carbon has an electronegativity equal to 2.5, while F-atom has an electronegativity equal to 4.0 [121]. The

difference between their electronegativity is 1.5. In contrast, the electronegativity of C-atom and H-atom is 2.5 and 2.1 respectively [125]. Their electronegativity difference is equal to just 0.4, which is less than that of C and F-atom. So, this larger difference in electronegativity leads to larger dipole moment.

P(VDF-TrFE) possesses larger E_c value than that of solvent cast PVDF, PVDF/ITO and ITO etched PVDF which is due to the larger dipole moment and hence large E_c is required to change the direction of polarization.

Sample name	P_m (μC/cm²)	P_r (μC/cm²)	E_c (MV/cm)
Solvent Cast PVDF	0.90	0.477	0.72
PVDF/ITO	7.404	1.219	0.43
ITO etched PVDF	7.558	1.383	0.56
P(VDF-TrFE)	28.306	19.887	1.07

Table 4.4 $P-E$ loop parameters of solvent cast PVDF, PVDF/ITO, ITO etched PVDF and P(VDF-TrFE)

4.4 Molecular structure of PVDF and P(VDF-TrFE):

PVDF is composed of the repeating unit (CH_2-CF_2). The internal rotation of the polymer's single bond results in the cause of difference between the spatial arrangements of groups and molecular backbone structures. When the molecular segments are arranged in a manner where they are 180° apart from each other with respect to the carbon backbone, it is referred to as a trans bond (T). In contrast, when the angle between them is either +60° or -60°, it is termed as a gauche bond (+G/-G). As a result, the PVDF molecular chains exhibit a variety of conformations and phase structures [40, 126].

Figure 4.9 represents the molecular structure of α-phase of PVDF drawn by using ChemDraw 3D software. α-phase has TGTG' helical conformations and is non-polar in nature. In this conformation, CF_2-CH_2 are antiparallel and making a trans bond (T). Furthermore, the angle between CH_2 and CF_2 is 60° and results in gauche bond (G). Then followed by trans and inverse gauche bond as shown in below figure. Due to the antiparallel

stacking of the two molecular chains in the crystals unit cell of the α-phase, the dipoles almost cancel out one another, thus resulting in no net dipole moment. Due to zero net dipole moment, α-phase has very small value of remanent polarization and also results in small value of dielectric permittivity. The circle around the atoms represents the surface of electron cloud [126]. XRD and FTIR analysis indicates the presence of α-phase in solved casted PVDF sample. Ferroelectric hysteresis loops of this sample also give a lossy response which is also an indication of the presence of some percentage of non-polar α-phase in solved casted PVDF sample.

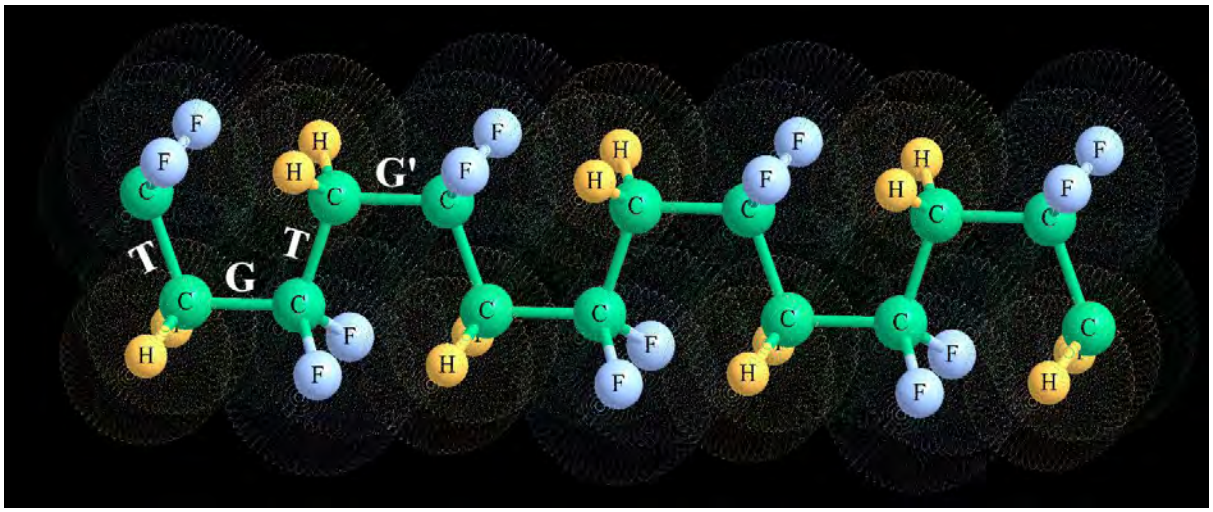

Figure 4.9 Structure of α-phase drawn by using ChemDraw 3D.

Figure 4.10 illustrates the β-phase (TTTT) of PVDF, where T is the symbol for trans bond that maintains alignment with the carbon backbone within the same plane. β-phase is the most highly polar conformation of the molecular chains. The chains are arranged in a plane zigzag all-trans conformation (TTTT) with CF_2 and CH_2 group facing one side each. In this arrangement, dipoles are oriented perpendicular to the chain axis. In literature, an alternatively deflected molecular chain structure is reported to explain the steric hindrance of fluorine atoms in the molecular chain. This structure can decrease the steric hindrance between fluorine atoms and lower the molecular potential energy [42, 126]. β-phase has less conformational defects and large dipole moment as compared to α-phase which results in high dielectric value and exhibits excellent ferroelectricity as shown in section 4.3.1. XRD and FTIR of PVDF/ITO and ITO etched PVDF indicates the presence of β-phase. PVDF/ITO exhibits resistive ferroelectric loops due to the presence of higher concentration of free charge carriers in ITO. ITO etched PVDF shows improved ferroelectric response when compared

with PVDF/ITO. The dielectric response of solvent cast PVDF and ITO etched PVDF are comparable.

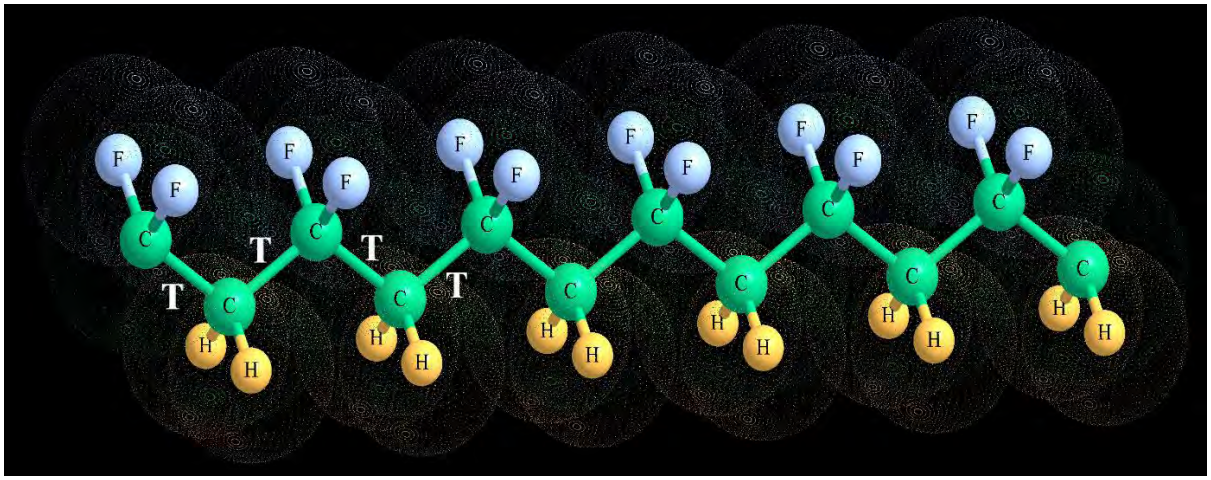

Figure 4.10 Structure of β-phase

T_3GT_3G' is the configuration of gamma phase (γ). γ-phase has 3 trans (T) and one gauche bond (G) as shown in Figure 4.11. γ-phase is less polar than β-phase because it's density of dipole moment is smaller than that of β-phase. So, β-phase is more preferred over γ-phase [127]. Minor dips of γ-phase is only reported in FTIR of solvent cast PVDF.

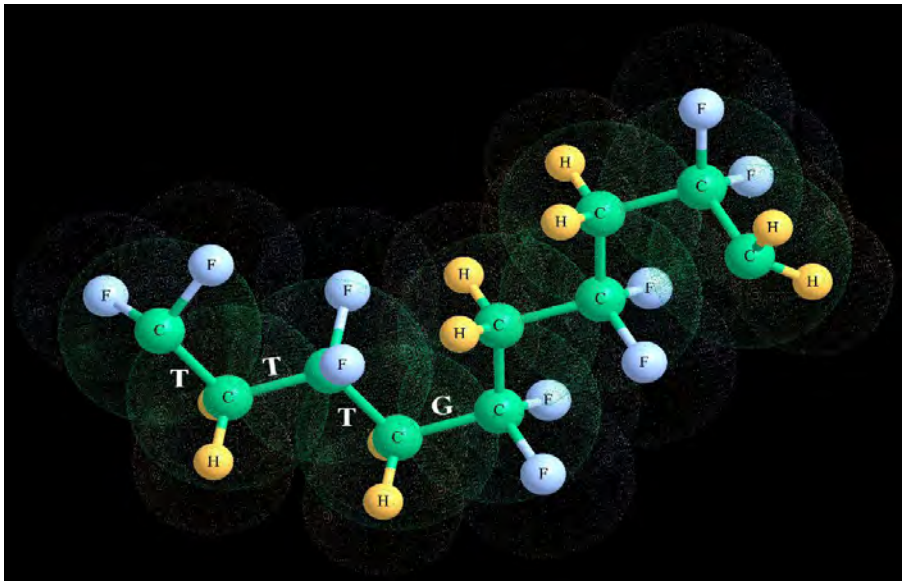

Figure 4.11 Structure of γ-phase

Figure 4.12 illustrates the 3D molecular structure of P(VDF-TrFE). P(VDF-TrFE) exhibits crystalline β-phase as claimed in XRD and FTIR. In β-phase all polymer chains are in the trans (TTTT) conformation, and the fluorine atoms are arranged unilaterally in the

chain. Addition of TrFE content into the copolymer favor the trans bonds over gauche bonds due to the replacement of hydrogen with fluorine. This replacement results in a larger dipole moment due to larger electronegativity difference between carbon atom and fluorine atom. This large dipole moment results in large value of dielectric constant and also enhanced ferroelectric property. The large size of fluorine atom leads to greater steric hindrance, which results in β-phase [50, 126]. P(VDF-TrFE) exhibits large dielectric value as compared to solvent cast PVDF and ITO etched PVDF. In the dielectric spectrum of P(VDF-TrFE) transition from ferro-electric to para-electric is observed. The phase transition occurs at T_c=395 K. At T_c chain conformation changes from TTTT to TTTG. P(VDF-TrFE) exhibits square loops.

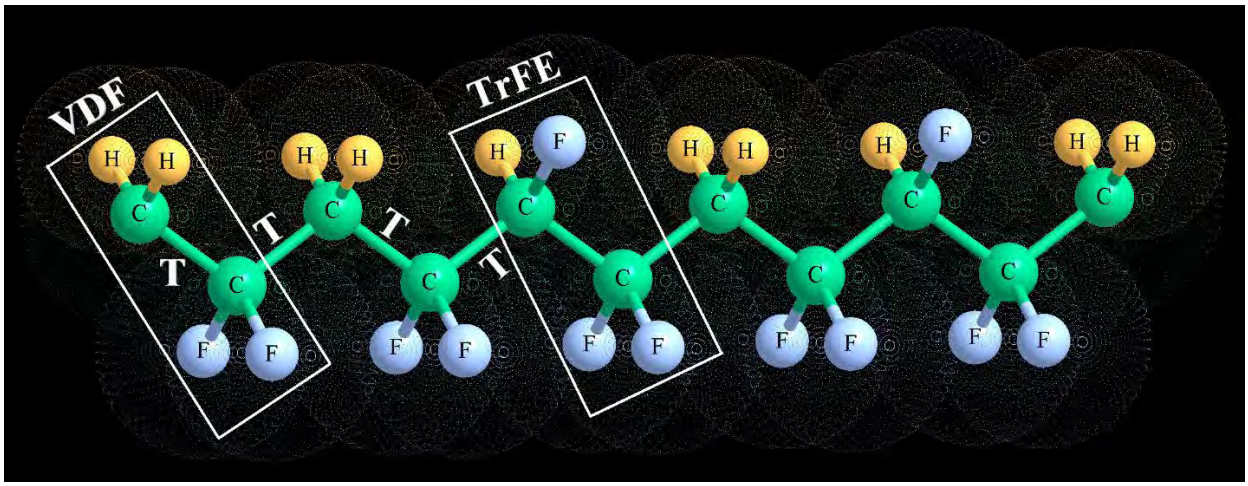

Figure 4.12 3D structure of P(VDF-TrFE) chains.

4.4 Summary and Conclusion:

This work mainly focuses on the electrical (dielectric and ferroelectric) properties of solvent cast PVDF, P(VDF-TrFE) and ITO etched PVDF. Thick films of solvent cast PVDF and P(VDF-TrFE) are prepared by using solvent cast technique. β-PVDF (extracted from PVDF/ITO) was purchased, and ITO was etched by using HCl as an etchant agent. XRD and FTIR were done for the structural analysis of these thick films. XRD spectrum of solvent cast PVDF confirms the presence of α and β-phase. A small hump was observed along with crystalline β-phase in PVDF/ITO and ITO etched PVDF, while only β-phase is observed in P(VDF-TrFE). FTIR confirmed the XRD results. FTIR also confirmed that the small hump observed in PVDF/ITO and ITO etched PVDF is attributed to α-phase. P(VDF-TrFE) exhibits higher crystallinity than solvent cast PVDF, PVDF/ITO and ITO etched PVDF. This high crystallinity is due to the difference in steric hindrance between CHF and CH_2. When more than 20% TrFE content is added to PVDF, severe hindrance between fluorine atoms occurs in α-phase and directly results in crystalline β-phase.

The first two regions of dielectric spectrum of solvent cast PVDF, ITO etched PVDF and P(VDF-TrFE) are same. The only difference between them is a phase transition, that occurs only in P(VDF-TrFE) because with the addition of TrFE content, crystallinity increases, and it exhibits excellent ferroelectricity. The dielectric constant value of P(VDF-TrFE) is larger than that of solvent cast PVDF and ITO etched PVDF. This large value of P(VDF-TrFE) is attributed to large dipole moment. While the dielectric constant values of solvent cast PVDF and ITO etched PVDF are comparable.

Ferroelectric $P-E$ measurement of solvent cast PVDF show lossy loops, which indicates higher leakage current. PVDF/ITO sample shows resistive loops due to lower electrical conductivity, but the percentage of leakage current in PVDF/ITO is less than that of solvent cast PVDF. After etching of ITO, saturated loops are observed because concentration of free charge carrier's get reduced. Square and well saturated loops are observed in P(VDF-TrFE), which corresponds to excellent ferroelectricity.

The hysteresis loops of solvent cast PVDF, PVDF/ITO, ITO etched PVDF and P(VDF-TrFE) are compared at 1.3 MV/cm. Large values of maximum polarization (P_m) and remanent polarization (P_r) is observed in P(VDF-TrFE) as compared to solvent cast PVDF, PVDF/ITO and ITO etched PVDF which is due to large dipole moment and excellent

ferroelectricity. P_m and P_r values of ITO etched PVDF is greater than that of PVDF/ITO and solvent cast PVDF because of the decrease in concentration of free charge carriers. Solvent cast PVDF exhibit less value of P_m and P_r when compared with PVDF/ITO, ITO etched PVDF and P(VDF-TrFE), which is due to the low crystallinity and lossy loops observed.

Hence, this study shows that dilute HCl can be used as an etchant agent for removing ITO electrodes. It is observed that after etching of ITO from PVDF, the electrical response of ITO etched PVDF is enhanced as observed in dielectric and ferroelectric $P-E$ loops. The addition of TrFE content to PVDF further enhanced ferroelectricity as claimed in its electrical response. Large value of dielectric constant and well-saturated $P-E$ loops are observed in P(VDF-TrFE) sample when compared with solvent cast PVDF, PVDF/ITO and ITO etched PVDF. P(VDF-TrFE) can be used in the field of energy storage due to its large dielectric value. It can also be used in a piezoelectric device due to large remanent polarization (P_r).

References:

1. Haga, Y. and M. Esashi, *Biomedical microsystems for minimally invasive diagnosis and treatment.* Proceedings of the IEEE, 2004. **92**(1): p. 98-114.
2. Li, C., et al., *Flexible dome and bump shape piezoelectric tactile sensors using PVDF-TrFE copolymer.* Journal of Microelectromechanical Systems, 2008. **17**(2): p. 334-341.
3. Meng, N., et al., *Nanoscale interfacial electroactivity in PVDF/PVDF-TrFE blended films with enhanced dielectric and ferroelectric properties.* Journal of Materials Chemistry C, 2017. **5**(13): p. 3296-3305.
4. Sukumaran, S., et al., *Recent advances in flexible PVDF based piezoelectric polymer devices for energy harvesting applications.* Journal of Intelligent Material Systems and Structures, 2021. **32**(7): p. 746-780.
5. Gutiérrez-Sánchez, G., et al. *Comparative assessment of PVDF and PVDF-TrFE piezoelectric polymers for flexible actuators applications*. in *Smart Sensors, Actuators, and MEMS VIII*. 2017. SPIE.
6. Saxena, P. and P. Shukla, *A comprehensive review on fundamental properties and applications of poly (vinylidene fluoride)(PVDF).* Advanced Composites and Hybrid Materials, 2021. **4**: p. 8-26.
7. Curie, J. and P. Curie, *Développement par compression de l'électricité polaire dans les cristaux hémièdres à faces inclinées.* Bulletin de minéralogie, 1880. **3**(4): p. 90-93.
8. Lu, H. and A. Gruverman, *Piezoresponse force microscopy for functional imaging of organic ferroelectrics*, in *Organic Ferroelectric Materials and Applications*. 2022, Elsevier. p. 233-262.
9. Ruan, L., et al., *Properties and applications of the β phase poly (vinylidene fluoride).* Polymers, 2018. **10**(3): p. 228.
10. Jia, N., et al., *Crystallization behavior and electroactive properties of PVDF, P (VDF-TrFE) and their blend films.* Polymer Testing, 2017. **57**: p. 302-306.
11. Kao, K.C., *Dielectric phenomena in solids*. 2004: Elsevier.
12. Kittel, C. and P. McEuen, *Introduction to solid state physics*. 2018: John Wiley & Sons.
13. *Band Gap for Semiconductor Materials*. 2023; Available from: https://instrumentationtools.com/band-gap/.
14. Khan, M.T. and S.M. Ali, *A brief review of measuring techniques for characterization of dielectric materials.* International Journal of Information Technology and Electrical Engineering, 2012. **1**(1).
15. Peiris, N., *Microwave-assisted processing of solid materials for sustainable energy related electronic and optoelectronic applications*. 2014, Loughborough University Loughborough.
16. Dalkin, T., *Conduction and polarization mechanisms and trends in dielectrics.* IEEE Electrical Insulation Magazine, 2006. **22**(5): p. 11-28.
17. Jayaram Balasubramanyam, M.L.K.S., Sujith Thomas *Lecture Notes on Engineering Physics*. 2014.
18. Sawada, A., *Theory of space-charge polarization for determining ionic constants of electrolytic solutions.* The Journal of chemical physics, 2007. **126**(22): p. 224515.
19. Chaudhari, V.A. and G.K. Bichile, *Synthesis, structural, and electrical properties of pure PbTiO3 ferroelectric ceramics.* Smart Materials Research, 2013. **2013**.
20. Lines, M.E. and A.M. Glass, *Principles and applications of ferroelectrics and related materials*. 2001: Oxford university press.
21. Raju, G.G., *Dielectrics in electric fields: Tables, Atoms, and Molecules*. 2017: CRC press.
22. Usman, M., *Studies of Ferroelectric and Multiferroic Behavior in [Ba(Zr,Ti)O3]1-y:[CoFe2O4]y System*. 2015, Quaid e Azam university: Islamabad
23. Shirane, G. and S. Hoshino, *On the phase transition in lead titanate.* Journal of the Physical Society of Japan, 1951. **6**(4): p. 265-270.

24. Bain, A.K. and P. Chand, *Ferroelectrics: Principles and applications*. 2017: John Wiley & Sons.
25. Dineva, P., et al., *Piezoelectric materials*. 2014: Springer.
26. Qiu, J. and H. Ji, *The application of piezoelectric materials in smart structures in China.* International Journal of Aeronautical and Space Sciences, 2010. **11**(4): p. 266-284.
27. *What is Piezoelectric Effect?* 2022 24-01-2022; Available from: https://www.circuitbread.com/ee-faq/what-is-piezoelectric-effect.
28. Adil Wazeer, A.D., Arijit Sinha, Amit Karmakar, *Piezoelectric Polymer Composites for Energy Harvesting.* Springer, 2022.
29. Nor, N.M., H.H. Hamzah, and K.A. Razak, *Recent advancement in sustainable energy harvesting using piezoelectric materials*, in *Sustainable Materials for Next Generation Energy Devices*. 2021, Elsevier. p. 221-248.
30. Maity, K. and D. Mandal, *Piezoelectric polymers and composites for multifunctional materials*, in *Advanced Lightweight Multifunctional Materials*. 2021, Elsevier. p. 239-282.
31. Lang, S.B., *Pyroelectricity: from ancient curiosity to modern imaging tool.* Physics today, 2005. **58**(8): p. 31.
32. Zhang, D., et al., *Recent advances in pyroelectric materials and applications.* Small, 2021. **17**(51): p. 2103960.
33. Lin, Y., et al., *Studies on the electrostatic effects of stretched PVDF films and nanofibers.* Nanoscale Research Letters, 2021. **16**(1): p. 79.
34. Nguyen, M.D., et al., *Experimental evidence of breakdown strength and its effect on energy-storage performance in normal and relaxor ferroelectric films.* Current Applied Physics, 2019. **19**(9): p. 1040-1045.
35. Devonshire, A., *Theory of ferroelectrics.* Advances in physics, 1954. **3**(10): p. 85-130.
36. Yan, H., et al., *The contribution of electrical conductivity, dielectric permittivity and domain switching in ferroelectric hysteresis loops.* Journal of Advanced Dielectrics, 2011. **1**(01): p. 107-118.
37. Guo, F., Y. Liu, and S. Zhao, *The modification of contribution: electric conductivity, dielectric displacement and domain switching in ferroelectric hysteresis loops.* Applied Physics A, 2020. **126**: p. 1-7.
38. Haertling, G.H., *Ferroelectric ceramics: history and technology.* Journal of the American Ceramic Society, 1999. **82**(4): p. 797-818.
39. Khan, K.A., et al., *Time-dependent and energy dissipation effects on the electro-mechanical response of PZTs.* Mechanics of Materials, 2016. **102**: p. 74-89.
40. Cui, Z., et al., *Crystalline polymorphism in poly (vinylidenefluoride) membranes.* Progress in Polymer Science, 2015. **51**: p. 94-126.
41. Benz, M. and W.B. Euler, *Determination of the crystalline phases of poly (vinylidene fluoride) under different preparation conditions using differential scanning calorimetry and infrared spectroscopy.* Journal of applied polymer science, 2003. **89**(4): p. 1093-1100.
42. Weinhold, S., et al., *Orthorhombic vs. monoclinic structures for the α and γ phases of poly (vinylidene fluoride): an analysis.* Macromolecules, 1982. **15**(6): p. 1631-1633.
43. Sharma, M., G. Madras, and S. Bose, *Process induced electroactive β-polymorph in PVDF: effect on dielectric and ferroelectric properties.* Physical Chemistry Chemical Physics, 2014. **16**(28): p. 14792-14799.
44. Fujisaki, Y., *Poly (vinylidenefluoride-trifluoroethylene) P (VDF-TrFE)/semiconductor structure ferroelectric-gate FETs.* Ferroelectric-Gate Field Effect Transistor Memories: Device Physics and Applications, 2016: p. 157-183.
45. Lovinger, A.J., *Annealing of poly (vinylidene fluoride) and formation of a fifth phase.* Macromolecules, 1982. **15**(1): p. 40-44.
46. Shepelin, N.A., et al., *New developments in composites, copolymer technologies and processing techniques for flexible fluoropolymer piezoelectric generators for efficient energy harvesting.* Energy & Environmental Science, 2019. **12**(4): p. 1143-1176.

47. Kepler, R. and R. Anderson, *Adv. In Phys.* Adv. in Phys, 1992. **41**: p. 1.
48. Li, M., et al., *Ferroelectric phase diagram of PVDF: PMMA.* Macromolecules, 2012. **45**(18): p. 7477-7485.
49. Li, G.R., N. Kagami, and H. Ohigashi, *The possibility of formation of large ferroelectric domains in a copolymer of vinylidene fluoride and trifluoroethylene.* Journal of applied physics, 1992. **72**(3): p. 1056-1061.
50. Chen, X.-Z., et al., *A polymer blend approach to tailor the ferroelectric responses in P (VDF–TrFE) based copolymers.* Polymer, 2013. **54**(9): p. 2373-2381.
51. Bouden, S., et al., *Multifunctional indium tin oxide electrode generated by unusual surface modification.* Scientific Reports, 2016. **6**(1): p. 1-9.
52. Bhavanasi, V., et al., *Enhanced piezoelectric energy harvesting performance of flexible PVDF-TrFE bilayer films with graphene oxide.* ACS applied materials & interfaces, 2016. **8**(1): p. 521-529.
53. Liu, Z., et al., *Flexible piezoelectric nanogenerator in wearable self-powered active sensor for respiration and healthcare monitoring.* Semiconductor Science and Technology, 2017. **32**(6): p. 064004.
54. Dash, S., et al., *Enhanced dielectric properties and theoretical modeling of PVDF–ceramic composites.* Journal of Materials Science: Materials in Electronics, 2019. **30**: p. 19309-19318.
55. Zhang, L. and Z.-Y. Cheng, *Development of polymer-based 0–3 composites with high dielectric constant.* Journal of Advanced Dielectrics, 2011. **1**(04): p. 389-406.
56. Sebastian, M.T. and H. Jantunen, *Polymer–ceramic composites of 0–3 connectivity for circuits in electronics: a review.* International Journal of Applied Ceramic Technology, 2010. **7**(4): p. 415-434.
57. Siemann, U., *Solvent cast technology–a versatile tool for thin film production*, in *Scattering methods and the properties of polymer materials*. 2005, Springer. p. 1-14.
58. Kumar, K. and D. Teotia, *A comprehensive review on pharmaceutical Oral dissolving films.* Journal of Drug Delivery and Therapeutics, 2019. **9**(5-s): p. 170-174.
59. Katiyar, N. and K. Balasubramanian, *Nano-heat-sink thin film composite of PC/three-dimensional networked nano-fumed silica with exquisite hydrophobicity.* RSC advances, 2015. **5**(6): p. 4376-4384.
60. Lade Milind, S., et al., *Polymer based wafer technology: A Review.* International Journal of Pharmaceutical & Biological Archives, 2013. **4**(6): p. 1060-1074.
61. Kohlmann, H., *100 years in situ diffraction.* Zeitschrift für Kristallographie-Crystalline Materials, 2017. **232**(12): p. 843-849.
62. Bunaciu, A.A., E.G. UdriŞTioiu, and H.Y. Aboul-Enein, *X-ray diffraction: instrumentation and applications.* Critical reviews in analytical chemistry, 2015. **45**(4): p. 289-299.
63. Darrell Henry, D.M. *X-ray reflection in accordance with Bragg's Law*. 2016; Available from: https://serc.carleton.edu/research_education/geochemsheets/BraggsLaw.html.
64. Seeck, O.H. and B. Murphy, *X-ray Diffraction: Modern Experimental Techniques*. 2015: CRC Press.
65. Hsu, C.-P.S., *Infrared spectroscopy.* Handbook of instrumental techniques for analytical chemistry, 1997. **249**.
66. *Nicolet 5700 FTIR spectrometer*. 2006; Available from: http://icems.ist.utl.pt/reeq/FTIR.html.
67. Xu-Ling, L., et al., *Preliminary result of bunch length measurement using a modified Michelson interferometer.* Chinese Physics C, 2009. **33**(10): p. 901.
68. *Michelson Interferometer*. 2023; Available from: https://wanda.fiu.edu/boeglinw/courses/Modern_lab_manual3/michelson.html.
69. Jaggi, N. and D. Vij, *Fourier transform infrared spectroscopy*, in *Handbook of Applied Solid State Spectroscopy*. 2006, Springer. p. 411-450.

70. Tarantilis, P., et al., *Differentiation of Greek red wines on the basis of grape variety using attenuated total reflectance Fourier transform infrared spectroscopy.* Food Chemistry, 2008. **111**(1): p. 192-196.
71. Smentkowski, V.S., *Trends in sputtering.* Progress in Surface Science, 2000. **64**(1-2): p. 1-58.
72. Thornton, J.A., *Sputter Coating—Its Principles and Potential.* SAE Transactions, 1973: p. 1787-1805.
73. Simić, M. *Realization of digital LCR meter*. in *2014 International Conference and Exposition on Electrical and Power Engineering (EPE)*. 2014. IEEE.
74. Cryotronics, L.S. *Model 336 Temperature Controller*. Available from: https://www.lakeshore.com/docs/default-source/product-downloads/lstc_336_l.pdf?sfvrsn=462ca395_3.
75. *Parallel Plate Capacitor*. Available from: http://hyperphysics.phy-astr.gsu.edu/hbase/electric/pplate.html.
76. Sinha, J., *Modified Sawyer and Tower circuit for the investigation of ferroelectric samples.* Journal of Scientific Instruments, 1965. **42**(9): p. 696.
77. Zhu, H., T. Miyashita, and M. Mitsuishi, *Energy storage behaviors in ferroelectric capacitors fabricated with sub-50 nm poly (vinylidene fluoride) Langmuir–Blodgett nanofilms.* Polymer Journal, 2019. **51**(8): p. 795-801.
78. Loop, P.P. *Ferroelectric and Capacitor Test Station* Available from: http://www.polyktech.com/home/polyk-pe-loop.
79. PolyK. *Ferroelectric Polarization Loop and Dielectric Breakdown Test System*. Available from: https://piezopvdf.com/ferroelectric-polarization-loop-and-dielectric-breakdown-test-system/.
80. PolyK. *Piezotech P(VDF-TrFE) 70/30 mol Copolymer Resin 50 gram*. 2023; Available from: https://piezopvdf.com/piezotech-p-vdf-trfe-70-30-mol-50-gram/.
81. Li, L., et al., *Studies on the transformation process of PVDF from α to β phase by stretching.* Rsc Advances, 2014. **4**(8): p. 3938-3943.
82. Bera, B. and M.D. Sarkar, *Piezoelectricity in PVDF and PVDF based piezoelectric nanogenerator: a concept.* IOSR J. Appl. Phys, 2017. **9**(3): p. 95-99.
83. PolyK. *Optically transparent piezo film PVDF with ITO Electrode*. 2023; Available from: https://piezopvdf.com/PVDF-piezo-film-pvdf-ito/.
84. Mahato, P., et al., *Effect of fabrication technique on the crystalline phase and electrical properties of PVDF films.* Materials Science-Poland, 2015. **33**(1): p. 157-162.
85. Singh, P., et al., *Ferroelectric polymer-ceramic composite thick films for energy storage applications.* AIP advances, 2014. **4**(8).
86. Xia, W. and Z. Zhang, *PVDF-based dielectric polymers and their applications in electronic materials.* Iet Nanodielectrics, 2018. **1**(1): p. 17-31.
87. Badatya, S., et al., *Solution processed high performance piezoelectric eggshell membrane–PVDF layer composite nanogenerator via tuning the interfacial polarization.* Journal of Alloys and Compounds, 2021. **863**: p. 158406.
88. RP, V., D.V. Khakhar, and A. Misra, *Studies on α to β phase transformations in mechanically deformed PVDF films.* Journal of applied polymer science, 2010. **117**(6): p. 3491-3497.
89. Shukla, N., et al., *Low temperature ferroelectric behaviour of PVDF based composites.* 2008.
90. Esterly, D.M. and B.J. Love, *Phase transformation to β-poly (vinylidene fluoride) by milling.* Journal of Polymer Science Part B: Polymer Physics, 2004. **42**(1): p. 91-97.
91. Aliane, A., et al., *Impact of crystallization on ferro-, piezo-and pyro-electric characteristics in thin film P (VDF–TrFE).* Organic Electronics, 2015. **25**: p. 92-98.
92. Wang, F., et al., *All-organic poly (butyl methacrylate)/Poly (vinylidenefluoride-trifluoroethylene) dielectric composites with higher permittivity and low dielectric loss for Energy Storage Application.* Polymer-Plastics Technology and Engineering, 2017. **56**(5): p. 526-534.

93. Choi, Y.Y., et al., *Nanoscale piezoresponse of 70 nm poly (vinylidene fluoride-trifluoro-ethylene) films annealed at different temperatures.* physica status solidi (RRL)–Rapid Research Letters, 2010. **4**(3-4): p. 94-96.
94. Seo, J., J.Y. Son, and W.-H. Kim, *Piezoelectric and ferroelectric characteristics of P (VDF-TrFE) thin films on Pt and ITO substrates.* Materials Letters, 2019. **238**: p. 237-240.
95. Mao, D., B.E. Gnade, and M.A. Quevedo-Lopez, *Ferroelectric properties and polarization switching kinetic of poly (vinylidene fluoride-trifluoroethylene) copolymer.* Ferroelectrics-Physical Effects, 2011: p. 78-100.
96. Bandyopadhyay, R., et al., *Application of powder X-ray diffraction in studying the compaction behavior of bulk pharmaceutical powders.* Journal of pharmaceutical sciences, 2005. **94**(11): p. 2520-2530.
97. Li, Z., et al., *Ferro-and piezo-electric properties of a poly (vinyl fluoride) film with high ferro-to para-electric phase transition temperature.* RSC advances, 2015. **5**(99): p. 80950-80955.
98. *Jaffari, G. Hassnain, et al. "Manipulation of crystallization and dielectric relaxation dynamics via hot pressing and copolymerization of PVDF with Hexafluoropropylene." Journal of Polymer Research 30.1 (2023): 11.*
99. *Li, Junjie, et al. "Influence of crystalline properties on the dielectric and energy storage properties of poly (vinylidene fluoride)." Journal of Applied Polymer Science 122.3 (2011): 1659-1668.*
100. *Cai, Xiaomei, et al. "A critical analysis of the α, β and γ phases in poly (vinylidene fluoride) using FTIR." RSC advances 7.25 (2017): 15382-15389.*
101. *Lanceros-Mendez, S., et al. "FTIR and DSC studies of mechanically deformed β-PVDF films." Journal of Macromolecular Science, Part B 40.3-4 (2001): 517-527.*
102. *Dhakras, Dipti, et al. "Enhanced piezoresponse of electrospun PVDF mats with a touch of nickel chloride hexahydrate salt." Nanoscale 4.3 (2012): 752-756.*
103. *Shehzad, Mudassar, and Yaojin Wang. "Flexible and transparent flexoelectric microphone." Advanced Materials Technologies 8.3 (2023): 2200908.*
104. *Costa, C. M., et al. "Mesoporous poly (vinylidene fluoride-co-trifluoroethylene) membranes for lithium-ion battery separators." Electrochimica Acta 301 (2019): 97-106.*
105. *Arshad, A., et al., Dielectric and structural properties of poly (vinylidene fluoride)(PVDF) and poly (vinylidene fluoride-trifluoroethylene)(PVDF-TrFE) filled with magnesium oxide nanofillers. Journal of Nanomaterials, 2019. 2019.*
106. *Ryu, J., et al., Synthesis and application of ferroelectric poly (vinylidene fluoride-co-trifluoroethylene) films using electrophoretic deposition. Scientific reports, 2016. 6(1): p. 1-7.*
107. Jaffari, G.H., et al., *Manipulation of crystallization and dielectric relaxation dynamics via hot pressing and copolymerization of PVDF with Hexafluoropropylene.* Journal of Polymer Research, 2023. **30**(1): p. 11.
108. Jaffari, G.H., et al., *Electrical Response Pvdf/Batio3 Nanocomposite Flexible Free Standing Films.* Available at SSRN 4096130.
109. Teyssedre, G., A. Bernes, and C. Lacabanne, *Influence of the crystalline phase on the molecular mobility of PVDF.* Journal of Polymer Science Part B: Polymer Physics, 1993. **31**(13): p. 2027-2034.
110. Psarras, G., *Fundamentals of dielectric theories*, in *Dielectric Polymer Materials for High-Density Energy Storage*. 2018, Elsevier. p. 11-57.
111. Chen, J., et al., *Enhanced dielectric constant and hydrophobicity of P (VDF–TrFE)-based composites.* Journal of Materials Science: Materials in Electronics, 2018. **29**: p. 17612-17621.
112. Zhu, L., *Exploring strategies for high dielectric constant and low loss polymer dielectrics.* The journal of physical chemistry letters, 2014. **5**(21): p. 3677-3687.
113. Arifin, D.E.S. and d.J. Ruan. *Study on the curie transition of P (VDF-TrFE) copolymer*. in *IOP Conference Series: Materials Science and Engineering*. 2018. IOP Publishing.

114. Chung, T. and A. Petchsuk, *Synthesis and properties of ferroelectric fluoroterpolymers with Curie transition at ambient temperature.* Macromolecules, 2002. **35**(20): p. 7678-7684.
115. Meereboer, N.L., et al., *Pronounced surface effects on the Curie transition temperature in nanoconfined P (VDF-TrFE) crystals.* Macromolecules, 2019. **52**(4): p. 1567-1576.
116. Zhang, L., et al., *Dielectric response and percolation behavior of Ni–P (VDF–TrFE) nanocomposites.* Journal of Advanced Dielectrics, 2017. **7**(03): p. 1750015.
117. Zhang, Y., et al., *Regulating dielectric and ferroelectric properties of poly (vinylidene fluoride-trifluoroethylene) with inner CH= CH Bonds.* Polymers, 2018. **10**(3): p. 339.
118. Chan, H., et al., *Dielectric permittivity of PCLT/PVDF-TRFE nanocomposites.* IEEE Transactions on Dielectrics and Electrical Insulation, 2000. **7**(2): p. 204-207.
119. Meng, N., et al., *Multiscale understanding of electric polarization in poly (vinylidene fluoride)-based ferroelectric polymers.* Journal of Materials Chemistry C, 2020. **8**(46): p. 16436-16442.
120. Kong, D.S., et al., *Dielectric and ferroelectric properties of P (VDF-TrFE) films with different polar solvents.* Journal of the Korean Physical Society, 2019. **74**: p. 78-81.
121. O'Hagan, D., *Understanding organofluorine chemistry. An introduction to the C–F bond.* Chemical Society Reviews, 2008. **37**(2): p. 308-319.
122. Jaffari, G.H., et al., *Structural and electrical response of poly (vinylidene fluoride-co-chlorotrifluoroethylene) copolymer free-standing films.* Polymer International, 2022. **71**(8): p. 1030-1038.
123. Al-Kuhaili, M., *Electrical conductivity enhancement of indium tin oxide (ITO) thin films reactively sputtered in a hydrogen plasma.* Journal of Materials Science: Materials in Electronics, 2020. **31**(4): p. 2729-2740.
124. Yang, J., et al., *Epitaxy enhancement of piezoelectric properties in P (VDF-TrFE) copolymer films and applications in sensing and energy harvesting.* Advanced Electronic Materials, 2020. **6**(10): p. 2000578.
125. Alemán-Vázquez, L.O., et al., *Use of hydrogen donors for partial upgrading of heavy petroleum.* Energy & Fuels, 2016. **30**(11): p. 9050-9060.
126. Xie, L., et al., *Properties and applications of flexible poly (vinylidene fluoride)-based piezoelectric materials.* Crystals, 2021. **11**(6): p. 644.
127. Park, B.-E., et al., *Ferroelectric-gate field effect transistor memories.* 2016.